Departamento de Investigación en Polímeros y Materiales

División de Ingeniería

Universidad de Sonora

First-principles study of electronic and optical properties of hybrid perovskites for use of solar cells

by

Edgar Paredes Sotelo

A Thesis Submitted in partial fullfillment of the requirements for the degree of Master in Materials Science.

Director: Dra. Rosa Elena Navarro Gautrín

Co-director Dr. José Luis Cabellos

Hermosillo, Sonora August 1, 2021

Institutional Statement

Dr. Teresa del Castillo Castro
Head of department

Hermosillo, Sonora, June 15, 2021.

Declaration

I declare this thesis titled: ***First-principles study of optical and electronic properties of hybrid perovskites for use of solar cells*** is a work of my own authority, which has been done to defend of my Master's work at the Universidad de Sonora. This work was made under the guidance of Dra. Rosa Elena Navarro Gautrín and Dr. José Luis Cabellos of the Universidad de Sonora.

Dedication

I dedicate this work to my parents **Edgar** *and* **Idalia**, *who gave me their full support and love during these strange times.*

Acknowledgments

Thanks to my **brothers Antonio and Idalia**, who put up with me in my bad days as well as in the good ones. And no matter the time, their advice never fell on deaf ears.

Thanks to all **my friends and colleagues** who were by my side during the two years. Above all, I thank **Luis Manuel** for his friendship and camaraderie.

I thank Dra. **Rosa Elena Navarro Gautrín** for being a guide in my development, and her consideration of this project. Her support during this process was without a doubt very helpful.

I thank Dr. **José Luis Cabellos** for being a guide in my development, for having the patience to support and advise me during the course of this project, and above all, for being a good friend.

Many thanks to my **thesis committee**; all their observations were of great help during the development of this work. I thank you for your time and support during these past years.

Thanks to Dra. **Carmen Heras** and L.C.C. **Daniel Mendoza Camacho** of the supercomputing department of Universidad de Sonora for allowing me to use the ACARUS supercomputer and all of its resources. Without their support, this work could not have been completed.

To **CONACyT** for the financial support it gave me with the grant number (CVU) 1008864 of the program *Becas Nacional (Tradicional) 2019-2*.

Abstract

Nowadays, hybrid perovskites are highly investigated materials for their optimal electronic and optical properties, making them semiconductors of the highest capacity for their use as solar energy harvesters in a photovoltaic device, so their study is very important. Finding their structure that defines these properties involves arduous effort and a lot of computational resources. In this thesis we studied the hybrid perovskites of lead methylammonium (MA) halides, $MAPbX_3$ where (X=I, Cl, Br), for simulating their structural, optical, and electronic properties. Each perovskite presents three structural phases which are (in order of symmetry) the orthorhombic, tetragonal and cubic phase. For each of the phases of its respective perovskite, its structural parameters, and optical properties such as the real and imaginary part of the dielectric function, refractive index, reflectivity, and its absorbance spectrum were calculated. For the electronic properties, the band structure, density of states (DOS), and projected density of states (PDOS) are presented. The results for each perovskite are then compared with their own phases and between the other perovskites and their experimental reported results to show their optimal structure to obtain the best properties for each of the perovskites for use as a light-absorbing layer of a solar cell. Our computed results indicate that the cubic Iodine hybrid perovskite is the best candidate for its experimental application in photovoltaic devices, exhibiting the largest absorption peak in the visible region of the solar spectrum. The optical and electronic properties were close to the experimental ones, and the perovskite structure's impact on its properties is demonstrated.

Works presented :

As part of this thesis, four works were presented in congresses.

- Poster presentation at the *Reunión Universitaria de Investigación en Materiales 2019*, Nov. 2019, Universidad de Sonora, Hermosillo, Sonora. A.0.1
- Participation in the *19th USPEX online workshop on crystal structure prediction with USPEX code* from November 11 to 13, 2020.
- Poster presentation in the online *Workshop on Excited Charge Dynamics in Semiconductors*, SMR3516 from September 28 to 30, 2020.
- Poster presentation at the *Reunión Universitaria de Investigación en Materiales, 2021*, Marzo 2021, Universidad de Sonora, Hermosillo, Sonora. A.0.2

Contents

1 Introduction **1**
- 1.1 Introduction . . . 1
- 1.2 Hypothesis . . . 4
- 1.3 Objectives . . . 4
- 1.4 Thesis outline . . . 5

2 Organometal halide perovskites as photovoltaic devices **7**
- 2.1 Perovskite materials . . . 7
- 2.2 Organometal halide perovskite solar cells . . . 9

3 Theoretical methods and background **11**
- 3.1 Density Functional Theory . . . 11
  - 3.1.1 DFT simulation software . . . 13
  - 3.1.2 Pseudopotentials . . . 14
  - 3.1.3 K-points . . . 15
- 3.2 Light-Matter Interaction Hamiltonian . . . 15
- 3.3 The Band-Gap . . . 19
- 3.4 Density of states . . . 21
- 3.5 Optical properties of perovkites . . . 21
  - 3.5.1 Linear Optical Response . . . 22
  - 3.5.2 Refractive index . . . 24
  - 3.5.3 Reflectivity . . . 24
  - 3.5.4 Absorption coefficient . . . 25
  - 3.5.5 Energy-loss spectrum . . . 25

4 Results and Discussion **27**
- 4.1 Structural properties . . . 28
  - 4.1.1 Cubic perovskites . . . 29
  - 4.1.2 Tetragonal perovskites . . . 31
  - 4.1.3 Orthorhombic perovskites . . . 31
- 4.2 Electronic properties . . . 34
- 4.3 Bandstructure: Cubic $MAPbX_3$ (X=I, Br, Cl) . . . 35
- 4.4 Bandstructure: Tetragonal $MAPbX_3$ (X=I, Br, Cl) . . . 37
- 4.5 Bandstructure: Orthorhombic MAPbX (X=I, Br, Cl) . . . 38
- 4.6 PDOS: Cubic MAPbX (X=I, Br, Cl) . . . 40
- 4.7 PDOS: Tetragonal MAPbX (X=I,Br,Cl) . . . 44
- 4.8 PDOS: Orthorhombic MAPbX (X=I, Br, Cl) . . . 44
- 4.9 Optical properties . . . 45
- 4.10 Optics: Cubic $MAPbI_3$,$MAPbBr_3$, and $MAPbCl_3$ . . . 47
- 4.11 Optical reflectivity & refractive index of cubic $MAPbI_3$ . . . 49

4.12 Optical absorption coefficent of cubic $MAPbI_3$ 52
4.13 Theoretical vs experimental results 56
4.13.1 Spectroscopic Ellipsometry 57

5 Conclusion and future prospects **59**
5.0.1 Electronic properties 59
5.0.2 Optical properties 59
5.1 Future work 62

A Appx. Congress **63**
A.0.1 Attendance certificate *RUIM* 2019 63
A.0.2 Attendance certificate *RUIM* 2021 64

B Appx. Linear response **65**
B.0.1 Perturbation approach 65
B.0.2 Scissors Hamiltonian 66
B.1 Velocity-gauge Formalism 67
B.1.1 Linear Response 68

Bibliography **73**

List of Figures

1.1 National Renewable Energy Laboratory solar cell comparison chart from 1976 to modern day, perovskite solar cell evolution can be seen in its entirely [National Renewable Energy Laboratory]. 2

1.2 We show the solar cell golden triangle connected with the cost, efficiency and lifetime parameters. 3

2.1 3D structure geoemtry of Perovskite. Panel (a) shows the cubic phase that is stable at high temperatures. Panel (b) shows the orthorhombic phase that is stable at low temperatures. The blue-colored sphere represents the methylammonium, the black colored sphere represent Pb atoms, whereas, the violet-colored sphere represent halogens atoms (I, Br, Cl) [Green 2014]. 7

2.2 Hybrid perovskite structural phases. 8

2.3 Normal and inverse structure of a planar and mesoporous solar cell. [Makableh 2019] 10

3.1 Upper panel; shows a comparison between a real-wavefunction depicted in blue-dashed and a pseudo-wavefunction depicted in red-solid line. Notice that large oscillations near the nucleus of the real-wavefunction. Lower panel; shows a comparison between the real-potential of an atom depicted in blue solid-lines and the pseudopotential depicted in red-dashed lines. 14

3.2 Brillouin zone scheme and k-point path used of (a) a simple cubic lattice R-Γ-X-M-Γ-X, (b) a orthorhombic lattice Γ-X-S-Y-Γ-Z-U-R-T-Z-Γ, and (c) a tetragonal lattice Z-Γ-M-A-R-X-Γ reported by Wahyu et al. [Setyawan 2010]. 16

3.3 Band gap representation of a conductor, semiconductor and insulator material. [Yusoff 2016] 20

3.4 Silicon band structure along the high symmetry path of the BZ and computed within the framework of DFT. The valence bands are depicted in blue-solid line, whereas, conduction are depicted in red-solid line. 20

3.5 Total Density of States (DOS) of bulk silicon computed employing *Quantum Espresso* code. The Fermi energy level has shifted to the zero-energy y-axis [Cargnoni 2000]. 22

4.1 3D structure of cubic $MAPbI_3$ (a), $MAPbCl_3$ (b), $MAPbBr_3$ (c). The violet, the green, and the copper color spheres represent the Bromide, Chloride, Iodide, respectively, while the big-sized gray spheres represent the lead atoms. The blue and light grey spheres represent the carbon and nitrogen atoms respectively, while the small white ones are the hydrogen bonded to each atom. 28

4.2 3D structure of tetragonal $MAPbI_3$ (a), $MAPbCl_3$ (b), $MAPbBr_3$ (c). The violet, the green, and the copper color spheres represent the Bromide, Chloride, Iodide, respectively, while the big-sized gray spheres represent the lead atoms. The blue and light grey spheres represent the carbon and nitrogen atoms respectively, while the small white ones are the hydrogen bonded to each atom. 30

4.3 3D structure of orthorhombic $MAPbI_3$ (a), $MAPbCl_3$ (b), $MAPbBr_3$ (c). The violet, the green, and the copper color spheres represent the Bromide, Chloride, Iodide, respectively, while the big-sized gray spheres represent the lead atoms. The blue and light grey spheres represent the carbon and nitrogen atoms respectively, while the small white ones are the hydrogen bonded to each atom. 32

4.4 The upper panel shows the band structure of the primitive cell for cubic $MAPbI_3$ along with the high-symmetry directions (HSD) on the Brillouin zone (BZ) R-Γ-X-M-Γ-X. The middle panel shows the computed band structure along the same HSD on BZ, employing the primitive cell for a cubic $MAPbBr_3$, and the lower panel shows the computed band structure along the same HSD on BZ, employing the primitive cell for the cubic $MAPbCl._3$. The blue-solid lines correspond to the valence bands and the red-solid lines correspond to the conduction bands. We show the band structure without an applied scissors correction. 35

4.5 The upper panel shows the band structure of the tetragonal primitive cell $MAPbI_3$ along with the HSD on the BZ Z-Γ-M-A-R-X-Γ. The middle panel shows the computed band structure along the same HSD on BZ, employing the primitive cell for a tetragonal $MAPbBr_3$, and the lower panel shows the computed band structure along the same HSD on BZ, employing the primitive cell for the tetragonal $MAPbCl_3$. The blue-solid lines correspond to the valence bands and the red-solid lines correspond to the conduction bands. We show the band structure without an applied scissors correction. 37

4.6 The upper panel shows the band structure of the orthorhombic primitive cell $MAPbI_3$ along with the HSD on the BZ Γ-X-S-Y-Γ-Z-U-R-T-Z-Γ. The middle panel shows the computed band structure along the same HSD on BZ, employing the primitive cell for a orthorhombic $MAPbBr_3$, and the lower panel shows the computed band structure along the same HSD on the BZ, employing the primitive cell for the orthorhombic $MAPbCl_3$. The blue-solid lines correspond to the valence bands and the red-solid lines correspond to the conduction bands. We show the band structure without an applied scissors correction. . . . 39

4.7 The upper panel shows the Kohn-Sham projected density of states (PDOS) for the cubic $MAPbI_3$ structure. The middle panel shows the PDOS for the cubic $MAPbBr_3$ structure, and the lower panel shows the PDOS for the cubic $MAPbCl_3$ structure. In all plots, the Fermi energy is shifted to zero. 40

4.8 The upper panel shows the Kohn-Sham projected density of states (PDOS) for the tetragonal $MAPbI_3$ structure. The middle panel shows the PDOS for the tetragonal $MAPbBr_3$ structure, and the lower panel shows the PDOS for the tetragonal $MAPbCl_3$ structure. In all plots, the Fermi energy is shifted to zero. 41

4.9 The upper panel shows the Kohn-Sham projected density of states (PDOS) for the $MAPbI_3$ structure. The middle panel shows the PDOS for the $MAPbBr_3$ structure, and the lower panel shows the PDOS for the $MAPbCl_3$ structure. All three perovskites are in their orthorhombic structural phase, and their Fermi energy is shifted to zero. 43

4.10 Frequency dependence of the $\varepsilon^{ab}(\omega)$ of the Cubic $MAPbI_3$. The upper panel shows the $\varepsilon_2^{ab}(\omega)$ in the ranging frequency from 0 to 10 eV, and the lower panel shows the $\varepsilon_1^{ab}(\omega)$ in the ranging frequency from 0 to 10 eV. The dielectric function is related to the imaginary part of electric susceptibility by $\varepsilon^{ab}(\omega) = 1 + 4\pi\chi_1^{ab}(-\omega;\omega)$. 47

4.11 Frequency dependence of the refractive index, $n(\omega)$, and reflectivity, $R(\omega)$, of the Cubic $MAPbI_3$. The upper panel (c) shows the refractive index in the ranging energy from 0 to 10 eV, and the lower panel (d) shows the reflectivity in the ranging energy from 0 to 10 eV. 48

4.12 Frequency dependence of the absorption coefficient ($\alpha(\omega)$) and energy loss spectrum, $L(\omega)$, of the Cubic $MAPbI_3$. The upper panel (c) show the absorption coeficient in in the ranging energy from 0 to 14 eV. The lower panel (d) show the loss energy spectrum in the ranging energy from 0 to 14 eV. 50

4.13 The upper panel shows the comparison of the $\mathfrak{Im}[\varepsilon^{ab}(\omega)]$ part for the three cubic perovskites of $MAPbI_3$, $MAPbBr_3$, and $MAPbCl_3$. The bottom panel shows the comparison of the $\mathfrak{Re}[\varepsilon^{ab}(\omega)]$ part for the the three mentioned cubic perovskites, in the energy range from 0 to 10 eV. Notice, the $MAPbI_3$ perovskite, shows the largest absorption peak located at 2.8 eV. Moreover, it is larger in 31% than Br perovskite. 55
4.14 The absorption coefficient of the tetragonal perovskite $MAPbI_3$, (a) computed in this thesis, and (b) an experimental one [Kanemitsu 2017]. The onset of $\alpha(\omega)$ is in agremment with the experimental one. The computed $\alpha(\omega)$ does not present the same behavior as the experimental one, on the spectrum $\alpha(\omega)$ there is a missing shoulder, that is probably due to excitonic effects. 58
4.15 Illustration of a typical ellipsometer configuration. Image taken from Ref. [Wang 2020]. 58

A.1 Attendance certificate of work presented in the: La Reunión Universitaria de Investigación en Materiales,*RUIM*, Nov. 2019, Universidad de Sonora, Hermosillo, Sonora. 63
A.2 Attendance certificate of work presented in the: La Reunión Universitaria de Investigación en Materiales,*RUIM*, March 2021, Universidad de Sonora, Hermosillo, Sonora. 64

List of Tables

2.1 $MAPbX_3$ structural phase transition temperatures [Oku 2015]. . . . 9

4.1 Calculated structural parameters for the cubic perovskite phases. Experimental parameters are shown for reference. For cubic structural phase: a=b=c. Cubic perovskite parameters. The table also shows a comparison of experimental parameters for each cubic cell. 29

4.2 Calculated lattice constants of tetragonal phase parameters with their experimental parameters reference for each perovskite. For the tetragonal structural parameters: a=b≠c. 31

4.3 Computed lattice constants of orthorhombic phase parameters with their experimental parameters reference for each perovskite. For the orthorhombic structural parameters: a≠b≠c. 32

4.4 We present the obtained values for the band gap, static reflectivity ($R(0)$), static refractive index ($n(0)$), static dielectric permittivity ($\varepsilon_1(0)$), and the maximum peak of the imaginary part of the dielectric constant (ε_2) with its respective amplitude, for $MAPbX_3$ perovskites in all their structural phases. 54

4.5 Calculated structural properties of a tetragonal $MAPbI_3$, cubic $MAPbBr_3$, and cubic $MAPbCl_3$ compared with their experimental (Exp.) counterparts. The calculated structural parameters showed an error of less than $\leq 2\%$ compared to the experimental results for all perovskites shown. 56

4.6 Calculated bandgaps of a tetragonal $MAPbI_3$, cubic $MAPbBr_3$, and cubic $MAPbCl_3$ compared with their experimental (Exp.) counterparts. The $MAPbI_3$ calculated bandgap was approximately underestimated by 16%, in comparison with its experimental result. 57

Chapter 1

Introduction

Contents

1.1 Introduction 1
1.2 Hypothesis 4
1.3 Objectives 4
1.4 Thesis outline 5

1.1 Introduction

It is very important to take into account green energies [Gielen 2019, Ellabban 2014], especially in recent years, where the pollution of seas, land, and air has caused havoc around the planet due to the excessive use of non-renewable fuels [Mohamed 2019, Stephenson 2018, Aleman-Nava 2014], technology has allowed advancements in research for new devices that reduce fossil fuels dependence, devices involved in renewable energy, such as solar energy. It is said that, per day, more than 1.65 x 10^{16} watts fall on the earth's surface by the sun [Wild 2013], an amount that if it could be harvested, it would be possible to end the current problems of this preamble.[Huang 2019, Zhang 2016, Xu 2015] Precisely for this reason it is necessary to find suitable forms for the correct transition between modern optoelectronic and devices of the past, especially during these years where fossils fuels lead with 80 % of the energy market [Jeon 2014b]. Therefore, in the case of devices such as solar cells, wherein these times amorphous silicon cells are the main ones in the world market with prices close to dollars per watt, efficiencies of 23 % and life span of around 20 years, it is necessary to find some other material with use as the active part of the solar cell. Of course, there are many, and in these times they are considered together with silicon, cells like CIGS [Benmir 2013], germanium [Osterthun 2021], or mixtures of silicon with another material [Fan 2010] that shows good results, but they have not been successful in taking the place of silicon as the material of excellence for photovoltaic devices. Among the materials that are currently being investigated, is perovskite. Perovskite is any material that carries a certain structural formula, every one of its members possesses the same structural formula. The first material discovered with such a structure as calcium titanium trioxide ($CaTiO_3$), which was discovered by mineralist Gustav Rose in the mountains of Russia, he then proceeded to name it perovskite, in honor of Count Lev Perovski, who first

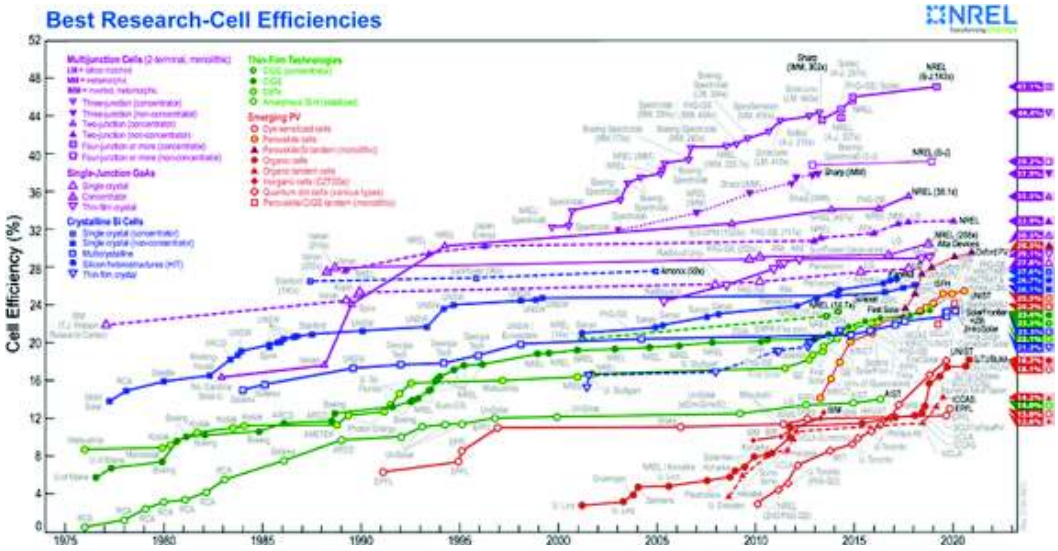

Figure 1.1: National Renewable Energy Laboratory solar cell comparison chart from 1976 to modern day, perovskite solar cell evolution can be seen in its entirely [National Renewable Energy Laboratory].

characterized the material [Yusoff 2016]. The perovskite family presents great advantages, depending on the components, it's possible to modify its properties, such as its absorption range, band gap, absorption coefficient, etc. In addition, many of these materials have a high emission in different ranges of the visible spectrum, which makes them very useful for the development of instruments for optoelectronic purposes. In this case, emerging solar cells, for example, those based on hybrid perovskites, or perovskite solar cell (PSC), are made up of an organic and an inorganic part, that have shown good results, [Liu 2013a] the most studied PSC material is $MAPbI_3$. The energy conversion efficiency of solar cells, which can be with a porous structure or a flat structure, has reached over 26 % as viewed in Figure 1.1 in the year 2020, and it is estimated that solar modules can have low prices around 0.1 dollars per watt [Cai 2017]. For this reason, perovskite solar cells can become the photovoltaic technology of the new generation, due to their excellent properties and low production cost. Whenever we talk about solar cells and their utility, the golden triangle of solar cells must be taken into account, see Figure 1.2, this indicates that a reliable solar cell must have a good balance between the cost of manufacturing, energy production, and its stability which is defined as the average lifetime before it begins to reduce its capacity and its performance [Meng 2018]. Hybrid perovskite solar cells have shown themselves as great contenders against other types of cells, because of their low cost and high performance, their only weakness lies in their short useful life [Niu 2015] comparing it for example with silicon solar cells that have an average lifetime of 20 years, this being a topic of high interest that is under investigation [Lee 2014].

Figure 1.2: We show the solar cell golden triangle connected with the cost, efficiency and lifetime parameters.

Experimental research has made great strides on these issues, but there is another approach we can take in the study of these materials. We can use what is referred to as materials simulation, where simulation is defined as the production of a computational model of something, where its study is the main purpose [Gomes 2019]. Some time ago, the chemistry was thought to be a discipline that developed experimentally, and it was for many years. This until the 1970s when computer software began to be used in order to explain approaching chemistry in a way that experimental chemistry could never achieve. At first pharmaceutical companies promoted computational chemistry in the search for new drugs with a positive biological effect. Nowadays we can use these methods to obtain the optical and electronic properties of periodic materials in a completely controlled environment, which can pave the way for experimental development [van Mourik 2014].

Electronic structure packages are in stock that allows us to simulate compound molecules for study. These packages are in free formats like *ABINIT* [Romero 2020, Gonze 2005, Gonze 2002] and other under license ones like *VASP* [Kresse 1993a, Kresse 1996], these packages present a great opportunity to study periodic systems. *QE* software [Giannozzi 2009, Giannozzi 2017, Giannozzi 2020] is a free program for the scientific community, used for the calculation of optical, structural, vibrational properties, etc. of the materials. Its use is of great importance since it allows us to use the DFT that is a large part of this work. On the other hand, the Vienna Ab initio simulation package or also known as *VASP* by its initials, is a computer program for modeling atomic structures of materials and its main utility is the calculation of their electronic structure and the dynamic molecular mechanics of materials [Kresse 1993b].

Density Functional Theory (DFT) is a highly used quantum method to calculate the electronic structure of materials. [Becke 2014b] DFT is based on the Thomas-Fermi approach, developed by Thomas and Fermi in 1927 [Thomas 1927a,

Teller 1962]. The method allows calculations such as the electronic and molecular density of materials. It was introduced in 1964 by Kohn and Hohenberg, focusing on the system density [Hohenberg 1964], this is where it differs from other methods such as the Hartree method, which is based on the wave function [Yehuda B. Band 2013]. There are hundreds of articles that use it for the above, this due to the quality of results that we can see in these publications. For perovskite type semiconductors it has been applied for many of its family members such as $MAPbX_3$, in its 2D and 3D structures, the latter has great characteristics for use as optoelectronic devices. Using DFT allows us to obtain almost every property of materials such as their structural, electronic, optoelectronic, magnetic, and thermodynamic properties.

So much is the effect of perovskites in optoelectronics that thousands of investigations have been developed by theoretical computational means, with the objective to lead the way of experimental research progress for these materials and their application in industry. It has also been proven that the use of computational methods such as DFT, produces results of a good level in terms of the simulation of their atomic structures, although there is some uncertainty in terms of the electronic ones, so more advanced methods are used to bring the results as close as possible to those found experimentally. [Diau 2017]

In the present work, the structural, optical, and electronic properties for the cubic, tetragonal and orthorhombic phases of the $MAPbX_3$ perovskites were determined, using pseudopotentials approximation and plane-wave basis-DFT implemented in the *Quantum ESPRESSO* [Giannozzi 2017, Giannozzi 2020] simulation package which was chosen because of its number of usable pseudopotentials, high accessibility, and open-source nature [Giannozzi 2009].

1.2 Hypothesis

The use of the DFT as a theoretical-computational basis for conducting in silico experiments allow us to find which hybrid perovskite material MAPbX3 (X= I, Br, Cl) has the best optical response when it is exposed to solar light.

1.3 Objectives

General objective

- To compute the optical and electronic properties of the following perovskites: $CH_3NH_3PbI_3$, $CH_3NH_3PbBr_3$ and $CH_3NH_3PbCl_3$ employing density functional theory as it is implemented in the open-source computer software *Quantum ESPRESSO* [Giannozzi 2009, Giannozzi 2017, Giannozzi 2020].

Specific objectives

- Installation of *Quantum ESPRESSO* in High Performance Computing Area of Sonora University.

- Comprehend *Quantum ESPRESSO* basics and become familiar with DFT and its basic theory.

- Review and deduction of the radiation-matter interaction Hamiltonian whithin $\mathbf{A} \cdot \hat{\mathbf{p}}$ gauge, [Cabellos 2009a] where $\hat{\mathbf{p}}$ is the quantum opertor of moment and $\mathbf{A}$ is the vector potential [Cabellos 2009b].

- Review of electrical susceptibility tensor of first order (Linear optical response) following the Ref. [Cabellos 2009a, Cabellos 2011]

- Computing the ground-state geometries for all perovskites materials and their respective structural phase.

- Computing and obtain the electronic (Band structure, Density of states) and optical properties (absorption, refractive index, reflectivity, etc.), for every perovskite material. To achieve this, the imaginary part, $\mathfrak{Im}[\chi(-\omega;\omega)]$, and the real part, $\mathfrak{Re}[\chi(-\omega;\omega)]$ of the dielectric function, are calculated within the framework of the linear response theory and following the methodology of this Ref. [Cabellos 2009a].

1.4 Thesis outline

- This thesis work is a theoretical study on the structural, electronic, and optical properties of methyl ammonium lead iodide, chloride, and bromide, $CH_3NH_3PbX_3$ (X= I, Cl, Br) perovskites. The simulated results are made possible using PBE (Perdew-Burke-Ernzerhof) exchange-correlation functional using a plane-wave basis set with density functional theory (DFT).

- Chapter 2 presents a brief introduction and useful information on hybrid perovskite materials, their history and development as photovoltaic devices of the current era, with a focus on the main perspective for their use as an absorption layer of a solar cell, as shown reported in recent years.

- Chapter 3 recalls the theoretical aspects of this work, mainly the functional theory of density, linear optical response, pseudopotentials, a complete deduction of the Light-Matter interaction Hamiltonian is presented, also, the *Quantum ESPRESSO* electronic structure package is discussed.

- Chapter 4 arguments on the results calculated for each of the investigated perovskites, their structural parameters of their cubic, tetragonal, and orthorhombic phase with their respective electronic properties (band gap, density of states, etc.), and optical properties (dielectric properties, absorption, reflective index, etc.) for each structural phase. These results are presented with a comparison between each perovskite.

- Chapter 5 concludes this thesis, summarizing the results obtained and giving an overview of possible future studies, in addition, all the references consulted in this research work are presented.

Chapter 2

Organometal halide perovskites as photovoltaic devices

Contents

2.1 Perovskite materials 7
2.2 Organometal halide perovskite solar cells 9

2.1 Perovskite materials

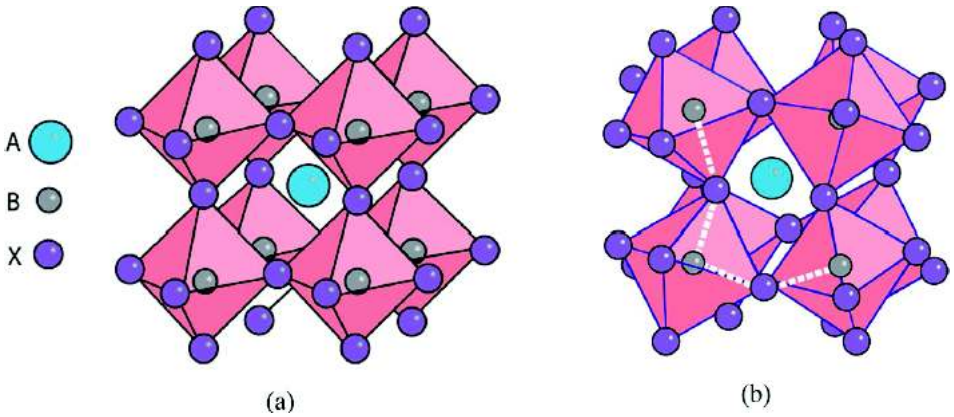

Figure 2.1: 3D structure geoemtry of Perovskite. Panel (a) shows the cubic phase that is stable at high temperatures. Panel (b) shows the orthorhombic phase that is stable at low temperatures. The blue-colored sphere represents the methylammonium, the black colored sphere represent Pb atoms, whereas, the violet-colored sphere represent halogens atoms (I, Br, Cl) [Green 2014].

The perovskite family exhibits many different types of behaviors. This one is very numerous, and at the moment it continues to grow. In a natural way, the first perovskite found and detailed is $CaTiO_3$ [Lemanov 1999, Liu 2015], this, like all others, has an ABX_3 conformation as a structure, where A is a monovalent cation, B a metallic cation, and X, an anion. Its structure has become quite famous nowadays thanks to the wide arranges of applications this family of materials can have. They have been widely used for their excellent conductive, optical, and magnetic

properties. Since their family is very extensive, it is possible to determine some perovskite with properties that make them useful in some fields. In Figure 2.1 we have the ABX_3 perovskite family 3D structure. Here the B cation coordinates with six X anions forming an octahedral geometry surrounding the B cation, four of these structures surround the A cation, where the latter coordinates with twelve X anions forming a cuboctahedral geometry [Liu 2013b, Petrovic 2015].

On the other hand, the hybrid perovskites, or organometallic, have a structure similar to the normal ones. The main difference is that the cation A of the structure ABX_3, is an organic cation, representative ions are methylammonium (CH_3NH_3 + or MA +) and formamidinium ($H_2N\text{-}CH{=}NH_2$), as for B metallic cations with a smaller radius are used (Pb, Sn, Ge), and for X, typically a halogen ion is found (Cl, I, Br) [Diana Marcela Montoya Montoya 2016, Indari 2017, Eperon 2014].

There are three major perovskite crystal structures phases, cubic, tetragonal, and orthorhombic. Perovskites materials tend to present these as shown in Figure 2.2, a cubic Pm-3m phase, an orthorhombic Pnma phase, and a tetragonal I4/mcm phase. The Table B.5, show the paThe orthorhombic phase occurs when the perovskite material is at very low temperatures. This phase tends to maintain its stability up to 165 K, temperatures above it begin to transform the structural symmetry from orthorhombic to a tetragonal symmetry with greater stability. The present orthorhombic phase belongs to the Pnma group. In the case of the tetragonal phase, it remains stable between temperatures of 165-330 K, the phase belongs to the space group I4/mcm, over 330 K, the tetragonal phase undergoes a transformation to a cubic phase with a space group Pm-3m of greater symmetry [Whitfield 2016, Oku 2015]. The tetragonal phase tends to be the most used and studied due to its high stability at room temperature. For ease of comparison, Table B.5, shows the parameters of the three major perovskite crystal structures. Lead methylammonium halide perovskites have shown an ability to change their

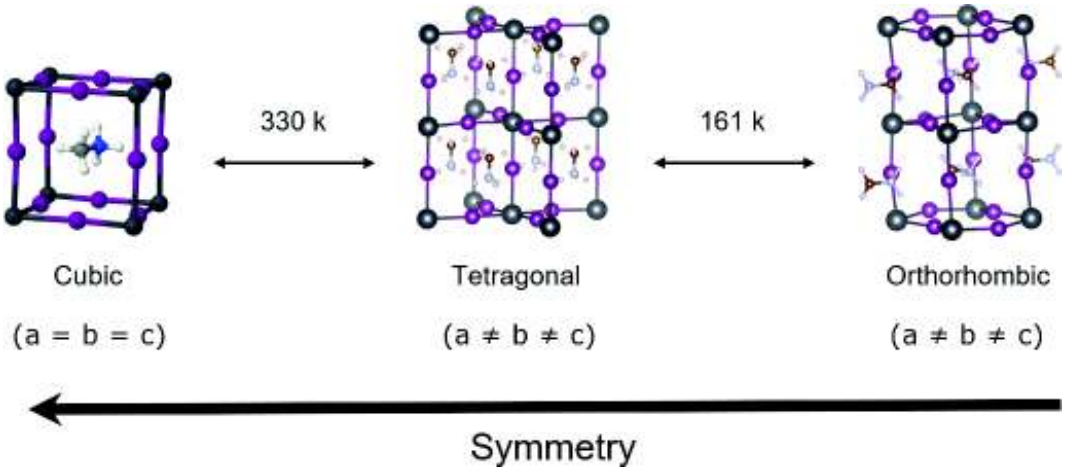

Figure 2.2: Hybrid perovskite structural phases.

electronic properties by modifying the halogens in their structure. The latter is possible since the area near the band gap of its electronic structure is dominated by lead and halogen orbitals. Therefore, it is possible to modify their band gap by substituting the B cations of their structure, modifying their performance completely. As it is possible to modify these materials in this way, it is also understood that these perovskites manifest a wide range of electronic behaviors, such as semiconductor, superconducting, piezoelectric, and thermoelectric, of course depending on the composition and specific structure of the material transforming them to an acceptable state for their intended use.

Perovskite	**$MAPbI_3$**	**$MAPbBr_3$**	**$MAPbCl_3$**
Structural phase	Cubic	Cubic	Cubic
Transition Temperature (K)	330	236	177
Structural phase	Tetragonal	Tetragonal	Tetragonal
Transition Temperature (K)	161	$149 \approx 154$	172
Structural phase	Orthorhombic	Orthorhombic	Orthorhombic

Table 2.1: $MAPbX_3$ structural phase transition temperatures [Oku 2015].

2.2 Organometal halide perovskite solar cells

Organometal halide solar cells have emerged as one of the cells with the highest efficiency, in the short time that they have been investigated, and have presented a greater advancement compared to other materials. These types of cells have presented a great advantage, their flexibility, low cost, simplicity of manufacture, and their abundance, have made them very sought after in the scientific area. [Wu 2019] Organometal halide perovskite solar cells were introduced first by Miyasaka et al. in the year 2009 [Kojima 2009], the first attempt used $MAPbX_3$ (X = I, Br) as visible-light sensitizers in dye-sensitized liquid junction type solar cells. This led to an energy conversion efficiency (PCE) reported of 3%. by 2012 they had reached a PCE up to 10.9% [Snaith 2012]. As of 2020, organometal halide solar cells have proved to be capable solar cells showing PCE's of nearly 26% as seen on the efficiencies chart of the national renewable energy lab. [Mamedov 2011]

Solar cells with the perovskite material are commonly found with different layers where this is the centerpiece or solar absorbance layer. The general structure of a perovskite solar cell contains a transparent conductive oxide (TCO) material superimposed on glass, a hole-transporting material (HTM), a layer of the perovskite material, an electron-transporting material (ETM), and a metallic contact.

Perovskite solar cells can be made either planar or mesoporous in structure, both can be created directly or inverse, depending on how the layers of the cell are arranged. In planar solar cells, the cell layers are manufactured one on top of the other separately, while in the mesoscopic structure, some layers, such as the

electron-transport layer or hole-transporting layer are manufactured as a mesoporous structure filled with perovskite material. which improves the optical and electrical properties of perovskite. [Makableh 2019] In figure 2.3 we can see the direct and inverse form of the planar perovskite solar cell. Aside from the pure perovskite layer and mesoporous perovskite, both planar and mesoporous share the same composition regarding their structure. Normally the layer of void carrying material is

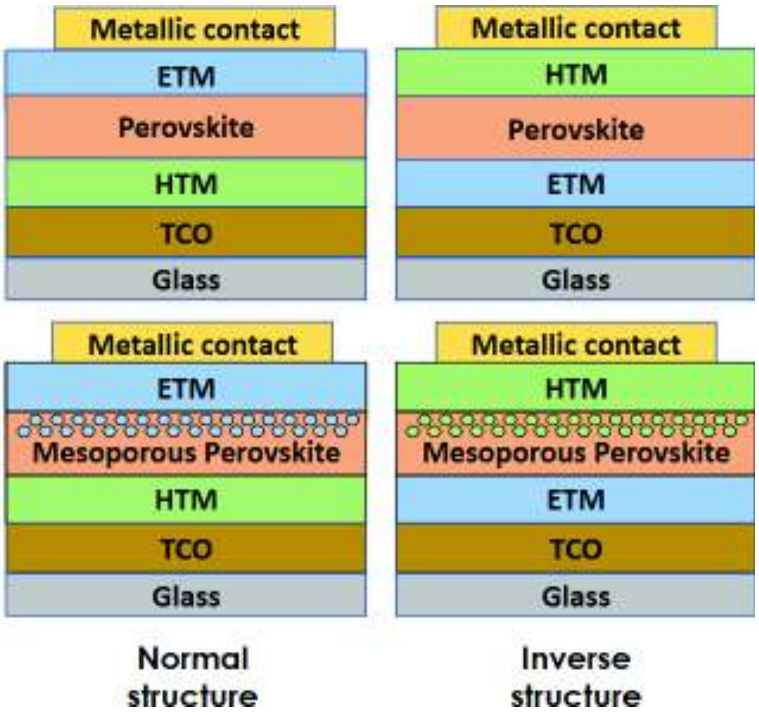

Figure 2.3: Normal and inverse structure of a planar and mesoporous solar cell. [Makableh 2019]

added by spin coating to a TCO material, where chlorine-doped tin oxide (FTO) and indium-doped tin oxide (ITO) are typically used. This serves to extract holes from the perovskite material and transfer it to the electrodes. Electron transport materials usually a metal oxide like TiO_2 [Park 2015, Wu 2014], ZnO [Wu 2014] and SnO2 [Zuo 2016] can be used for the solar cell. On the other hand, pit carrier materials such as NiOx, CuOx, CrOx, and poly (3,4-ethylenedioxythiophene) polystyrene sulfonate (PEDOT PSS) [Wei 2017], spiro-OMeTAD [Wu 2014] are used. In the case of the metallic contacts, the most commonly used are silver and gold [Wu 2018c].

To date, no form of commerce-related application of these materials has been demonstrated in the photovoltaic area, so there is still a long way to go before these materials are practical enough to be used for commercial applications around the world. However, perovskite solar cells have shown a very promising advance, and it is still being seen these days; These have shown properties similar to high efficiency cells such as silicon or CdTe, so it is expected that very soon we will see these materials being applied all over the world.

Chapter 3

Theoretical methods and background

Contents

3.1 Density Functional Theory 11
3.1.1 DFT simulation software 13
3.1.2 Pseudopotentials 14
3.1.3 K-points 15
3.2 Light-Matter Interaction Hamiltonian 15
3.3 The Band-Gap 19
3.4 Density of states 21
3.5 Optical properties of perovkites 21
3.5.1 Linear Optical Response 22
3.5.2 Refractive index 24
3.5.3 Reflectivity 24
3.5.4 Absorption coefficient 25
3.5.5 Energy-loss spectrum 25

3.1 Density Functional Theory

DFT is a quantum method utilized [Janesko 2021] to research the quantum mechanical structure of materials via a density approach, it is one of the most popular methods used for the simulation of periodical systems and surface energy on molecular systems. It's a powerful tool for the calculations of the quantum state of solids, atoms, and molecular dynamics. DFT has been used by many researchers over the years and some of the highest cited physicians are DFT theorists, most known are the names of Richard Smalley, Alex Becke [Becke 2014a], and most notably John Perdew who has one of the worlds most cited articles [Perdew 1996] which of course concerns DFT theory, as seen on google scholar [4/10/2021]. Some other methods have proven quite capable *ab-initio* simulation research, but while they suffer from plenty of variables, like the calculation of many-electron wave function of a many-atom system, requiring a vast arrange of computational resources where the complexity of the problem at hand may render the most advanced computational

labs useless. DFT presents a solution, as it only takes into account the electron density of the system, reducing the number of variables to only three, the x, y, and z, as in the position coordinates, which is a good contrast compared to, for example, the time-dependent Schrödinger equation, where it is necessary to obtain the wave functions associated with the state in which a system is found. The latter is extremely complex being that there is no exact analytical solution for many-electron systems [Schrödinger 1926, Viklund 2016]

The beginning of DFT is found in the creation of Thomas Fermi's theory, a method designed to find the electronic structure of atoms using the ground state density of an electron $\rho(r)$ [Fermi 1928, Lieb 1977, Thomas 1927b]. Although the theory showed many interesting and useful points, his work failed to stand out due to the large number of variables that remained unsolved. Even so, in the following years, there began to be outstanding advances on the subject with the Hohenberg and Kohn theorems [Hohenberg 1964] in the year 1964, these being followed by the work of Kohn and Sham [Kohn 1965] in 1965, where they made known that in fact, the electronic density could be obtained by using the one-electron theory, which completely and exactly determining all the ground state properties of an N-electron system, letting us sidestep the computational difficulty required to process a many-nucleus, many-electron wave function system, this by focusing on the electron density instead of the many-body wave function. This being said, DFT's main principle tells us that the total energy of a system is a unique function of the electron energy, it is a theory that adequately describes the properties of the ground state of a system, Hohenberg and Kohn theorems show us that the electron density is the most important variable in the description of a system in its ground state. Hohenberg and Kohn proposed their first theorem, which states that ground state energy depends solely on electron density, which means that it is a functional of electron density. Their second theorem proved that by minimizing the energy of the system according to the electron density, the ground state energy can be obtained for a system [Zhou 2007, Von Barth 2004].

While DFT works as a first principles method it has a fundamental problem in its structure, it underestimates the bandgap [YAKOVKIN 2007, Cabellos 2009a, Hybertsen 1986, Castillo-Quevedo 2020], this is reflected in the results, showing values with an error percentage in comparison with experimental data. DFT being a ground state theory, meaning that providing an accurate description of the electronic structure of a system can be difficult. For a correct DFT calculation, the quantum-mechanical exchange and correlation of the particles or exchange-correlation (XC) potential must be set [Burke 2012]. The exchange energy refers to the corresponding energy exchange between two or more electrons in their positions with the same spin orientation, and the correlation energy is the difference of the total energy of the system and the sum of the kinetic, potential, and exchange energies. Up to now, extensive research has been done to find some type of approximation that gives the most chemically accurate results to obtain the XC potential. Local density approximation (LDA) and the Generalized gradient approximation (GGA) are the more popular and widely use approximations [Rathod 2017].

Local density approximation (LDA) was the first approximation used to obtain the energy of XC [Kohn 1965]. The energy density XC in LDA at a position r, depends only on the density of particles at that point, $n(r)$. This density dependence must be identical to that of a homogeneous electron gas (HEG) of the same density $nHEG = n(r)$ and because it has been precisely calculated [Klimeš 2011]. The exchange correlation energy is totally local in the LDA approximation [Janesko 2021] and it ignores the effect of nearby inhomogeneity in electron density [Seminario 1995, Argaman 2000]. The LDA for the exchange and correlation energy can be written as

$$E_{XC}^{LDA}[n] = \sum n(r)\varepsilon_{XC}(n)dr \tag{3.1}$$

where n is the electronic density, ε_{XC} the exchange correlation energy per particle corresponding to the charge density n, which is a linear combination of exchange and correlation energies. [Ramanujam 2015a]

Most extensions of LDA include a dependency on the Generalized gradient approximation (GGA) [Perdew 1986] that includes functionals such as Perdew, Becke and Ernzerhof (PBE). GGA systematically improves the atomization or cohesion energies of a wide range of molecules and solids and correct the severe overbinding of LDA hydrogen-bonded solids. Right now, PBE-GGA is the most popular approach, from which high-quality results are obtained [Perdew 1996]. The PBE functional has been successfully employed in many previous calculations. In 2014 Feng et al. [Feng 2014] studied elastic properties under DFT employing PBE functional are with good agreement with experimental data. Later, Liu et al. [Liu 2018] computed electronic and thermodynamic properties in a new Cs-doped efficient and stable perovskite solar cell employing the PBE functional with good results. Many other works employing the PBE functional in hybrid perovskites for the computation of the electronic and optical properties have been previously published [Shi 2018, Hernández-Haro 2019, Mosconi 2015b, Shirayama 2016, Wu 2018b, Mosconi 2015a, Geng 2014, Giorgi 2015, Targhi 2018, Kim 2014].

3.1.1 DFT simulation software

The popularity of the DFT cannot be denied, thousands of articles are published a year using it, and that without number the articles that seek to improve this theory. There is so much on this side that they have designed a multitude of software to take advantage of the value that the DFT offers and put it at a distance from anyone wanting to learn. Of course, using it is not something simple, and it requires a lot of time to use correctly, a life would not be enough to try everything it can offer us. Carrying out these studies requires a high computational base. The software must be capable of executing this type of calculation and yield acceptable results for it to be useful.

In this work, the *Quantum Espresso* software was chosen, which offers us a great diversity of studies, it is comparable with much other software, with QE it is possible to obtain ground-state calculations, spectroscopic properties, structural optimization, molecular dynamics, etc. [Giannozzi 2009] However, QE is free to use

software that makes it available to all researchers. Apart from the previous one, among the programs that are available to perform DFT calculations, we have VASP [Kresse 1993b], CASTEP [Clark 2005], ORCA [Neese 2012], CP2K [Kühne 2020], GAMESS [Barca 2020], SIESTA [Soler 2002], etc.

3.1.2 Pseudopotentials

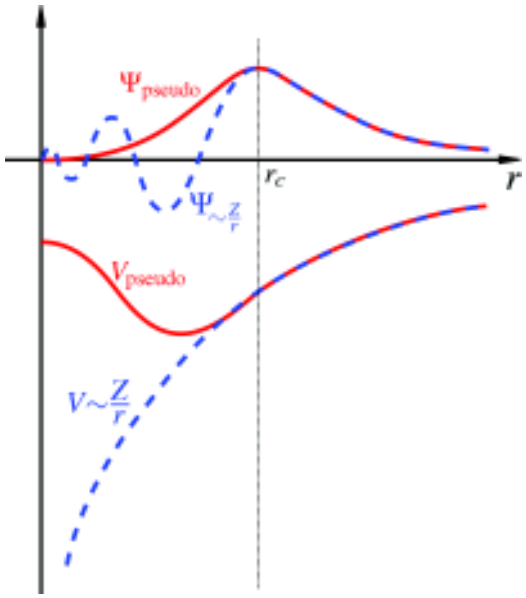

Figure 3.1: Upper panel; shows a comparison between a real-wavefunction depicted in blue-dashed and a pseudo-wavefunction depicted in red-solid line. Notice that large oscillations near the nucleus of the real-wavefunction. Lower panel; shows a comparison between the real-potential of an atom depicted in blue solid-lines and the pseudopotential depicted in red-dashed lines.

Pseudopotentials are approximations of the complex structure of the core electrons of an atom nucleus for calculating energies of outershell electrons. [Heine 1970] They replace the atomic potential of all electrons with an effective potential such that the nucleus core states no longer exist, and the valence states are represented by a pseudowavefunction that can be described with fewer Fourier modes, thus reducing computational cost with the use of a plane wave basis. This has made it possible to accurately calculate the properties of solids without the need for any adjustable parameters [Ramanujam 2015b, Denteneer 1987].

With pseudopotentials it is possible to simulate material structures and estimate their behavior under desired conditions. In DFT the use of pseudopotentials can dramatically reduce the number of planes waves to expand a wave function, improving the calculation, making them a necessary element for all plane-wave methods.

Many methods have been proposed to calculate pseudopotentials over the years, such as Norm-conserving pseudopotentials (NCPP) which have quickly shown that

the potentials for transition metals and for first row elements which turn out to be extremely hard [Bachelet 1982], Ultrasoft pseudopotentials (USP) which were introduced by Vanderbilt [Vanderbilt 1990] in order to allow calculations to be performed with the lowest possible cutoff energy for the plane-wave basis set, applying to systems with first row elements (s- and p-) and for systems with d- or felectrons [Vanderbilt 1990], etc. By "hard" and "soft", we mean the degree of hardness. A pseudopotential is considered soft when it requires a small number of Fourier components for its accurate representation and vice versa. That is why Ultrasoft pseudopotentials are generally characterized by a longer cut-off radius than NCPP, the larger the cut-off radius, the faster they converge, but they become less accurate.

In Figure 3.1, We depicted the real potential of an atom in a blue dashed line, notice it asymptotically goes to minus infinity. In the red solid line, a pseudopotential is depicted. The idea is to cut the large tail that the real potential possesses, which makes it difficult to find the solution of the Schrödinger equation. At the top of the figure, is depicted the wavefunction for the real potential in blue dashed line, notice the oscillatory behavior that numerically is very hard to represent, but with the red line, the pseudopotentials wavefunction depicted is a smooth function that can be handled very easily.

In the following sections, we will discuss other approximations that the theory of the density functional employ, in the calculations of the optical properties investigated for our materials and the light-matter interaction.

3.1.3 K-points

The first Brillouin zone in reciprocal space (a mathematical constructed space) is defined as a primitive cell, where it is divided into small equal parts called Brillouin zones. [Beiser 1987] Its behavior is like that of a Bravais lattice, where it is instead divided into Wigner-Seitz cells. The limits found in the Brillouin zones are given by plans related to points on the reciprocal lattice. These so-called points are high symmetry locations identified with Greek letters.

So, these high symmetry locations or K-points, are sampling points in the first Brillouin zone of the material, this is the specific region of reciprocal-space which is closest to the origin which is referred to as Gamma point or (0, 0, 0). By studying the first Brillouin zone we can completely characterize a material behavior. This field has been extensively studied and there are many works that present information on the types of systems belonging to perovskites, the orthorhombic, tetragonal, and cubic system have been previously reported [G. Burns 1990, Kovalev 1965, Tombe 2017], in this work we use different K-point paths for each type of structural phase.

3.2 Light-Matter Interaction Hamiltonian

Every optical property deals with the interactions of atoms and molecules with electromagnetic fields, because of this, it's important to understand how light and matter can interact with one another. For the deduction of this section, several

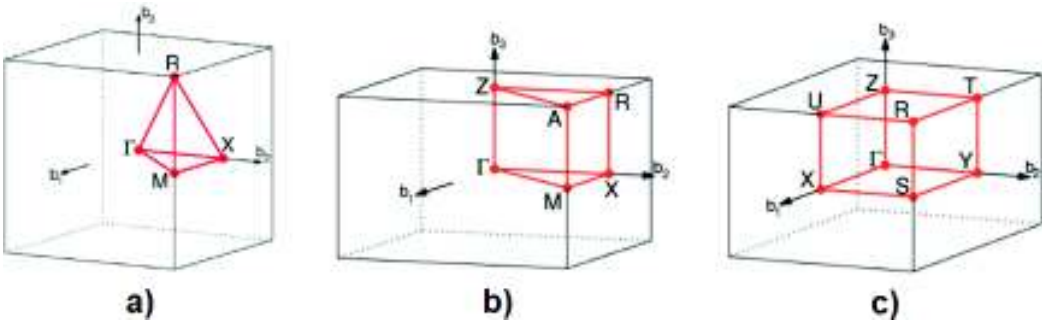

Figure 3.2: Brillouin zone scheme and k-point path used of (a) a simple cubic lattice R-Γ-X-M-Γ-X, (b) a orthorhombic lattice Γ-X-S-Y-Γ-Z-U-R-T-Z-Γ, and (c) a tetragonal lattice Z-Γ-M-A-R-X-Γ reported by Wahyu et al. [Setyawan 2010].

books and articles [Aversa 1995] were consulted, among them, the book Time Dependent Quantum Mechanics and Spectroscopy was consulted [Tokmakoff 2019], Electronic Structure: Basic Theory and Practical Methods [Martin 2004], Nonlinear Optics [Boyd 2013] and many others. [Kittel 2004, Ashcroft 1976, Walls 2012, Singh 2012, Fox 2006, He 1999].

To obtain the Hamiltonian for a charged particle in an electromagnetic field, we start with the Lorentz force

$$F = q\,(E + vxB) \tag{3.2}$$

In the Equation 3.2 F is the Lorentz force, v is the velocity of the particle. If we put the equation in terms of the Cartesian components of the electric and magnetic field, we have

$$F_x = q\,(E_x + v_y B_z - v_z B_y) \tag{3.3}$$

Then we express the Lorentz force in terms of the total potential energy V and we obtain

$$F_x = -\frac{dV}{dx} + \frac{d}{dt}\left(\frac{dV}{dv_x}\right) \tag{3.4}$$

The total potential energy can be expressed as shown in the next equation

$$V = q\phi - q\bar{v}\cdot\bar{A} \tag{3.5}$$

We then write the Lagrangian in terms of the kinetic energy and the total potential energy where $L = T - U$, so we can show that

$$L = \frac{1}{2}m\bar{v}^2 + q\bar{v}\cdot\bar{A} - q\phi \tag{3.6}$$

The classic Hamiltonian that describes charged particles in a field is related to the Lagrangian as show below

$$H = \bar{p} \cdot \bar{v} - L = \bar{p} \cdot \bar{v} - \frac{1}{2} m \bar{v}^2 \cdot \bar{A} - q\phi \tag{3.7}$$

Then we obtain

$$\bar{p} = \frac{dL}{d\bar{v}} = m\bar{v} + q\bar{A} \tag{3.8}$$

So, we can describe $\bar{v}$ as

$$\bar{v} = \frac{1}{m}\left(\bar{p} - q\bar{A}\right) \tag{3.9}$$

If we substitute equation 3.9 into equation 3.7 we get that the Hamiltonian can be written as

$$H = \frac{1}{m}\bar{p} \cdot \left(\bar{p} - q\bar{A}\right) - \frac{1}{2m}\left(\bar{p} - q\bar{A}\right)^2 - \frac{q}{m}\bar{p} \cdot \left(\bar{p} - q\bar{A}\right) \cdot A + q\phi \tag{3.10}$$

$$H = \frac{1}{2m}\left[\bar{p} - q\bar{A}_{(\bar{r},t)}\right]^2 + q\phi_{(\bar{r},t)} \tag{3.11}$$

Equation 3.11 is the classic Hamiltonian for a particle inside an electromagnetic field [Berestetskii 2012] Obtaining equation which lets us obtain the polarization of a singular system we can express our Hamiltonian as

$$\hat{H} = \hat{H}_0 + \hat{H}_i \tag{3.12}$$

Where $\hat{H}$ is the Hamiltonian operator, $\hat{H}_0$ is the base Hamiltonian, and $\hat{H}_i$ is the interaction Hamiltonian [Nastos 2005]. We then chose a gauge for the representation of the wave, in this case, the Coulomb gauge, where $\nabla.A = 0$ and in the absence of charges the scalar potential equals zero, $\phi = 0$. Taking this into account, in the Coulomb gauge, the last term of equation 3.11 is dropped and we get

$$\hat{H} = \frac{P^2}{2m} + V_r \tag{3.13}$$

Where P is the momentum operator, m the mass of an electron, and v_r is the potential energy of the system. This is the Hamiltonian for a free particle. The momentum operator can be replaced by the sum of the same operator and the force of an electron traveling through an electric field.

$$P \to P - \frac{e}{c}A \tag{3.14}$$

We substitute equation 3.14 in equation 3.13 and we get

$$\hat{H} = \frac{1}{2m}\left(P - \frac{e}{c}A\right)^2 + V_r \tag{3.15}$$

with m the mass of the electron, P its canonical momentum, and V_r is the local periodic crystal potential, we neglect spin-orbit terms. Here, we will derive the Hamiltonian for the light-matter interaction, the Electric Dipole Hamiltonian which is obtained by starting with the force experienced by a charged particle in an electromagnetic field, developing a classical Hamiltonian for this system. The momentum operator can be written as:

$$P = -i\hbar\nabla \tag{3.16}$$

Equation 3.15 then becomes

$$\hat{H} = \frac{1}{2m}\left(-i\hbar\nabla - \frac{e}{c}A\right)^2 + V_r \tag{3.17}$$

$$\hat{H} = \frac{1}{2m}\left(-i\hbar\nabla - \frac{e}{c}A\right)\left(-i\hbar\nabla - \frac{e}{c}A\right) + V_r \tag{3.18}$$

$$\hat{H} = \frac{1}{2m}\left(-\hbar^2\nabla^2 + \frac{i\hbar e}{c}\nabla\cdot A + \frac{i\hbar e}{c}A\cdot\nabla + \frac{e^2}{c^2}A\cdot A\right) + V_r \tag{3.19}$$

$$\hat{H} = \frac{-\hbar^2\nabla^2}{2m} + \frac{i\hbar e}{2mc}\nabla\cdot A + \frac{i\hbar e}{2mc}A\cdot\nabla + \frac{e^2}{2mc^2}A\cdot A + V_r \tag{3.20}$$

After some derivation we get that

$$\hat{H} = \frac{-\hbar^2\nabla^2}{2m} + \frac{i\hbar e}{2mc}\left(\nabla\cdot A + A\cdot\nabla\right) + \frac{e^2}{2mc^2}A\cdot A + V_r \tag{3.21}$$

Since we are working with the chain rule, the first term of $(\nabla \cdot A + A \cdot \nabla)$ is zero because $\nabla.A = 0$.

$$\hat{H} = \frac{-\hbar^2\nabla^2}{2m} + \frac{i\hbar e}{2mc}(2A \cdot \nabla) + \frac{e^2}{2mc^2}A \cdot A + V_r \tag{3.22}$$

The base Hamiltonian can be refereed as written plus the potential energy of the system.

$$\hat{H_0} = \frac{-\hbar^2\nabla^2}{2m} + V_r \tag{3.23}$$

So if we substitute in equation 3.13 we obtain:

$$\hat{H} = \hat{H_0} + \frac{i\hbar e}{mc}(A \cdot \nabla) + \frac{e^2}{2mc^2}A \cdot A \tag{3.24}$$

The weak approximation field, expressed as $\frac{e^2}{2mc^2}A \cdot A$ can be taken out of the equation, it is considered small compared to the other term. Only when a high field strength is present, this term should be considered. In this case, the Coulomb gauge presents us with $\nabla.A = 0$ so the interaction energy is represented as $A \cdot P$, and equation 3.24 becomes

$$\hat{H} = \hat{H_0} - \frac{e}{mc}(A \cdot P) \tag{3.25}$$

$$\hat{H} = \hat{H_0} + V(t) \tag{3.26}$$

$$V(t) = -\frac{e}{mc}(A \cdot P) \tag{3.27}$$

This results in the Light-Matter Interaction Hamiltonian sometimes called *veocity gauge* or $v \cdot A$ which describes the coupling between one electron and electromagnetic field this being the basis of this work.

3.3 The Band-Gap

The energy gap, or Band gap of a material [KRANE 1996] can be represented with its band structure, a material band structure is the conformation of the material

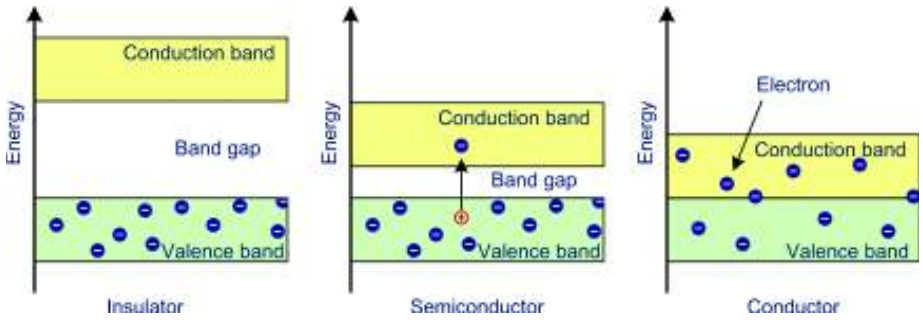

Figure 3.3: Band gap representation of a conductor, semiconductor and insulator material. [Yusoff 2016]

valence and conduction bands. If these bands are not superposed with each other, the separation between the valence and conduction bands will denote if the material is a conductor, semiconductor or an insulator, the energy difference between the lowest energy band of the conduction bands and the highest energy band of the valence bands is the band gap. In figure 3.3 we can see the bang gap difference between these material types, which directly translate with the material conductivity capacity, If you want to work with any type of material, whatever your intention, it is essential to know its band structure, since it gives us a large amount of information, especially in the field of photoelectronics, since, the bang gap represents the energy necessary to excite a valence electron to a conduction electron, a large band gap will make a material a good insulator, and a very small one a conductor, so it is necessary to take this type of study into account.

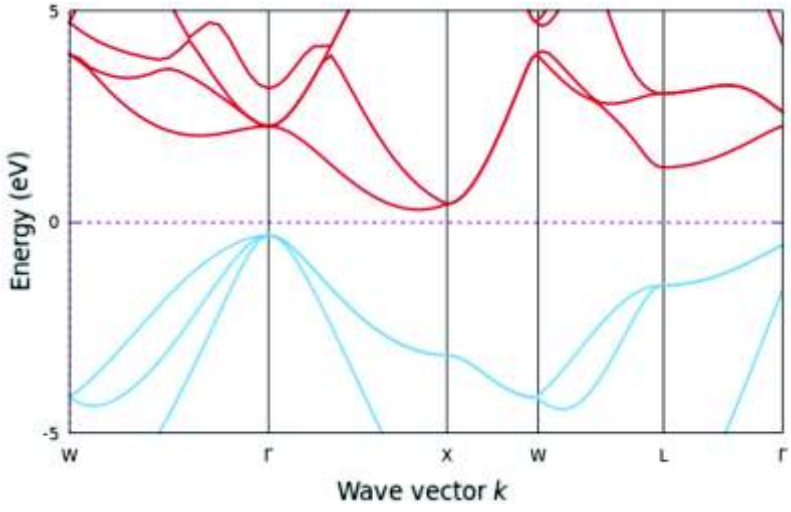

Figure 3.4: Silicon band structure along the high symmetry path of the BZ and computed within the framework of DFT. The valence bands are depicted in blue-solid line, whereas, conduction are depicted in red-solid line.

For an atomic composition to be possible, the Pauli exclusion principle must be satisfied. This principle states that no more than two electrons in an atom can occupy the same state at the same point in time, so when atoms come together to form a solid, orbitals are formed to satisfy the Pauli exclusion principle. Two orbitals are formed for each atom in the structure, one of a higher energy level, and the other one with a lower energy level. The more atoms we have in the solid, the finer the orbitals become, which creates energy bands. [Askeland 2010] The atom's electrons of the solid, will occupy these bands, filling the lowest energy levels first, these occupied levels of the structure, are called the valence states of the band structure, on the other hand, the unoccupied states, are referred to as the conduction states.

In Figure 3.4, we show the band structure for a silicon crystal, we can see in blue, the valence bands, in red, the conduction bands, and the corresponding band gap (separation) of the structure. Silicon shows an indirect band gap, which means that the valence band of maximum energy and the conduction band of minimum energy are found at different K points in space, in the case where the top of the valence and the minimum of the conduction bands are at the same point K, the band gap of the structure is known as being direct.

3.4 Density of states

The density of states (DOS) describes the number of states available in a system for a range of energy [Castillo-Quevedo 2020]. Its main use is to provide information on the concentration and energy distribution of electrons within the system. Figure 3.5 shows the distribution of the material states for Silicon bulk semiconductor, where the valence states are located below fermi level and the conduction states are located above the fermi level. The separation between the conduction and valence states is the band gap [Kittel 2004, Ashcroft 1976, Martin 2004]

The projected density of states (PDOS), which is differentiated from DOS, refers to this as the density of states contributed by each atom that makes up the material. Its importance lies in the fact that we can know the energy levels that each component dominates and, in the case of semiconductors, the effect they have on the material band gap.

3.5 Optical properties of perovkites

Optical properties provide information about the atomic structure and their electronic band structure define them [Sipe 2000, Onida 2002, Castillo-Quevedo 2020, Hybertsen 1986, Cabellos 2009a] Once we have obtained the atomic structure of the perovskites, the optical properties were computed evaluating Equation 3.29. The optical properties of materials are defined as the response that these materials have when interacting with passing electromagnetic fields (Light) [Sipe 2000, Meza 2019, Anderson 2015, Sipe 1987]. Absorption, refraction, dispersion, and transmittance are some of the possible properties. In this section of the work, there will be a

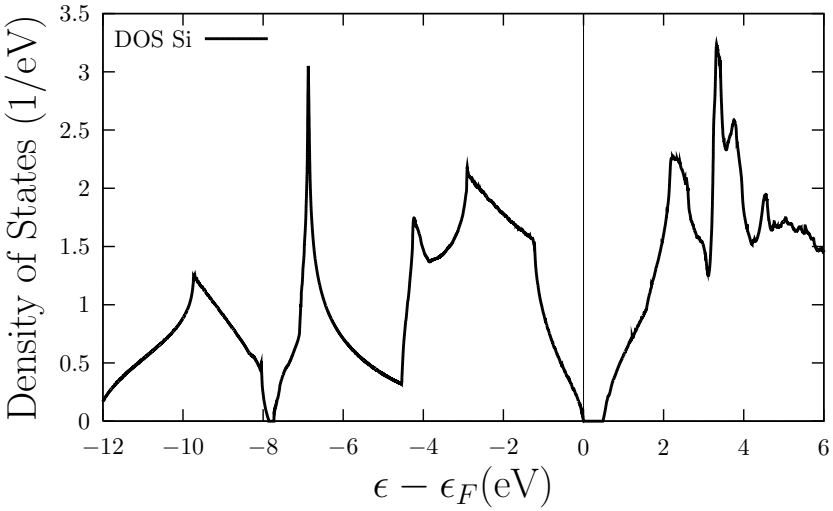

Figure 3.5: Total Density of States (DOS) of bulk silicon computed employing *Quantum Espresso* code. The Fermi energy level has shifted to the zero-energy y-axis [Cargnoni 2000].

brief presentation of the optical properties that were obtained for our investigated materials. It will be announced how they were obtained by means of a simple description of their respective equations and their importance for material study will be mentioned. A complete full Quantum derivation of *chi* based en perturbation theory is described in Appendix B

3.5.1 Linear Optical Response

Linear polarization of a material P provides a description of light interacting directly with a material when low intensity radiation is contemplated, the response function or the linear optical susceptibility χ, relates to the optical polarization to the exciting light field E [Sipe 2000, Cabellos 2009a, Bennink 1999, Gehr 1996, Fischer 1995] as

$$P^i(\omega) = P_s^i + \sum_{3}^{j=1} \chi_{ij}^{(1)}(-\omega,\omega)E^j(\omega) + \sum_{3}^{j,l=1} \chi_{ijl}^{(2)} E^j(\omega)E^l(\omega) + E^i(\omega)... \qquad (3.28)$$

The polarization of a material is expressed as the sum of the zero-field spontaneous polarization P_s^i with the summation of the of the linear optical susceptibility tensor χ [Cabellos 2009a, Sipe 2000] given in Equation 3.29, and a completly derivation is given in Appendix B

$$\chi_{ij}^{(1)}(-\omega,\omega) = \frac{e^2}{\hbar\omega} \sum_{n,m,\overrightarrow{K}} f_{mn}(\overrightarrow{K}) \frac{r_{nm}^i(\overrightarrow{K}) r_{nm}^j(\overrightarrow{K})}{\omega_{mn}(\overrightarrow{K}) - \omega} = \frac{\varepsilon_{ij}(\omega) - \delta_{ij}}{4\pi} \qquad (3.29)$$

In the Equation 3.29 n, m denote energy valence and conduction bands, respectivly, $f_{mn}(\overrightarrow{K})$ is the Fermi occupation factor, Ω is the normalization volume, $\omega_{mn}(\overrightarrow{K}) \equiv [\omega_m(\overrightarrow{K}) - \omega_n(\overrightarrow{K})]$ is the frequency difference, $\hbar\omega_n(\overrightarrow{K})$ is the energy of band n at $\overrightarrow{K}$ and $\overrightarrow{r}_{mn}$ are the matrix elements of the position operator. The latter are given by the Equations 3.30

$$\begin{aligned} r^i_{nm}(\overrightarrow{K}) &= \frac{V^i_{nm}(\overrightarrow{K})}{i\omega_{nm}}; \omega_n \neq \omega_m \\ r^i_{nm}(\overrightarrow{K}) &= 0, \omega_n = \omega_m \end{aligned} \tag{3.30}$$

where $V^i_{nm}(\overrightarrow{K}) = [P^i_{mn}(\overrightarrow{K})/m]$, m is the free electron mass, and P_{nm} is the momentum matrix element. As seen from Equation (3.3) the imaginary part $\varepsilon^{ij}_2(\omega)$ of the dielectric function, $\varepsilon_{ij}(\omega)$, is obtained by

$$E^{ij}_2 = \frac{e^2}{\hbar\pi} \sum_{n,m} d\overrightarrow{K} f_{nm}(\overrightarrow{K}) \frac{V^i_{nm}(\overrightarrow{K}) V^j_{nm}(\overrightarrow{K})}{\omega^2_{mn}} \delta(\omega - \omega_{mn}(K)) \tag{3.31}$$

Once we have the frequency defendant imaginary part ($\varepsilon^{ij}_2(\omega)$), we can use the Kramers-Kronig relation [Toll 1956] to compute the real part employing the imaginary part [Hutchings 1992, Lucarini 2005], so Kramers-Kronig gives the expression corresponding to the frequency dependent real part $\varepsilon^{ij}_1(\omega)$ of the dielectric function $\varepsilon_{ij}(\omega)$. Kramers-Kronig transform requires the frequency dependence, in a wide energy range, of ε^{ij}_2 to be able to obtain ε^{ij}_1 and the other way around [Tokmakoff 2019]. The expression obtained from the transform when applied to Equation 3.32 is

$$E^{ij}_1(\omega) - 1 = \frac{2}{\pi} P \int_0^\infty \frac{\omega' E^{ij}_2(\omega')}{\omega'^2 - \omega^2} d\omega' \tag{3.32}$$

The real ($\varepsilon_1(\omega)$) and imaginary part ($\varepsilon_2(\omega)$) of the complex dielectric constant is extremely important in terms of the optical properties of a material, it describes the ability of a medium to store an electric field during polarization. The $\varepsilon_1(\omega)$ represents the capacity of the charge storage medium, and $\varepsilon_2(\omega)$ shows the material energy loss during the process, in another words, the material absorption. Once the real part and the imaginary part of the dielectric constant have been obtained, we can obtain the following optical properties, the refractive index ($n(\omega)$), extinction coefficient ($k(\omega)$), reflectivity ($R(\omega)$), absorption coefficient ($\alpha(\omega)$) and finally the energy loss spectrum ($L(\omega)$). Each optical property is given a brief explanation of its use and the proper equation is presented to obtain it in the calculations [Sipe 2000, Chimata 2010, Mamedov 2011]

3.5.2 Refractive index

The complex refractive index is made up of its real part (n) and its imaginary part (k), which is also known as the extinction coefficient. Light changes as it passes through a medium, some can be lost if transmitted by extinction. Both change and extinction can be described by the complex refractive index [Van Krevelen 2009, Adair 1989]:

$$n^* = n' - in'' = n - ik \tag{3.33}$$

The real part of the refractive index shows us the values corresponding to the ratio of the speed of light in a vacuum to that of a different medium of higher density, in other words, n tells us the proportion of refraction light has when it passes from one medium to another, if there is none, light passes without refraction. For the case, k represents the light attenuation, or the material absorption, when its amplitude is large, the absorption of light is stronger than in the opposite case. The refractive index in perovskites can be observed by a Spectroscopic Ellipsometry and Spectrophotometry techniques [Löper 2015].

To obtain the real part of the complex refractive index from ε_2 and ε_2 we use the Equation 3.34

$$n(\omega) = \left(\frac{\sqrt{\varepsilon_1^2(\omega) + \varepsilon_2^2(\omega)} + \varepsilon_1(\omega)}{2} \right)^{1/2} \tag{3.34}$$

and for the extinction coefficient we employs the Equation 3.35

$$k(\omega) = \left(\frac{\sqrt{\varepsilon_1^2(\omega) + \varepsilon_2^2(\omega)} - \varepsilon_1(\omega)}{2} \right)^{1/2} \tag{3.35}$$

Interesting, the absorption coefficient is related to the imaginary part of the index of refraction, also called the extinction coefficient [Geist 1990] and in a previous work was observed for silicon [Geist 1990].

3.5.3 Reflectivity

The reflectivity of the material is described as the light quantity that is reflected from the material in relation to the amount of light in contact with the material surface. The object reflectance depends on the intensity of the light that comes in contact with it. The wavelength of light, the material type, and its composition also has a certain degree of impact on the total reflectivity. [Fox 2001, Green 1982]

The reflectivity depends on the real and imaginary part of the complex refractive index, as seen on the following Equation 3.36

$$R(\omega) = \frac{(n-1)^2 + k^2}{(n+1)^2 + k^2} \tag{3.36}$$

3.5.4 Absorption coefficient

The absorption coefficient (α) determines how far can light of a particular wavelength can penetrate a material before being absorbed by it [Geist 1990]. A higher absorption coefficient means that the material has a higher capacity to absorb photons, while a lower α, the light will be poorly absorbed. In semiconductors, α plays a major role in their description since light with wavelength below the forbidden band gap does not have enough energy to excite an electron to the conduction band from the top of the valence bands. If a material is thin enough, and with a low absorption coefficient, it will behave like a transparent material [Akkus 2007, Tran 1999, Hecht 2017].

In the Equation 3.37 we can see, how (α) is related to the optical constants.

$$\alpha(\omega) = 2\frac{\omega}{c}k(\omega) \tag{3.37}$$

3.5.5 Energy-loss spectrum

Electron energy-loss spectrum or (EEL spectrum) refers to the energy-loss function $-Im\varepsilon^{-1}(\omega)$ which is the response of a solid to an external electromagnetic perturbation of electron momentum transfer and energy loss [Keast 2005, Che 2008]. Examination of the low loss region of EELS spectra can provide invaluable localized information for unraveling electronic properties through analysis of spectral characteristics related to the dielectric response of the material [Sun 2016a].

The low-energy part of an EEL spectrum provides information similar to that provided by optical spectroscopy, which contains valuable information about the structure of the band and, in particular, about the dielectric properties of a material. This is especially relevant when an electron gains enough energy to traverse the energy band gap and a transition occurs from the top of the valence band to the bottom of the conduction band. This band gap transition should be the lowest energy transition in the low loss EEL spectrum, characteristic of the band structure of the material if it is undoped and flawless [Eljarrat 2016].

The EEL spectrum can be easily obtained with the use of the given Equation 3.38

$$-Im\varepsilon^{-1}(\omega) = \frac{\varepsilon_2(\omega)}{\varepsilon_2^2(\omega) + \varepsilon_1^2(\omega)} \tag{3.38}$$

In this chapter, a review of DFT beginnings and current standing has been made, denoting its importance in modern investigations and research. We analyzed the optical properties and their importance in the study of materials, focusing mostly on the real and imaginary parts of the complex dielectric constant and related properties. Also, a total deduction of the matter interaction Hamiltonian was made, which describes how light interacts with a sample. The results obtained in this work and a comparison with experimental results are presented below in order to show the efficacy of computational methods.

Chapter 4

Results and Discussion

Contents

4.1 Structural properties 28
4.1.1 Cubic perovskites 29
4.1.2 Tetragonal perovskites 31
4.1.3 Orthorhombic perovskites 31
4.2 Electronic properties 34
4.3 Bandstructure: Cubic $MAPbX_3$ (X=I, Br, Cl) 35
4.4 Bandstructure: Tetragonal $MAPbX_3$ (X=I, Br, Cl) 37
4.5 Bandstructure: Orthorhombic MAPbX (X=I, Br, Cl) . . . 38
4.6 PDOS: Cubic MAPbX (X=I, Br, Cl) 40
4.7 PDOS: Tetragonal MAPbX (X=I,Br,Cl) 44
4.8 PDOS: Orthorhombic MAPbX (X=I, Br, Cl) 44
4.9 Optical properties 45
4.10 Optics: Cubic $MAPbI_3$,$MAPbBr_3$, and $MAPbCl_3$ 47
4.11 Optical reflectivity & refractive index of cubic $MAPbI_3$ . . 49
4.12 Optical absorption coefficent of cubic $MAPbI_3$ 52
4.13 Theoretical vs experimental results 56
4.13.1 Spectroscopic Ellipsometry 57

In this chapter of this thesis, we computed the structural properties, electronic properties, and optical properties obtained for the perovskites of lead methylammonium iodide lead methylammonium chloride, and lead methylammonium bromide, in their respective cubic structural phase, tetragonal phase, and orthorhombic phases will be presented. Their results will be compared with those of other structural phases and between perovskites.

All the calculated structural, electronic, and optical properties for all perovskite structural phases were calculated using *Quantum Espresso v.6.0 open-source computer code* with the help of some implemented third party packages mentioned in the subsequent descriptions. The functional PBE was used to obtain the Exchange-correlation energy and all K-points grids were generated according to the Monkhorst-Pack scheme. For the calculations related to the optics of the materials, the k-point grid was obtained using the K point generation package, kpoints.x. These were added in the (*SCF*) input section, for the self-consistent run. For the band structure calculations, a manually specified high symmetry K-point grid was performed

and added in the input of the non-self-consistent run. Quantum Espresso was installed and used in the High-Performance Computing Area (*ACARUS* for its initials in Spanish) in the department of mathematics of the Universidad de Sonora.

4.1 Structural properties

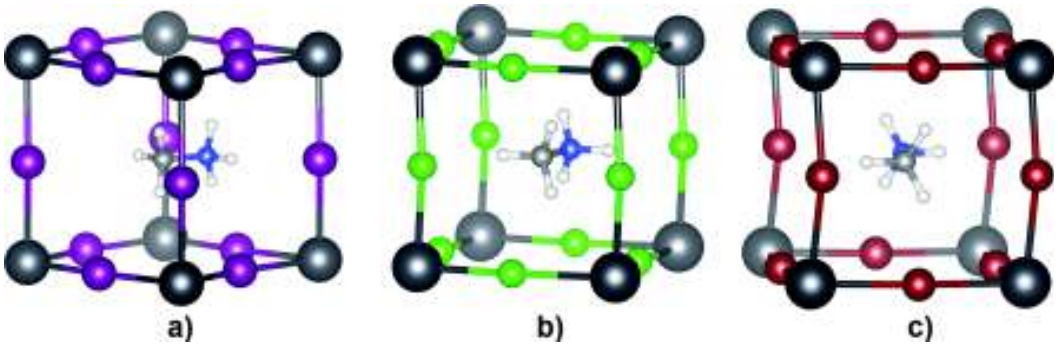

Figure 4.1: 3D structure of cubic $MAPbI_3$ (a), $MAPbCl_3$ (b), $MAPbBr_3$ (c). The violet, the green, and the copper color spheres represent the Bromide, Chloride, Iodide, respectively, while the big-sized gray spheres represent the lead atoms. The blue and light grey spheres represent the carbon and nitrogen atoms respectively, while the small white ones are the hydrogen bonded to each atom.

Here we will see the structural parameters obtained for each of the phases, these are found in the following tables, each table referring to the three perovskites in their respective structural phase. The parameters of the cubic cell are found in table (4.1), those of the tetragonal cell in table (4.2), and, in the case of the orthorhombic phase, in the table (4.3). Our structures were assigned to the space groups with number 221 (Pm-3m) for the case of cubic cells, 140 (I4/mcm) for tetragonal cells, and 62 (Pnam) for orthorhombic cells. Also, we present three-dimensional stick and ball representation of our chosen perovskites in all their structural phases. They are presented in JMOL colors (CPK color scheme) and were captured and visualized with the software VESTA (Visualization for Electronic and Structural Analysis) 3D visualization program for structural models. The energy optimization method is used to calculate the lowest energy configuration of atoms in molecules or crystals. Typically, it uses the Broyden-Fletcher Goldfarb-Shanno algorithm (BFGS). The optimization method determines the equilibrium position of the atoms minimizing the total energy while reducing the atomic forces known as the Hellmann-Feynman forces [Dominikowska 2016]. The unit cell volume is considered in the optimization scheme, and the structural optimization energy was done by optimizing the crystal lattice constants.

4.1.1 Cubic perovskites

In this section, the geometric properties of the respective cubic perovskites are presented. The band structure, the total state density, and the projected state density were obtained, this using the Quantum Espresso programs of bands.x, dos.x and projwfc.x, respectively.

In this study, we assume that the cubic perovskite crystal structure exists at high-temperature [Suzuki 2019]. The procedure of initial optimization is as follows: Initially, we propose smaller lattice constants than the expected optimized ones, for this case was 5.5 Å, and computed the total energy with the constraints of do not move the lattice constant, however relaxing the atoms. A grid was made with the lattice constant which variated between 5.5 to 6.5 Å depending on which perovskite structure was being computed.

We then made an iteration that obtained the new total energy of the system until all points on the grid were tested, obtaining the lowest energy for each point and choosing the lowest energy point. This is a fast screening procedure that lets us obtain the lattice constant which produces the lowest energy.

Once we had the lowest energy point, we refined the results by re-optimizing the structure (vc-relax), allowing QE software the variation of the lattice constants, in the stage of the optimization scheme, the size of the wavefunction, and the number of K- points were tested, optimizing the structure while finding a balance between precision and the computational time used.

Figure 4.1a shows the unit cell of the optimized cubic cell of perovskite. The optimized lattice parameters are 6.28 Å ,5.92 Å ,5.68 Å for $MAPbI_3$, $MAPbBr_3$, and $MAPbCl_3$, respectively, this is in good agreement with previous theoretical works [Li 2016], results were approximately 1.6% smaller than reported experimental ones [Oku 2015]. We employed the Perdew-Burke-Ernzerhof exchange-correlation functional because PBE obtained results reasonably agree with experimental values [Matsushita 2011]. In contrast, hybrid functionals increase the computational cost by one order of magnitude.

The lattice constants for the cubic structures are shown in the first row of the Table 4.1.1.

Cubic perovskite	a (Å)	Unit-cell volume ($Å^3$)	Exp a (Å)
$MAPbI_3$	6.288	248.67	6.391 [Oku 2015]
$MAPbBr_3$	5.920	207.47	5.933 [Oku 2015]
$MAPbCl_3$	5.680	183.25	5.666 [Oku 2015]

Table 4.1: Calculated structural parameters for the cubic perovskite phases. Experimental parameters are shown for reference. For cubic structural phase: a=b=c. Cubic perovskite parameters. The table also shows a comparison of experimental parameters for each cubic cell.

The perovskites form the symmetrical cubic structure shown in Figure 4.1 if the relative covalent radii of the constituents atoms meet a restricted criteria range; they are going to be more symmetrical structures. [Kieslich 2014, Green 2015]. Figure 4.1 (a) shows the less distorted geometry with the iodide atoms, which have a covalent radius of 1.14 Å , whereas the Pb atom has a covalent radius of 1.47 Å; the relation between both atoms is 0.77; (b) shows the relation between Cl and Pb, which is 0.67; in contrast, the relation Pb and Br atoms is 0.90.

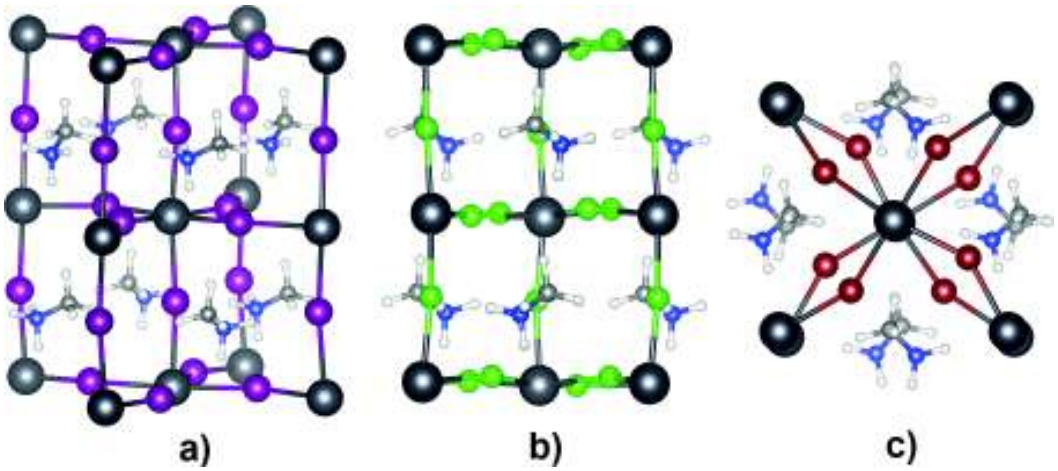

Figure 4.2: 3D structure of tetragonal $MAPbI_3$ (a), $MAPbCl_3$ (b), $MAPbBr_3$ (c). The violet, the green, and the copper color spheres represent the Bromide, Chloride, Iodide, respectively, while the big-sized gray spheres represent the lead atoms. The blue and light grey spheres represent the carbon and nitrogen atoms respectively, while the small white ones are the hydrogen bonded to each atom.

The tolerance factor can be expressed as a function of covalent radii of A, B, and X site ions, given by the Equation 4.1

$$t = \frac{1}{\sqrt{2}} \frac{(R_A + R_X)}{(R_B + R_X)} \tag{4.1}$$

Our results show that the larger the relation between atoms, the smaller is the distortion. The covalent radius of atoms I, Br, and Cl are directly correlated with the volume of the cell, this can be seen in Table 4.1.1, The second row shows the unit cell volumes for $MAPbI_3$, $MAPbBr_3$, and $MAPbCl_3$ perovskites with 249 $Å^3$, 208 $Å^3$, and 183 $Å^3$, respectively. So strictly speaking, in order to maintain a high-symmetry cubic structure, a tolerance factor t of 1 should be defined. Where R_A, R_B, and R_X are the covalent radii of the corresponding ions. The larger is the deviation from the ideal value t, the larger distorted the crystal would be, and its corresponding symmetry would be lowered. Therefore, to satisfy the ideal tolerance factor, the A-site ion must be much larger than the B-site ion. In the case of halide perovskites, in general, a large Pb or Sn atom occupies the B site; hence

the cation at the A-site must be extremely large. At finite temperature, the cubic structure may exist when t lies between 0.67 and 1, and smaller t (for example t $<$ 0.90) could result in a tetragonal structure with lower symmetry or orthorhombic crystal structure. On the other hand, a larger t (> 1), could threaten the perovskite structure. It is important to mention that DFT calculations computed at zero temperature have revealed that the orthorhombic is the most stable structure and the cubic one is the least stable since it is very difficult to satisfy the ideal condition $t = 1$. However, transitions between those crystal structures often occur in most perovskites at defined temperatures.

4.1.2 Tetragonal perovskites

Figure 4.2 a show the three dimensional unit cell of the optimized tetragonal perovskites. Following this, in Table 4.2 we can find the optimized lattice parameters for the tetragonal structural phase for all three perovskites. For $MAPbI_3$ the tetragonal structure lattice parameters are found in the first row, and they are a = 8.695 Å and c = 12.834 Å with a unit cell volume of 6500 Å^3, $MAPbBr_3$, in the second row, has the lattice parameters a = 8.032 Å and c = 11.864 Å with a unit cell volume of 5165.54 Å^3, and $MAPbCl_3$, at the last row, has the lattice parameters a = 7.709 Å and c = 11.380 Å with the smallest cell volume of 4554.11 Å^3. The optimized lattice constant show good agreement with the experimental data [Oku 2015, Mosconi 2016].

Tetragonal	a (Å)	c (Å)	Volume (Å^3)	Exp. (Å)
$MAPbI_3$	8.695	12.834	6548.60	a=8.800 c=12.685 [Oku 2015]
$MAPbBr_3$	8.032	11.864	5165.54	a=8.320 c=11.830 [Mosconi 2016]
$MAPbCl_3$	7.709	11.380	4554.11	a=8.020 c=11.260 [Mosconi 2016]

Table 4.2: Calculated lattice constants of tetragonal phase parameters with their experimental parameters reference for each perovskite. For the tetragonal structural parameters: a=b≠c.

The Figure 4.2 shows a top view of the unit cell for perovskite with bromine (c), it is interesting to highlight the orientation of the methylammonium molecules in the cell, this behavior is present in all three tetragonal perovskites, for this case of a tetragonal cell, the methylammonium seems to take a cross arrangement when seen in that plane view.

4.1.3 Orthorhombic perovskites

Figure 4.3 a shows the unit cell of the optimized orthorhombic perovskites and the orthorhombic optimized lattice parameters can be found in Table 4.3. Orthorhombic structure shows that for its lattice parameters For $MAPbI_3$ the tetragonal structure

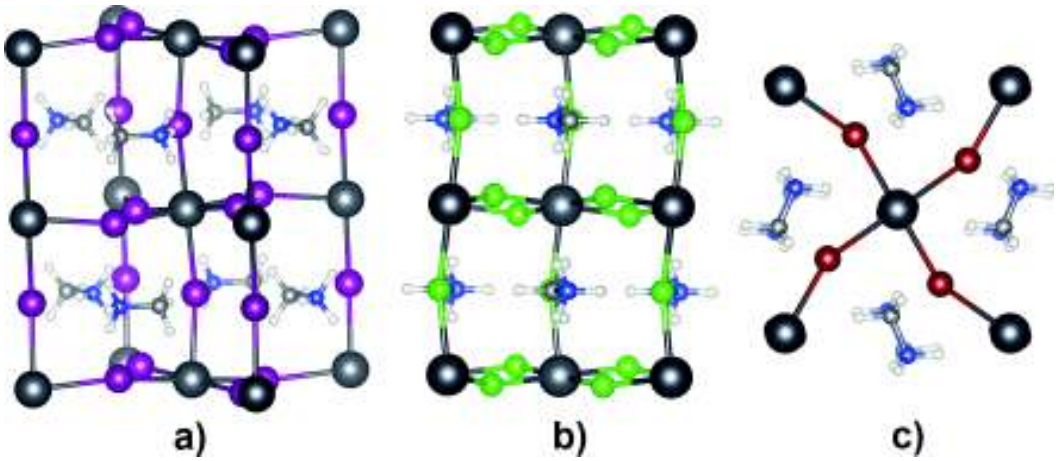

Figure 4.3: 3D structure of orthorhombic $MAPbI_3$ (a), $MAPbCl_3$ (b), $MAPbBr_3$ (c). The violet, the green, and the copper color spheres represent the Bromide, Chloride, Iodide, respectively, while the big-sized gray spheres represent the lead atoms. The blue and light grey spheres represent the carbon and nitrogen atoms respectively, while the small white ones are the hydrogen bonded to each atom.

lattice parameters are $a = 8.354$ Å, $b = 9.043$ Å, and $c = 12.661$ Åwith a unit cell volume of 6455.20 Å^3, $MAPbBr_3$, has the lattice parameters $a = 7.673$ Å, $b = 8.448$ Å, and $c = 11.692$ Åwith a cell volume of 5114.90 Å^3, and $MAPbCl_3$, at the last row, has the lattice parameters $a = 7.303$ Å, $b = 8.200$ Å, and and $c = 11.174$ Åwith a cell volume of 4516.35 Å^3. Again showing that obtained parameters are closely related to the experimental parameters [Oku 2015, Mashiyama 2006, Wang 2016].

Orthorhombic	a (Å)	b (Å)	c(Å)	Volume (Å^3)	Exp. (Å)
$MAPbI_3$	8.354	9.043	12.661	6455.20	a=8.836, b=8.555, c=12.580
$MAPbBr_3$	7.673	8.448	11.692	5114.90	a=7.976, b=8.565, c=11.841
$MAPbCl_3$	7.303	8.200	11.174	4516.35	a=7.549, b=7.835, c=11.062

Table 4.3: Computed lattice constants of orthorhombic phase parameters with their experimental parameters reference for each perovskite. For the orthorhombic structural parameters: a≠b≠c.

All the computations of the lattice constant for the nine perovskites show good agreement with the experimental data. As we mentioned earlier, temperature plays a decisive role in the geometrical structure. The DFT calculations are typically conducted at zero temperature from the theoretical perspective, whereas experiments are performed at non-zero temperatures. Despite that, the computed lattice constant are in excellent agreement with the observed lattice constants.

We can observe in Figure 4.3, in the case of the bromine cell (c), which shows a top view, the molecules are aligned in the same plane, showing different behavior from the crossed alignment that was observed in the tetragonal cells.

4.2 Electronic properties

In this section, the electronic properties of the respective perovskites are presented. The band structure, the total density of states (DOS), and the projected density of states (PDOS) density were computed using the *Quantum Espresso* programs of *bands.x*, *dos.x* and *projwfc.x* respectively.

In the last decade, hybrid organic-inorganic perovskites have attracted a lot of attention as the main active material in solar cells, due mainly two factors: the hybrid organic-inorganic perovskites have demonstrated strong light absorption and low-cost fabrication process [Burschka 2013, Huang 2021, Wu 2018a, Jeon 2014a, Lee 2012, Eswaramoorthy 2020] Furthermore, the hybrid methylammonium lead iodide perovskite exhibit high carrier mobility, and excellent carrier diffusion lengths larger than 1 μm [Stranks 2013, Herz 2017, Xing 2013], characteristics essentials for the development of electronic devices.

In previous theoretical work, Motta et al. [Motta 2015] employing the Boltzmann theory for diffusive transport in the relaxation time approximation, reported the mobility of electrons in the range 5-10 $cm^2\ V^{-1}s^{-1}$, which are in good agreement with recent experiments where the relaxation time observed is about 1 ps [Motta 2015]. The mobility of electrons for Silicon is 331 cm^2/Vs [Uprety 2019]. Additionally, and most importantly, the bulk perovskite methylammonium lead iodide has reached an efficiency larger than 22% [Yang 2017]. Due to these interesting properties, perovskites could become competitive to silicon-based solar cells. But, we have to point out that perovskites have a major drawback related to the chemical stability of methylammonium; thermodynamic considerations indicate that degradation under H_2O is highly favored [Senocrate 2019], albeit in principle preventable by encapsulation. The mentioned above is a big challenge that must be solved. Once this is solved, the perovskites, as we mentioned earlier, could become competitive to silicon-based solar cells.

To improve the efficiency of the perovskite solar material, it is necessary and mandatory to study and understand its electronic properties. However, there are few experimental works on the determination of band structure in hybrid organic-inorganic perovskites. A clear and deep understanding of the band structure is critical to understand solar light absorption and the charge carrier transport, among other properties in the perovskite materials.

Theoretical computations provide a first estimate of the band structure, previous studies compute the band structure of several perovskites employing advanced approximations as GW [Tao 2017, Filip 2018]. However, when we compute the band structure, we should pay special attention to the effective mass [Yang 2018, Yu 2016] because this determines the band flatness, the electronic localization, and the charge mobility inside the material [Castillo-Quevedo 2020]. Moreover, the band flatness is related to superconductivity [Castillo-Quevedo 2020]. In the next section, we present and discuss the electronic structure and PDOS for the perovskites.

4.3 Bandstructure: Cubic $MAPbX_3$ (X=I, Br, Cl)

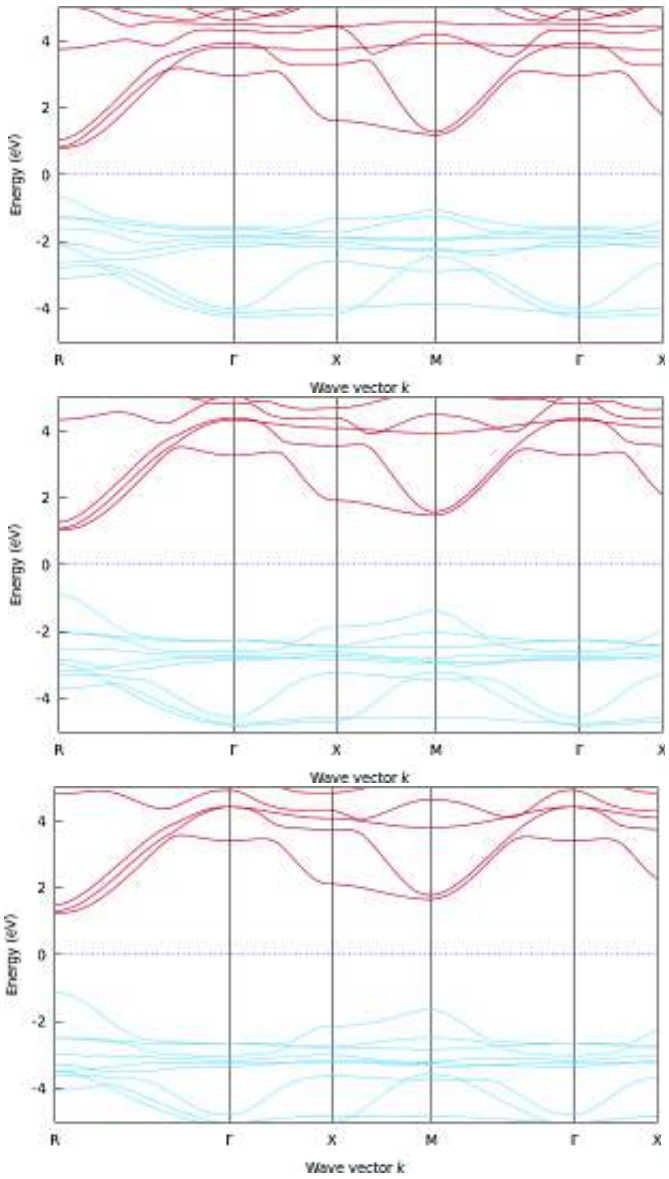

Figure 4.4: The upper panel shows the band structure of the primitive cell for cubic $MAPbI_3$ along with the high-symmetry directions (HSD) on the Brillouin zone (BZ) R-Γ-X-M-Γ-X. The middle panel shows the computed band structure along the same HSD on BZ, employing the primitive cell for a cubic $MAPbBr_3$, and the lower panel shows the computed band structure along the same HSD on BZ, employing the primitive cell for the cubic $MAPbCl._3$. The blue-solid lines correspond to the valence bands and the red-solid lines correspond to the conduction bands. We show the band structure without an applied scissors correction.

In our calculations of the band structure, DOS and PDOS, we have used the DFT methodology as implemented in Quantum Espresso code, particularly with the codes of bands.x, dos.x and projwfc.x respectively.

We show in Figure 4.4 the band structure for the Cubic $MAPbI_3$ (upper panel), $MAPbBr_3$ (middle panel) , and $MAPbCl_3$ (lower panel), computed along high-symmetry directions in the BZ, from R to X, passing to the center of the BZ, Γ, with the coordinates beign for: R [0.5,0.5,0.5], Γ [0,0,0], X [0,0.5,0], M [0.5,0.5,0], Γ[0,0,0], and X [0,0.5,0] in units of $2\pi/a$ where Â¨aÂ¨, is the lattice constants shown in Table 4.1.1.

The lowest direct Kohn-Sham band gap obtained belongs to the structure $MAPbI_3$, it was 1.47 eV at R point, $MAPbBr_3$ presented a bang gap of 1.95 eV at R point, whereas, for $MAPbCl_3$ structure is 2.36 eV. According to Ahmed et al. [Ahmed 2014] for the $MAPbI_3$ structure, the bandgap observed is 1.6 eV, while $MAPbBr_3$ and $MAPbCl_3$ have a bang gap of 2.24 and 2.97 eV respectively [Leguy 2016]. For $MAPbI_3$ observed value is 8% smaller than our computed value. In these calculations, the bandgap is underestimated by 0.14 eV compared with the experimental value of 1.6 eV; hence the scissors correction is 0.14 eV. To correct the bandgap that DFT underestimated, we applied a scissor correction of 0.14 eV to the conduction bands, which shifted them to the experimental value. For the other two cases a scissors correction of 0.29 eV for cubic $MAPbBr_3$ and 0.61 eV for $MAPbCl_3$ was applied. Remarkably, the largest Kohn-Sham band gap is correlated with the structure that has the most electronegative atom, the Chlorine atom in the unit cell $MAPbCl_3$. Furthermore, the band gaps of the structures $MAPbBr_3$ and $MAPbI_3$, follow the same trend.

In Figure 4.4 the valence bands are depicted in blue-solid lines, whereas the conduction bands are depicted in red-solid lines. In the upper panel, we can see that the top valence bands of the $MAPbI_3$ system tend to be the flattest. A direct comparison of with the top valence bands of the $MAPbBr_3$ and $MAPbCl_3$ systems shown in the middle and lower panels, respectively, indicate that the most flats valence bands belong to the $MAPbI_3$ system that also is correlated to the low electronegative atom.

Flat electronic bands produce a "pointy" density of states and are related to the superconductivity; we also have that the velocity of the electrons is related to the derivative of the band structure against the wavevector, hence the flatter the bands are, the lower the velocity of the hole or electron. Analysis of results in more detail leads to interesting observations: the $MAPbI_3$ has the lowest hole velocity based on the observation of the valence bands, and that is correlated with the electronegativity of the atom, more electronegative is the atom, a larger dispersion in the band structure. The above-mentioned is one of the most important results found in my thesis. In Figure 4.4 the valence bands are depicted in blue-solid lines, a bunch of them are located in a range of 0 to -4 eV for the $MAPbI_3$ system, in contrast for the case of the $MAPbBr_3$ and $MAPbCl_3$ systems, the range increase is from 0 to -5 eV. Regarding the conduction bands depicted in red-solid lines, there is a large dispersion around the R and M high symmetry K-points, and some of them are located in the energy range of 0 to 4 eV.

4.4 Bandstructure: Tetragonal $MAPbX_3$ (X=I, Br, Cl)

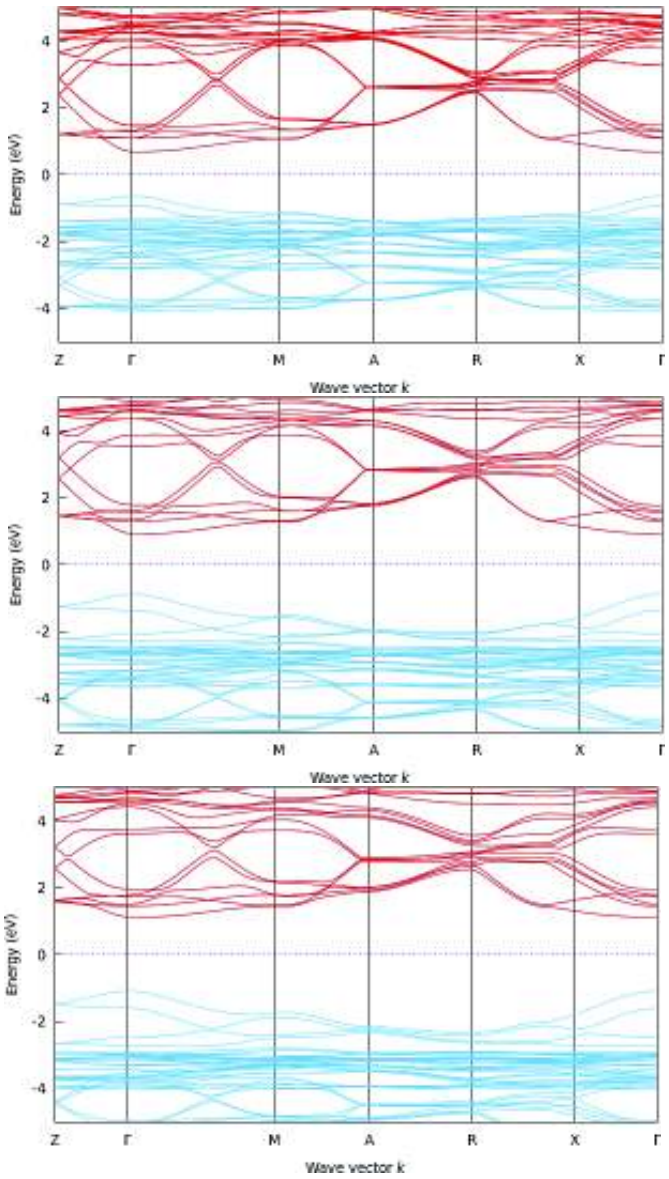

Figure 4.5: The upper panel shows the band structure of the tetragonal primitive cell $MAPbI_3$ along with the HSD on the BZ Z-Γ-M-A-R-X-Γ. The middle panel shows the computed band structure along the same HSD on BZ, employing the primitive cell for a tetragonal $MAPbBr_3$, and the lower panel shows the computed band structure along the same HSD on BZ, employing the primitive cell for the tetragonal $MAPbCl_3$. The blue-solid lines correspond to the valence bands and the red-solid lines correspond to the conduction bands. We show the band structure without an applied scissors correction.

In Figure 4.5 the band structure for the tetragonal $MAPbI_3$ (upper panel), $MAPbBr_3$ (middle panel), and $MAPbCl_3$ (lower panel). The band structure was computed along high-symmetry directions in the BZ, following the coordinates for: Z [0,0,0.5], Γ [0,0,0], M [0.5,0.5,0], A [0.5,0.5,0.5], R [0,0.5,0.5], X [0,0.5,0], and Γ [0,0,0] in units of $2\pi/a$ where Â¨aÂ¨, is the lattice constants shown in Table 4.2. As seen for the cubic structures, $MAPbI_3$ showed the lowest gap of 1.30 eV at the Γ point, $MAPbBr_3$ presented a bang gap of 1.80 eV at Γ point, and $MAPbCl_3$, presented a band gap of 2.21 eV. Reference [Leguy 2016] tells us that the experimental gap of tetragonal $MAPbI_3$ is 1.55 eV. Our computed value is approximately being underestimated by 16 %, double than the cubic perovskite case. The scissors correction is 0.25 eV for the $MAPbI_3$ tetragonal perovskite. To our knowledge, there is not quality reported experimental band gap data for the $MAPbCl_3$ and $MAPbBr_3$ tetragonal structures, in consequence, the cases of Cl and Br cases is not possible to estimate with the scissors correction. A comparison between the three band structures, in Figure 4.5, showed us that $MAPbI_3$ has the flattest valence bands of all tetragonal structures, this was the same result for the cubic case. Observing the valence bands (blue lines), we can see their displacement between perovskites in the range of -2 and -4 eV.

4.5 Bandstructure: Orthorhombic MAPbX (X=I, Br, Cl)

The orthorhombic band structure can be seen in Figure 4.6 for $MAPbI_3$ (upper panel), $MAPbBr_3$ (middle panel), and $MAPbCl_3$ (lower panel). The band structure was computed along high-symmetry directions in the BZ, following the coordinates for: G [0,0,0], X [0.5,0,0], S [0.5,0.5,0], Y [0,0.5,0], Γ [0,0,0], Z [0,0,0.5], U [0.5,0,0.5], R [0.5,0.5,0.5], T [0,0.5,0.5], Z [0,0,0.5], and Γ [0,0,0] in units of $2\pi/a$ where a, is the lattice constants shown in Table 4.3.

Following the same trend as the cubic and tetragonal structures, orthorhombic $MAPbI_3$ showed the lowest gap of 1.45 eV at the Γ point, $MAPbBr_3$ presented a band gap of 1.89 eV at Γ point, and $MAPbCl_3$, has the highest gap of 2.17 eV. Again to our knowledge, we couldn't find reported experimental band gap data for all three orthorhombic structural phase perovskites.

As for the valence bands in Figure 4.6, $MAPbI_3$ has the flattest valence bands of all orthorhombic structures, this is a shared behavior observed independent of the structural perovskite phase.

In the upper panel of Figure 4.6, we can observe that the bandwidth of the valence bands (blue lines), is in the ranging energy from 0 to -4 eV for the case of the perovskite with iodine in its stature, for the Br perovskite the bandwidth shifts to the range of 0 to -4.5 eV, and for the Cl perovskite, the bandwidth shift from 0 to -5 eV. With the comparison made, we can say that for the three cases, the band structure is very similar. It is noteworthy that the difference among them is the values of the band gap.

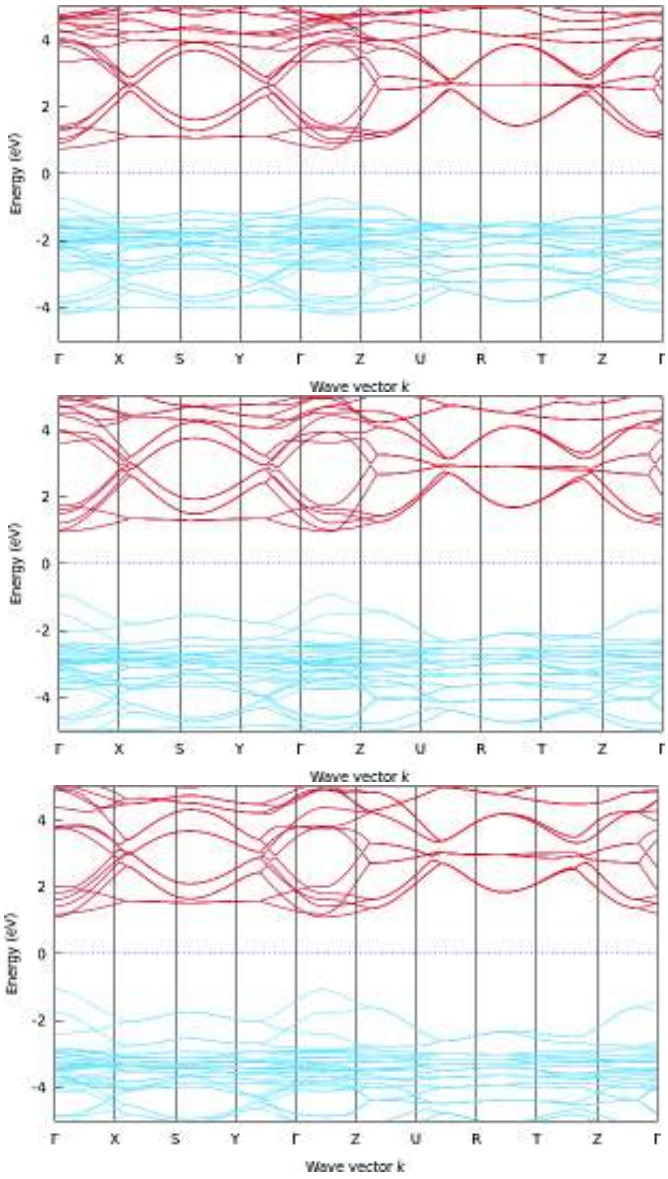

Figure 4.6: The upper panel shows the band structure of the orthorhombic primitive cell $MAPbI_3$ along with the HSD on the BZ Γ-X-S-Y-Γ-Z-U-R-T-Z-Γ. The middle panel shows the computed band structure along the same HSD on BZ, employing the primitive cell for a orthorhombic $MAPbBr_3$, and the lower panel shows the computed band structure along the same HSD on the BZ, employing the primitive cell for the orthorhombic $MAPbCl_3$. The blue-solid lines correspond to the valence bands and the red-solid lines correspond to the conduction bands. We show the band structure without an applied scissors correction.

4.6 PDOS: Cubic MAPbX (X=I, Br, Cl)

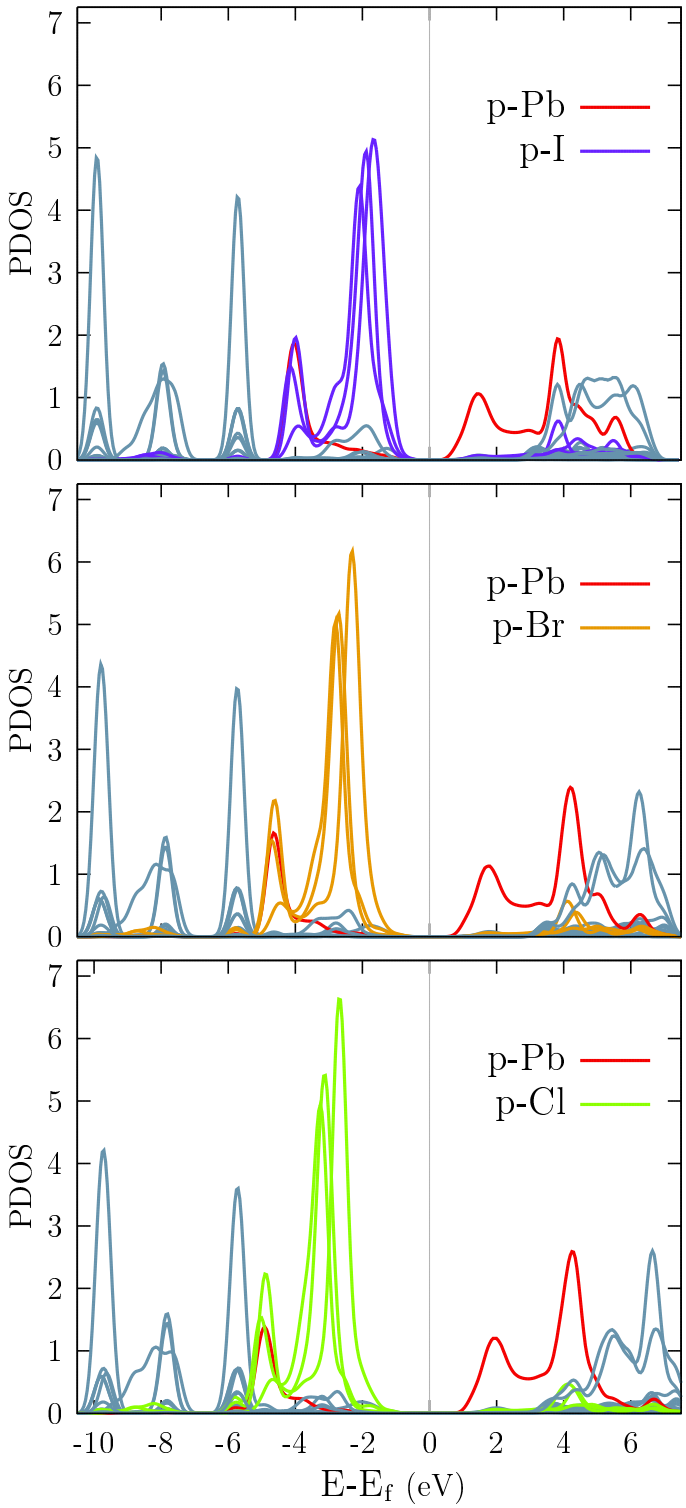

Figure 4.7: The upper panel shows the Kohn-Sham projected density of states (PDOS) for the cubic $MAPbI_3$ structure. The middle panel shows the PDOS for the cubic $MAPbBr_3$ structure, and the lower panel shows the PDOS for the cubic $MAPbCl_3$ structure. In all plots, the Fermi energy is shifted to zero.

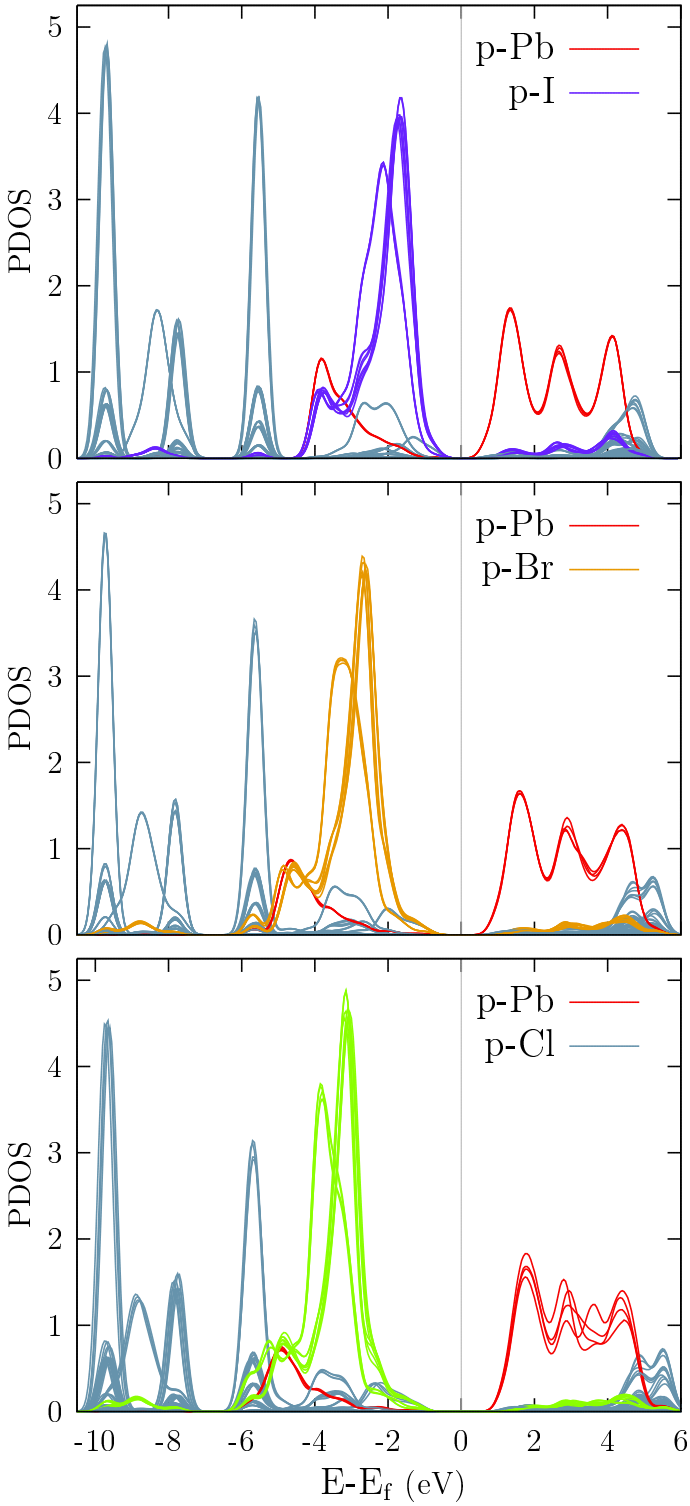

Figure 4.8: The upper panel shows the Kohn-Sham projected density of states (PDOS) for the tetragonal $MAPbI_3$ structure. The middle panel shows the PDOS for the tetragonal $MAPbBr_3$ structure, and the lower panel shows the PDOS for the tetragonal $MAPbCl_3$ structure. In all plots, the Fermi energy is shifted to zero.

To elucidate the nature of the electronic band structure, we calculated the density of states (DOS) and projected density of states (PDOS) as a function of energy for for the $MAPbI_3$ $MAPbBr_3$ and $MAPbCl_3$ systems.

Figure 4.7 display the PDOS for the three cubic systems. The upper panel of Figure 4.7 shows the Kohn-Sham projected density of states (PDOS) for the $MAPbI_3$ structure where the Fermi energy is shifted to zero. Notice, that it is zero in the range of bandgap. The examination of the PDOS shows that the width of valence bands is approximately 3 eV, Moreover, the PDOS showed the highest valence bands are mainly formed by a mix of p states from the Iodine and p and s states from lead. The p-Iodine states are depicted in purple-solid line, whereas p-lead states are depicted in red-solid line. In the Figure, one can see the p-lead states strongly dominate at the Fermi level with a slight mixture of methylammonium, so the charge transfer is null between the Pb and methylammonium. Remarkably, the methylammonium states are located below of -5 eV, they are very far away from the Fermi level, so they do not participate in the optical transitions at low energy. Regarding, the conduction bands, the lowest conduction band is mainly formed by the p-lead states, as a consequence the onset of the optical absorption should be dominated by the lead and Iodine atoms.

The upper panel of Figure 4.7 shows the Kohn-Sham projected density of states for the $MAPbBr_3$ structure where the Fermi energy is shifted to zero. A closer examination of the PDOS shows that the width of valence bands is approximately 4 eV, slightly larger than the $MAPbI_3$ structure. Moreover, the PDOS shown the highest valence bands are mainly formed by a mix of p states from the Br atom and lead p and s states.

The p-Br states are depicted in yellow-solid line, whereas p-lead states are depicted in red-solid line. Also, the methylammonium states are located below -5.5 eV, similar to the Iodine case, they are very far away from the Fermi level, so they do no take participate in the optical transitions at low energy. Regarding the conduction bands, the lowest conduction band is mainly formed by the p-lead states, as a consequence the onset of the optical absorption should be dominated by the lead and Br atoms.

The $MAPbCl_3$ structure, shows a very similar behavior than the $MAPbI_3$ and $MAPbBr_3$ cases. The lower panel of Figure 4.7 shows the Kohn-Sham projected density of states for the $MAPbCl_3$ structure where the Fermi energy is shifted to zero. A closer examination of the PDOS shows that the width of valence bands is approximately 4.5 eV, slightly larger than the $MAPbI_3$ and $MAPbBr_3$ structures. Moreover, the PDOS shown the highest valence bands are mainly formed by a mix of p states from the Br atom and lead p and s states.

The p-Cl states are depicted in green-solid line, whereas p-lead states are depicted in red-solid line. The methylammonium states are located below -5.5 eV, very far from the Fermi level, so they do not participate in the optical transitions at low energy. Regarding, the conduction bands, the lowest conduction band is mainly formed by the p-lead states, as consequence, the onset of the optical absorption is dominated by the lead and Cl atoms.

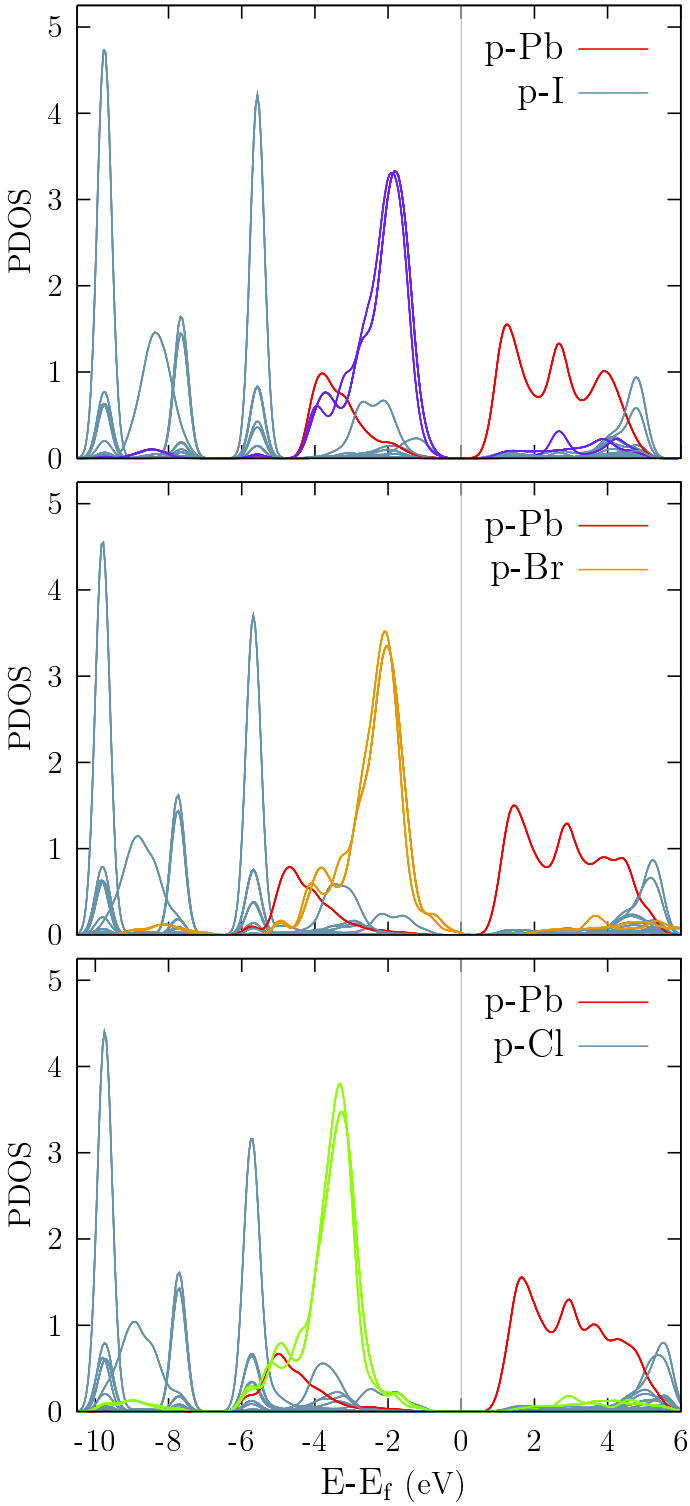

Figure 4.9: The upper panel shows the Kohn-Sham projected density of states (PDOS) for the $MAPbI_3$ structure. The middle panel shows the PDOS for the $MAPbBr_3$ structure, and the lower panel shows the PDOS for the $MAPbCl_3$ structure. All three perovskites are in their orthorhombic structural phase, and their Fermi energy is shifted to zero.

4.7 PDOS: Tetragonal MAPbX (X=I,Br,Cl)

Figure 4.8 display the PDOS for the three tetragonal systems. The upper panel of shows the Kohn-Sham PDOS for the $MAPbI_3$ structure, $MAPbBr_3$ being the middle one and $MAPbCl_3$ the bottom one. The Fermi energy is shifted to zero.

As explained before, the valence bands are dominated by a mix of p states from the halogen and p and s states from the lead atoms, while the conduction bands are totally dominated by p-lead states. The methylammonium states are located very far away from the Fermi level, not participating in the optical transitions. Depending on the halogen in the perovskite structure, it can be seen, as is the case for the description in the cubic cell, that shifts of the valence states are observed in the PDOS plots. Like before, the valence band is approximately 3 eV for $MAPbI_3$, 4 eV for $MAPbBr_3$, and 4.5 eV for $MAPbCl_3$.

4.8 PDOS: Orthorhombic MAPbX (X=I, Br, Cl)

Figure 4.9 display the PDOS for the three orthorhombic systems. The upper panel of shows the Kohn-Sham PDOS for the $MAPbI_3$ structure, $MAPbBr_3$ being the middle one and $MAPbCl_3$ the bottom one. The Fermi energy is shifted to zero.

For orthorhombic structures, shifts of the valence states are observed depending on the halogen in the perovskite structure, the same can be seen for the methylammonium states which are located at -5 eV for $MAPbI_3$, and proceed to shift to -6 eV for $MAPbCl_3$, $MAPbBr_3$ located in between. For the valence and conduction states that dominate the region close to the band gap of the material. The valence bands are being dominated by a mix of p states from the halogen and p and s states from the lead atoms, while the conduction bands are dominated almost exclusively by p-lead states.

4.9 Optical properties

The electron is a charged particle that interacts with an electric field. We must point out that the electric field could be static or variable in time; light being is an electric field variable in time; the application of an electric field originating from an external source will act on the electrons just as the field of the nuclei does. If the electromagnetic field is applied to the perovskites, the electromagnetic field is considered average. From a macroscopic point of view, the electrons are screening the external field. This is the optical response which we computed in this thesis. This chapter is primarily concerned with theoretical computations of optical constants of perovskites, which are computed within the long-wavelength limit q$\rightarrow$ 0 of the dielectric function $\varepsilon(q,\omega)$. These include the complex dielectric function $\varepsilon(\omega)$, the complex index of refraction, the energy-loss function, absorption coefficient, and the optical reflectivity.

The *ab initio* calculation of the above-mentioned optical properties for many nanomaterials has been a long-standing problem in chemistry, physics, and condensed-matter physics [Ehrenreich 1959, Adler 1962, Nozières 1958, Onida 2002, Sipe 2000, Anderson 2015]. In practice, these properties are computed for only a reduced set of perovskites materials. Thus, we aim to employ and develop an efficient and widely applicable method covering a broad range of frequencies from 0 to 20 eV to compute perovskites optical properties, providing a complement for experimental data.

The dielectric response theory for periodic systems has been developed extensively in the last years [Onida 2002], among the first theoretical works on the computation of the dielectric response, that developed the theory of dielectric function within the time-dependent Hartree approximation, also known as the random phase approximation, we highlight Pines et al. [Nozières 1958], Cohen et al. [Ehrenreich 1959], Adler et al. [Adler 1962], and Wiser et al. [Wiser 1963], and recently Cabellos et al. [Cabellos 2009a] corrected the effects of DFT band gap underestimation of the optical response. Theoretical methods for accurate calculations of optical spectra are still under development. Nowadays, more advanced theories are under development that takes into account excitonic and dynamics correlation effects based on the Bethe-Salpeter equation [Onida 2002]. Moreover, the theory has been extended to include time dependent density functional theory (TDDFT) [Zangwill 1980], which includes exchange effects.

In the following, the computational details involved in the computation of optical response will be explained. The optical absorption spectrum is determined by the imaginary part of the dielectric function, [Molina-Sánchez 2013] given in Equation 4.2 which in turn is related to imaginary part of electric susceptibility [Sipe 2000] given in Eq. B.50.

$$\varepsilon^{ab}(\omega) = 1 + 4\pi\chi_1^{ab}(-\omega;\omega) \tag{4.2}$$

Following the procedure of this thesis, we computed the expression given by Eq. B.50. The peaks present in the $\mathfrak{Im}[\chi_1^{xx}(-\omega,\omega)]$ part are due to direct interband optical transitions among the valence and conduction bands. They can be identified from

the critical points of the band structure. The band structure can give major contribution to the $\mathfrak{Im}[\chi_1^{xx}(-\omega,\omega)]$ part, identified as the top valence band and lowest conduction band [Salazar 2016, Lee 2004]. Additionally, we take into account the scissors correction [Nastos 2005, Cabellos 2009a] which is obtained by a rigid shift of the DFT energies to the experimental values [Stahrenberg 2001], as consequence the spectrum of $\mathfrak{Im}[\chi_1^{ab}(-\omega,\omega)]$ is shifted along the energy axis without changing the spectrum shape. [Nastos 2005, Cabellos 2009a] The $\mathfrak{Re}[\chi_1^{ab}(-\omega,\omega)]$ part was computed using the Kramers-Kronig relations [Reshak 2012], where the indirect transitions are neglected because they represent little contribution [Okoye 2003] to $\mathfrak{Im}[\chi_1^{ab}(-\omega,\omega)]$, also the spin-orbit, local field, and electron-hole effects are also neglected. [Leitsmann 2005, Cabellos 2009a], we express that the inclusion of these effects, is beyond the scope of this thesis work.

The wavefunctions were expanded in plane waves basis set and checked for convergence applying kinetic cutoff energy of 15 Hartree. The Monkhorst-Pack scheme was used [Monkhorst 1976] to sample the Irreducible Brillouin Zone (IBZ). To ensure that the optical properties converged. The total energy SCF tolerance was set to a value of $2\text{x}10^{-8}$ eV/atom. It is important to mention that there are several parts of the input file of QE, code calculation, data structure, parameter data, k-points, and pseudopotential files, that had to be tested until finding values that would allow a quality calculation. The perovskites are defined in the structure data, where the parameter data contains quantities such as kinetic energy cut-off (ecutwfc), the k-points sampling, the IBZ, and the pseudopotential files obtained directly from the QE website. Special care had to be taken with kinetic energy cut-off (ecutwfc) and the k-point mesh to get converged calculation for the perovskites.

Calculating optical properties is very sensible to the kinetic energy cut-off (*ecutwfc*), so, the optimization was done looking to get the best balance between the computation efficiency and maintaining the computation accuracy. A large cutoff energy is more exact is the optics calculation for periodic systems, like our perovskites materials. The plane wave is expressed by the Equation 4.3.

$$\psi_{nk}(\mathbf{r}) = \sum_{\mathbf{G}} C_{nk}(\mathbf{G}) e^{i(\mathbf{k}+\mathbf{G})\mathbf{r}} \tag{4.3}$$

Where $C_{nk}(\mathbf{G})$ are the plane wave coefficient, where $\mathbf{G}$ is a reciprocal lattice vector. The energy cut-off, limits these $\mathbf{G}$ vectors. (it is impossible that they are infinite) and it is given by Equation 4.4

$$\frac{\hbar|\mathbf{k}+\mathbf{G}|^2}{2m} \leqslant E_{cut} \tag{4.4}$$

The *ecutwfc* value employed in optics computation was 40 Rydberg. In the k-point optimization, we practically limit only a finite number of k plane waves. The summation in limited IBZ sampling was adapted where we used the mesh variation, that depends on the perovskite, k1×k2× k3 from 1× 1 ×1 to 9×9×9 and for finding the best convergence in the optics. In the following section, we turn our attention to the perovskites optical spectra.

4.10 Optics: Cubic $MAPbI_3$,$MAPbBr_3$, and $MAPbCl_3$

In this part of the results, the optical properties calculated for perovskites of cubic structural phase are presented. The calculated optical properties of the materials can be found in the section of each respective perovskite. The real part and the imaginary part of the dielectric function were calculated using *epsilon.x* in *Quantum ESPRESSO*. Once they were obtained for the proposed K-points mesh, they were utilized to obtain the *refractive index*, the *reflectivity*, the *absorption coefficient* and finally the *Energy Loss spectrum* was calculated employing programs made in home and written using *Python* programming code.

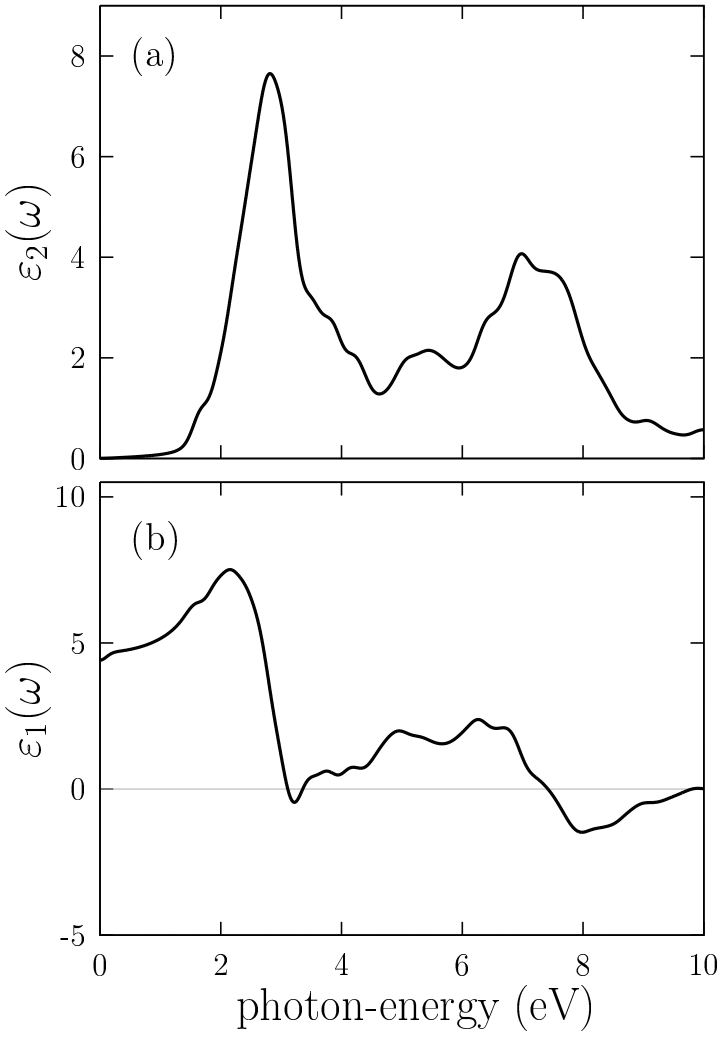

Figure 4.10: Frequency dependence of the $\varepsilon^{ab}(\omega)$ of the Cubic $MAPbI_3$. The upper panel shows the $\varepsilon_2^{ab}(\omega)$ in the ranging frequency from 0 to 10 eV, and the lower panel shows the $\varepsilon_1^{ab}(\omega)$ in the ranging frequency from 0 to 10 eV. The dielectric function is related to the imaginary part of electric susceptibility by $\varepsilon^{ab}(\omega) = 1+4\pi\chi_1^{ab}(-\omega;\omega)$.

The absorptive part of the dielectric function, $\varepsilon_2^{ab}(\omega)$ for the Cubic $MAPbI_3$ structure, is displayed in the upper panel (a) of Figure 4.10. The onset of the signal starts to rise at 1.2 eV, slightly smaller than the computed band gaps of the band structures shown in Figure 4.4 "a" where the electronic bandgap computed is 1.47 eV. This small difference is due to the excitonic effects not taken in the computation of the $\varepsilon_2^{ab}(\omega)$. In the ranging energy from 1 to 2 eV, it grows exponentially, and in the ranging energy from 2 to 2.8 eV, it presents a linearly growth.

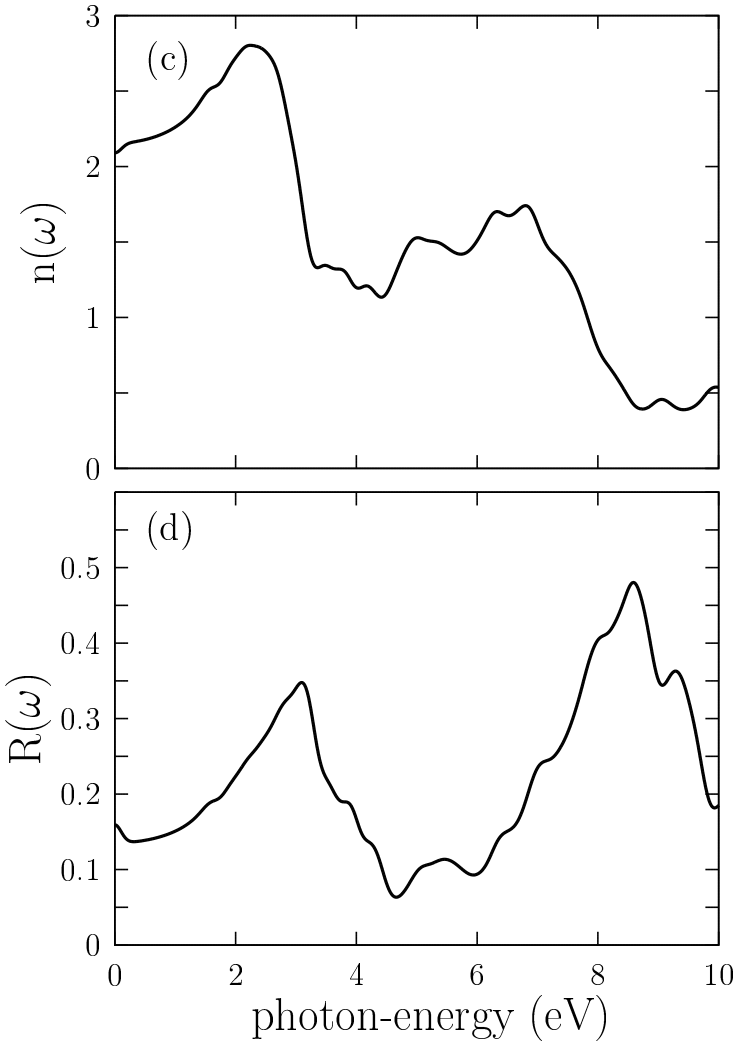

Figure 4.11: Frequency dependence of the refractive index, $n(\omega)$, and reflectivity, $R(\omega)$, of the Cubic $MAPbI_3$. The upper panel (c) shows the refractive index in the ranging energy from 0 to 10 eV, and the lower panel (d) shows the reflectivity in the ranging energy from 0 to 10 eV.

The largest peak is located at 2.8 eV of the energy range, followed by the second largest located at 7 eV. Remarkably, the largest peak ob absorption is located at the visible range of 2 and 3 eV. The onset of the signal in the energy range of 1.0 to 2

eV, which is mainly due to the direct transitions from the top-most valence bands (highest-energy valence bands) to the lowest energy conduction band localized at the Γ point. Because the cubic $MAPbI_3$ is completely isotropic, the *xx*, *yy*, and *zz* components are also isotropic. as consequence, we only present the xx component, and for the case of Cubic $MAPbI_3$, the scissor correction of 0.14 eV was applied. As we mentioned earlier, the onset of the signal is due to the optical transition between the top-most valence band to the lowest energy conduction band. According to the PDOS of the Cubic $MAPbI_3$ displayed on the upper panel of Figure 4.7, the top-most valence band is formed by *p-Iodine* states and the composition of the lowest energy conduction band is formed by the lead "p" states, which implies that the low energy part of the optical absorption spectrum displayed in the upper panel of Figure 4.10 is due to the iodine and lead atoms. The largest absorption peak located at 2.8 eV shown in the upper panel of Figure 4.10, is due to optical transitions from *p-Iodine* states to the methylammonium states located in the ranging energy from 3 to 6 eV, which can be seen in the upper panel of Figure 4.7. In summary, the methylammonium contributes to the high part of the optical absorption with transitions from the iodine states to the methylammonium states.

The lower panel (b) of Figure 4.10 shows the real part of the dielectric function, $\varepsilon_1^{ab}(\omega)$ for the cubic $MAPbI_3$ structure. We point out that the real $\varepsilon_1^{ab}(\omega)$ part provides information about the polarizability of the material. The lower panel of Figure 4.10 shows that the static value of the 4.4 u.a. ($\varepsilon_1^{ab}(0) = 4.4$). In the ranging energy from 0 to 2.1 eV. The real $\varepsilon_1^{ab}(\omega)$ part starts to increase and reach a large peak with a value of 7.8 located at 2.1 eV, after that, a rapid decrease is observed until it reaches zero. The negative values of the real $\varepsilon_1^{ab}(\omega)$ part are indicative of metallic behavior. In contrast, a change of sign in the real part indicates plasmonic resonances in the energy region where it crosses the energy axes with a positive slope.

4.11 Optical reflectivity & refractive index of cubic $MAPbI_3$

The refractive index of a material is defined as the ratio of the speed of light in a vacuum to that of in matter [Palik 1998]. The refractive index of a material is a function of the frequency, doping, thickness, and grain boundaries [Ong 2001, Ono 2018, Nenkov 2008, Lamichhane 2020], The refractive index of a perovskite in this thesis is computed using the Equation 3.34 and it is related to $\varepsilon_1^{ab}(\omega)$ trough the Equation 4.5 given as

$$n(0) = \sqrt{\varepsilon_1^{ab}(0)} \tag{4.5}$$

In panel (c) of Figure 4.12 we show the frequency dependence of the refractive index of the cubic $MAPbI_3$ in the ranging energy from 0 to 10 eV. Our computed refractive index spectra, depicted in Figure 4.12 "c", revels that the static refractive index is 2.1 ($n(0) = 2.1$) for the cubic $MAPbI_3$ perovskite. According to the lower panel (b) on Figure 4.10, the static value of $\mathfrak{Re}[\varepsilon_1^{ab}(0) = 4.4]$ so, according with Equation 4.5, the static value of the refractive index is $\sqrt{4.4}$ =2.09, which is in good agreement

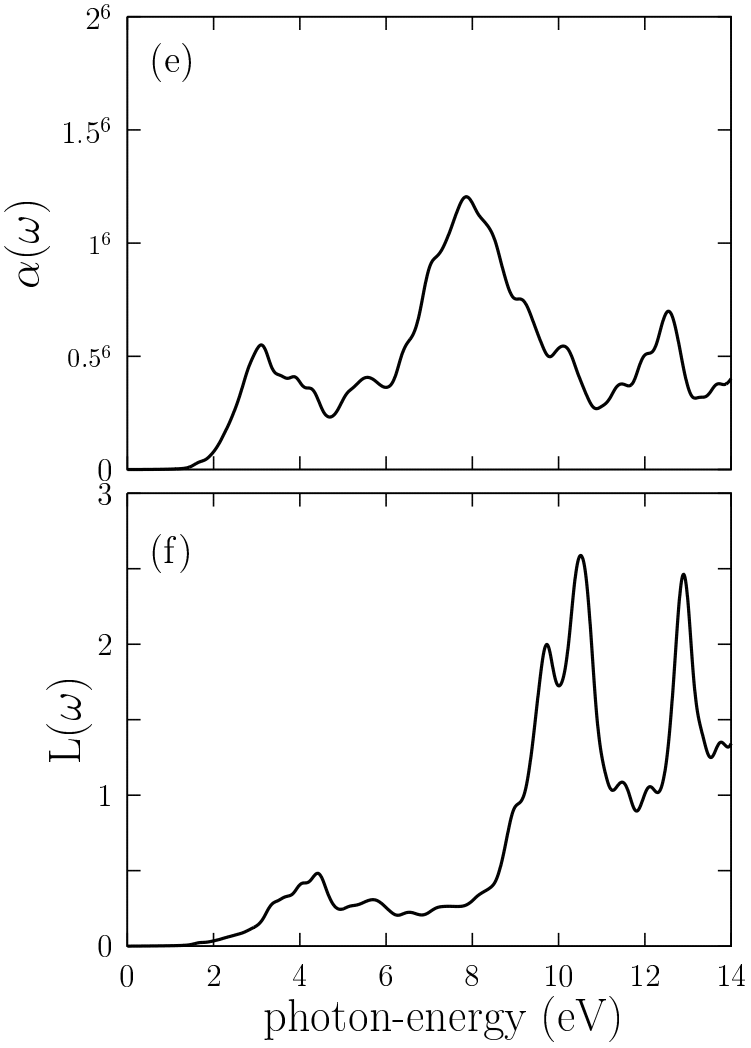

Figure 4.12: Frequency dependence of the absortion coefficient ($\alpha(\omega)$) and energy loss spectrum, L(ω), of the Cubic $MAPbI_3$. The upper panel (c) show the absortion coeficient in in the ranging energy from 0 to 14 eV. The lower panel (d) show the loss energy spectrum in the ranging energy from 0 to 14 eV.

with the static refractive index displayed in Figure 4.12c of 2.1. The above model related the static of $\mathfrak{Re}[\varepsilon_1^{ab}(0)]$ part to the refractive index, as we demostrated it perfomed well. At beginning of the 1950, Moss [Moss 1951] proposed a relationship between the electronic gap (E_g) and the refractive index (n) given in Equation 4.6,

$$n^4 E_g = 95 \text{ eV} \tag{4.6}$$

The Equation 4.6 is based on Bohr's atomic model of hydrogen. In the '90s, Herbe and Vandamme [HervÃ© 1994] formulated the Equation 4.7

$$n = \sqrt{1 + \left(\frac{A}{E_g + B}\right)} \tag{4.7}$$

where A=13.6 eV and B=3.4 eV are the constants. This Equation 4.7 agrees satisfactorily for most optoelectronic materials of the IV-VI group [Reddy 2008] Moreover, it reproduces the reported experimental values of the refractive indices of perovskites [Lamichhane 2020] For our case of cubic $MAPbI_3$ perovskite the data for the Equation 4.7 are: E_g= 1.47 eV, A= 13.6 eV, and B= 3.4 eV, so the evaluation leads to 2.97. This value is lower in almost 25% to the computed refractive index of 4.2. From the experimental point of view, there are several methods based on optical transmission and reflection measurements are used to calculate the refractive index data using the envelope, Maxwell-Garnett, and Goodman method [Sohn 2017] So far, other relations between the electronic gap and refractive index have been proposed, based on the fact that the optoelectronic properties of perovskites depend on the ionic nature by simply treating perovskites as ionic solids[Lamichhane 2020]. We let the study of these relations for a new project. The peaks in the refractive index are due to the interband transition of electrons from the valence band to the conduction band. In Figure 4.12c we can observe that at above the energy of 8 eV, the value of the refractive index is less than unity. Refractive index smaller than unity describes that group velocity, v_g of light that goes through the perovskite becomes greater than the speed of light, according to Equation 4.8

$$v_g = c/n \tag{4.8}$$

In the Equation above, c is the velocity of the light in vacuum and n the index of refraction, so at values of energy around 9 eV, the v_g is two times the velocity of light (6×10^8 cm/s). In Figure 4.12c, we can observe that the refractive index starts to increase from the static value to the largest peak located at 2 eV; after that, it decreases until it reaches 3 eV; in this region, the velocity of light increases very fast. Above 3 eV, the refractive index keeps the value around 1.5 until it reaches 7, after that, it starts to decrease, and around 8 eV, it becomes smaller than one.

In panel (d) of Figure 4.12 we show the frequency dependence of the reflectivity spectrum, $R(\omega)$, of the cubic $MAPbI_3$. Reflectivity is described as the relation equal to the ratio of incident light to a medium and the reflected light, this was computed in the range of 0 to 10 eV. In panel (d) of Figure 4.12 we observe that the static value of the reflectivity ($R(\omega = 0)$)=0.15) is 0.15. R(0) is independent of the size of cation A (MA+). The reflectivity spectrum $R(\omega)$, again, displayed in panel (d), shows a global minimum at 4.5 eV, corresponding to the plasma edge. This decrease in reflectivity may be due to plasmonic excitation [Lamichhane 2021]. As we mentioned earlier, the reflectivity spectrum has its first large peak located at 3.1 eV, which is related to the Penn bandgap. The global peak in the reflectivity spectrum is located at 8.8 eV, and at this point, the reflectivity is almost 50%, meaning that the perovskite is not absorbing 50% of the incident solar light. We

underline, that this frequency is far away from the visible spectrum that is of our interest, located between the range 1 to 3 eV.

The reflectivity spectrum in ranging energy from 0.5 to 3.1 eV, starts to increase at 3.1 eV, reaching a maximum value of 0.35, suggesting that 1/3 of the solar light is reflected. Above 3.1 eV, the reflectivity spectrum decreases until 4.5 eV, reaching a global minimum. In the ranging energy from 3.1 to 4.5 eV, the reflective spectrum is rather steep, and thus, the small energy shift leads to a significant change in the reflectivity. As we mentioned earlier, this abrupt diminution of reflectivity is related to the plasmon frequency. Moreover, at 4.5 eV, the reflectivity of the cubic $MAPbI_3$ perovskite to the part of the solar spectrum is minimum with a value of 0.08, which means that the light is absorbing or transmitting at this light frequency. Here, we bear in mind that the sum of the reflection, transmission, and absorption coefficients must be equal to 1 ($R + T + A = 1$). In the energy ranging from 4.5 to 6 eV, the reflectivity is almost constant, and after that, it starts to increase until 8.8 eV, where it finds the largest reflectivity of 0.5%. At higher energies or frequencies, the reflectivity tends to be as 20%. According to the dielectric function $\varepsilon_2^{ab}(\omega)$ displayed in the upper panel (a) of Figure 4.10, and DOS shows in the upper panel of Figure 4.7 the low energy reflectivity spectrum is strongly dominated by the Iodine and Pb atoms. In contrast, the optical transitions influence the high energy reflectivity spectrum among states of the Iodine and methylammonium molecule.

4.12 Optical absorption coefficent of cubic $MAPbI_3$

The frequency dependence of the absorption coefficient is a factor that gives valuable information about the decay of light intensity per unit distance in the perovskite. The frequency dependence of the absorption coefficient is depicted in solid-black line in the lower panel (f) on Figure 4.12, The highest peaks occurred at 10 and 13 eV, but these energies are too high from the visible region where the solar light is located. so, we focus on the part of the signal located in the energy range from 2 to 5 eV approximately The first peak is located at 4.2 eV. Remarkably, this peak is related to the reflectivity where the lowest value of reflectivity is located at 4.5 eV, so the absorption coefficient displayed on Figure 4.12f is in agreement with the reflectivity function displayed in Figure 4.12d. In the energy ranging from 5 to 8 eV, the absorption coefficient presents a small bump and at 8 eV, it starts to increase abruptly. The onset of the signal of the absorption coefficient is due to optical transitions between the I-states and the Pb-states. Above 5 eV, there are optical transitions between the methylammonium and the Pb states as the DOS reveals.

The energy loss function $L(\omega)$ is a parameter that describes the energy loss for an electron traversing the perovskite material, and that characterizes the inelastic scattering process [Sun 2016b]. The peaks in energy loss function $L(\omega)$ tells us which is the plasma frequency, these peaks are related to plasmon resonance. The increase of the light absorption is due to scattering by plasmons. An increase in the scattering leads to a delay in electromagnetic radiation in the perovskite and, consequently,

an increase in light absorption [Afanasyev 2021] by them. The inelastic scattering process is related to the drift velocity and mobility of electrons in a material as reported in literature [Ness 2005].

The lower panel (f) of Figure 4.12 display the L(ω) function in the energy ranging from 0 to 8 eV, and clearly, we can observe that there is no energy loss for photons having energy below 2 eV. Above 2 eV, the energy loss starts to increase very slowly, almost linearly until to 4 eV, then it starts to increase exponentially, reaching a maximum peak located at 4.5 eV, at this value of frequency the reflectivity get the global minimum as mentioned before, so while the loss function, depicted in solid-black line in Figure 4.12f, has a maximum peak located at 4.5 eV; the reflectivity, depicted in solid-black line in Figure 4.12, has a minimum located at 4.5 eV, so there is a common point between reflectivity and the loss of energy function. Slightly above 4.5 eV on the energy scale, it starts to decrease abruptly, and at 5 eV, it reaches a minimum local. The largest peak is located at 5.8 eV with a value almost of 0.5. Another peak with a value close to 0.5 is observed in Figure 4.12d and located at 7 eV. The first plasmon frequency is located at 4.5 eV, and the second is located plasmon frequency is 7 eV.

At higher frequency energies, the loss function tends to become smaller. Our computed loss function indicates that electrons are traversing the perovskite at an incident photon energy less than 2 eV, which is confirmed that energy loss of the material is due to the interband electronic transition [El-Nahass 2016]. We think that the energy loss spectra measurements of low energy plasmon peaks in these perovskites materials will show this second peak that we computed in this thesis. To emphasize the lost energy spectrum for perovskites was calculated from the negative imaginary part of the inverse dielectric function. We discussed all the optical properties in detail showing the path taken to achieve these results.

The Table 4.12 shows the values obtained for the perovskites of $MAPbI_3$, $MAPbBr_3$, and $MAPbCl_3$. It is worth mentioning that in the tetragonal and orthorhombic perovskites, anisotropy was presented within their optical properties, in these cases the highest values obtained for each perovskites were chosen, which were put in the table. The corresponding optics graphs can be seen in the appendix. As a quick description of the results in the table, the perovskites with iodine in their structure show what we consider, the best results compared to the rest of the other materials, the band gaps obtained for the cells with iodine show to be optimal for the optical absorption in the visible area of the electromagnetic spectrum.

For the static reflectivity, we can see that the smallest values belong to $MAPbI_3$, it must be taken into account that for a material that intends to absorb light, is important that it does not reflect it, so having low reflectivity values is considerably better, we also know that having high values for the reflectivity index are important for semiconductors with intended applications such as solar cells, again the cells with iodine show to stand out among the rest.

The values of the dielectric polarization or, (ε_1) are shown in the Table 4.12, since it indicates the polarization within the materials electrons, higher capacities can probe much more beneficial for a semiconductor, so, the values obtained for

Perovskites	Structural phase	Band gap (eV)	R(0)	n(0)	$\varepsilon_1(0)$	ε_2 (eV)
$MAPbI_3$	Cubic	1.47	0.15	2.10	4.40	2.81 (7.65)
$MAPbBr_3$	Cubic	1.95	0.97	1.90	3.61	3.50 (5.25)
$MAPbCl_3$	Cubic	2.36	0.89	1.90	3.43	3.88 (4.75)
$MAPbI_3$	Tetragonal	1.30	0.13	2.00	3.55	3.10 (7.00)
$MAPbBr_3$	Tetragonal	1.80	0.78	1.80	3.15	5.15 (4.40)
$MAPbCl_3$	Tetragonal	2.21	0.70	1.90	2.90	4.35 (4.60)
$MAPbI_3$	Orthorhombic	1.45	0.11	2.00	4.20	3.10 (6.80)
$MAPbBr_3$	Orthorhombic	1.89	0.80	1.70	3.20	5.20 (4.00)
$MAPbCl_3$	Orthorhombic	2.17	0.73	1.80	2.90	4.55 (4.45)

Table 4.4: We present the obtained values for the band gap, static reflectivity ($R(0)$), static refractive index ($n(0)$), static dielectric permittivity ($\varepsilon_1(0)$), and the maximum peak of the imaginary part of the dielectric constant (ε_2) with its respective amplitude, for $MAPbX_3$ perovskites in all their structural phases.

our perovskite show that $MAPbI_3$ presents the highest in its form cubic (4.40), followed by its orthorhombic phase (4.20) and $MAPbBr_3$ in its cubic phase (3.61). For the imaginary part of the dielectric constant (ε_2), the location, in the energetic range of 1.5 to 6.0 eV, where the peaks with the greatest amplitude (in parentheses) are presented. The peaks with the greatest optical amplitude belong to the cubic $MAPbI_3$ perovskite, located at 2.81 eV of the chosen energy range. It is observed for cubic perovskites, as the peaks of greater amplitude move to higher energy values in the energy range of choice. In the case of the tetragonal and orthorhombic phases, there is the exception of $MAPbBr_3$, where in both cases there were high amplitude peaks above 5 eV. Here in Figure 4.13 a comparison between ε_2^{ab} (upper panel) ε_1^{ab} (bottom panel) of cubic perovskites is shown. In both graphs, perovskite with iodine is represented by a purple line, bromine perovskite with a red line, and perovskite with chlorine, a green line. We can observe the shift of the beginning of absorption between perovskites, each perovskite showing the onset of its signal agreed with its bandgap, (I= 1.47 eV, Br= eV, and Cl= eV). Its maximum peak is also shifted to the right of the energy spectrum; also we can observe the amplitude difference between the maximum peaks, where the $MAPbI_3$ perovskite shows the largest amplitude.

On the bottom graph of Figure 4.13 we have the comparison of ($\varepsilon_1^{ab}(\omega)$) between our three perovskites, the panel shows us that $MAPbI_3$ presents both the highest and lowest ($\varepsilon_1^{ab}(\omega)$) value in the chosen range. Showing that $MAPbI_3$ has the highest polarization capacity in the optical range of the electromagnetic spectrum; moreover, we point out that the $MAPbI_3$ perovskite shows a sign change at 3 eV and 7 eV,

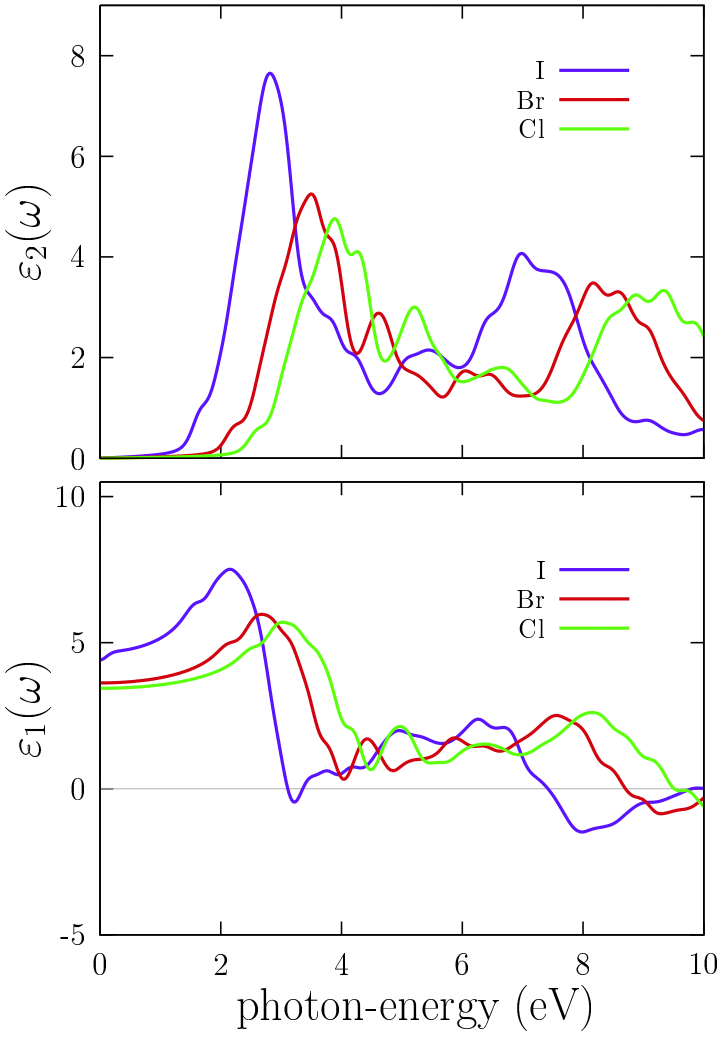

Figure 4.13: The upper panel shows the comparison of the $\mathfrak{Im}[\varepsilon^{ab}(\omega)]$ part for the three cubic perovskites of $MAPbI_3$, $MAPbBr_3$, and $MAPbCl_3$. The bottom panel shows the comparison of the $\mathfrak{Re}[\varepsilon^{ab}(\omega)]$ part for the the three mentioned cubic perovskites, in the energy range from 0 to 10 eV. Notice, the $MAPbI_3$ perovskite, shows the largest absorption peak located at 2.8 eV. Moreover, it is larger in 31% than Br perovskite.

this is not present in $MAPbBr_3$ and $MAPbCl_3$ perovskites, their signal maintains a positive output (they don't cross to a negative value) within the set range.

With a closer examination of the imaginary part of the perovskites, shown in upper panel of Figure 4.13, we observe that the maximum absorption peak in the set energy range for all our perovskites belonged to $MAPbI_3$ showing the highest amplitude in comparison to the rest of the perovskites studied; In the image, we can see that the maximum absorption peak is 31.3 % larger than for the case of perovskite with bromine and 38 % larger than for the chlorine one. Exceptionally,

the absorption peak for MAPbI3 is located in the visible region of the solar spectrum, which is between 1 to 3 eV, this is not the case for the other perovskites, that have their maximum absorption peak located far away from the visible range of the spectrum. These results separate the cubic perovskite $MAPbI_3$ from the rest. Furthermore, the best spectra belong to iodine, this being the least electronegative atom in comparison with bromide and chloride atoms. Based on this, an important conclusion on this thesis is that the larger the atom electronegativity is, the larger the shifts to higher energies in the energy scale will be, making $MAPbBr_3$ and $MAPbCl_3$ perovskites, less efficient for photovoltaic solar cells. In this thesis and based on the computed spectra, I propose this perovskite as the representative for this group of examined materials to become the light harvesting layer for a perovskite solar cell. We affirm that this perovskite will generate the largest output of electrical current once used in a photovoltaic solar cell. All calculates optical spectra for the tetragonal and orthorhombic perovskites, can be found in the appendix of this thesis.

We expect that our results presented in this thesis be of great guidance for the experimental part.

4.13 Theoretical vs experimental results

In this section of the thesis, a comparison will be made between the theoretical results obtained using the DFT-PBE method and experimental results from the literature. It is important to note that the experimental part was not dealt with in this thesis work, but this does not make it less important in any way. One of the most important objectives in theoretical studies is to support experimental research. A theoretical study can explore the areas that the experimental one cannot achieve as a guide to follow.

Perovskite	a (Å)	c (Å)	Exp. a (Å))	Exp. c (Å))
$MAPbI_3$	8.695	12.834	8.800 [Oku 2015]	12.685 [Oku 2015]
$MAPbBr_3$	5.920	——	5.933 [Oku 2015]	——
$MAPbCl_3$	5.680	——	5.666 [Oku 2015]	——

Table 4.5: Calculated structural properties of a tetragonal $MAPbI_3$, cubic $MAPbBr_3$, and cubic $MAPbCl_3$ compared with their experimental (Exp.) counterparts. The calculated structural parameters showed an error of less than $\leq 2\%$ compared to the experimental results for all perovskites shown.

Table 4.6 includes the theoretical values of the band gaps and Table 4.5 display structural parameters for the structures obtained with their experimental references. The experimental perovskites presented in the literature show a tetragonal structural phase for $MAPbI_3$, while the case for $MAPbBr_3$ and $MAPbCl_3$ is that they present

their cubic structural phase, which is in agreement with the table 2.1. For $MAPbI_3$, the resulting band gap presents a margin of 16 % of error when compared to the experimental one, for the other cases, $MAPbBr_3$ is more accurate, presenting 13 %, the opposite compared to $MAPbCl_3$, which has the highest error with 20 % to the experimental one. On the other hand, the structural parameters are almost

Perovskite	Band gap (eV)	Exp. Band gap (eV)
$MAPbI_3$	1.30	1.55 [Leguy 2016]
$MAPbBr_3$	1.95	2.24 [Leguy 2016]
$MAPbCl_3$	2.36	2.97 [Leguy 2016]

Table 4.6: Calculated bandgaps of a tetragonal $MAPbI_3$, cubic $MAPbBr_3$, and cubic $MAPbCl_3$ compared with their experimental (Exp.) counterparts. The $MAPbI_3$ calculated bandgap was approximately underestimated by 16%, in comparison with its experimental result.

identical to those reported, for the three cases, having an error in their coefficients of less than 2 %. It should be noted that DFT has a problem calculating properties such as the forbidden band, since this is a ground state theory, these properties belonging to the excited state can be obtained, but not without problems. This, of course, can be solved by improving the DFT calculation, the use of newer and more refined approximations such as the GW approximation [Mosconi 2016] can help by reducing the threshold if not completely eliminate it.

Next, the absorption coefficient calculated in this work is presented in Figure 4.14 together with an experimental one taken from the indicated reference. Similarities can be observed between the two, we can maintain a similar growth trend when increasing by the energy range, together with both having an absorption onset around 1.5 eV. Taking into account the above, we consider that the calculation of the coefficient is of good quality. Below we present a method that demonstrates how it is possible to calculate the optical properties experimentally, such as the dielectric function of a material, with which we can obtain a wide quantity of optical properties, as seen in this work.

4.13.1 Spectroscopic Ellipsometry

For the case of experimental work, there are different ways to calculate the dielectric constant of a material, one of them is called ellipsometry, which consists of the measure of a material film thickness and refractive index of individual layers and multiple layers in form of stacks. This technique has become quite popular in these years, mainly because it allows to obtain the imaginary and the real part of the dielectric function directly with a simple process [Wang 2020, Jellison 1999].

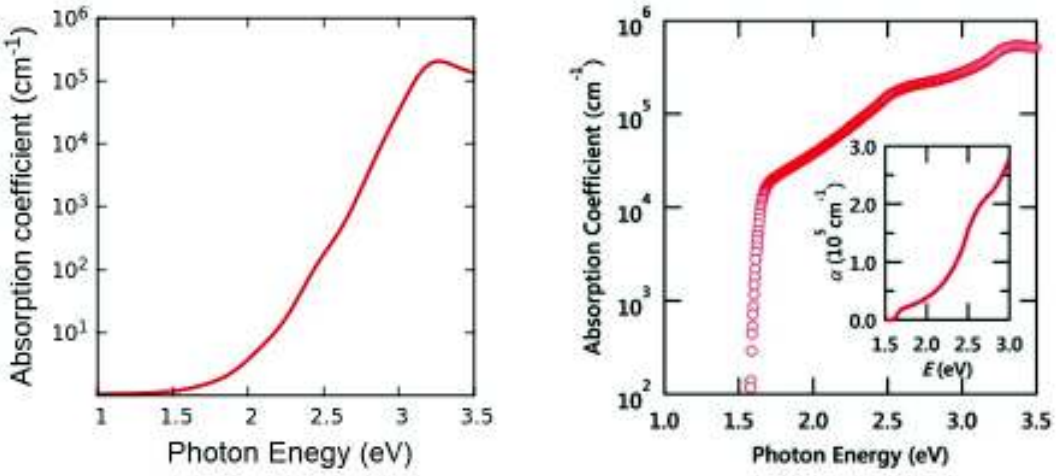

Figure 4.14: The absorption coefficient of the tetragonal perovskite $MAPbI_3$, (a) computed in this thesis, and (b) an experimental one [Kanemitsu 2017]. The onset of $\alpha(\omega)$ is in agremment with the experimental one. The computed $\alpha(\omega)$ does not present the same behavior as the experimental one, on the spectrum $\alpha(\omega)$ there is a missing shoulder, that is probably due to excitonic effects.

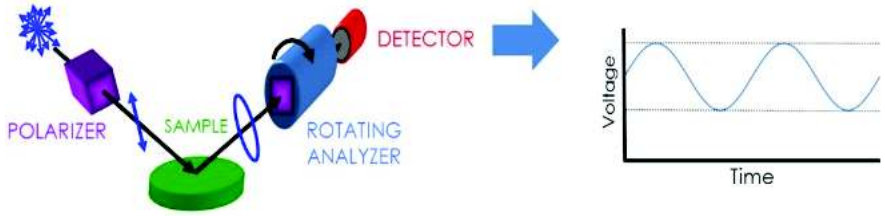

Figure 4.15: Illustration of a typical ellipsometer configuration. Image taken from Ref. [Wang 2020].

An ellipsometer consists of five main elements: a light source, a polarization state generator (PSG), a sample, a polarization state detector (PSD), and a light detector. In Figure 4.15, the configuration of this equipment is shown, where unpolarized light passes through a polarizer which polarizing the incident light beam, reflecting it off a sample surface. which is then repolarized before measuring its intensity. The process of reflecting light from a smooth sample surface generally linearly changes polarized light into elliptically polarized light. [Jellison 1999]

From these measurements, it is possible to obtain a description of the sample, the technique obtains information on the thickness and optical properties, like the complex dielectric function. Along with the latter, obtaining the optical properties studies in this work can prove quite simple.

Chapter 5

Conclusion and future prospects

Contents

5.0.1 Electronic properties 59
5.0.2 Optical properties 59
5.1 Future work 62

In this chapter, we present our conclusions and observations on the photovoltaic perovskites studied in this thesis. We studied hybrid perovskites material focusing on their optical response and electronic states. Nowadays, hybrid perovskites are one of the most studied emerging solar cell technologies. The structural, optical, and electronic properties for the proposed perovskites of $MAPbI_3$, $MAPbBr_3$ and $MAPbCl_3$ were calculated using the DFT-PBE method implemented in *Quantum ESPRESSO*. All of the following properties were obtained for the cubic (Pm-3m), tetragonal (I4/mcm) and orthorhombic (Pnam) structural phases of the three perovskites:

5.0.1 Electronic properties

- Band structure
- Total density of states (TDOS)
- Projected density of states (PDOS)

5.0.2 Optical properties

- Real part (ε_1) and imaginary part (ε_2) of the dielectric function
- Refractive index (n)
- Reflectivity (R)
- Absorption coefficient (α)
- Energy loss spectrum (L)

To achieve this, first, we chose the *Quantum ESPRESSO* software package which is essential to the learn DFT theory and provides a medium to work in. First, we took appropriate benchmarks to obtain the correct methods; then we proceeded to obtain the results covered in this work. QE was installed in *ACARUS* of the Universidad de Sonora where I became familiar with its packages and how to use them. The first benchmark that we employed to verify its accuracy in calculating the structural parameters and electronic band structure of graphene, silicon and gallium arsenide. Some of the results were presented in a seminar of my thesis. From these benchmarks, I learned that the cutoff energy for the wave function tells how many vectors of the reciprocal space will be needed to represent the wavefunctions, which means how much energy can be used for the dispersion relation of the wavefunctions plane waves.

We computed the optical and electronic properties of perovskites as follows: As the first step, we optimized the atomic structure, then with the structure in hand we computed the band structure, DOS, PDOS, and optical properties. We point out here, that the reflectivity, refraction index, and other properties were computed by scripts created with the Python programming language, to help with the calculation of all optical properties based on ε_1 and ε_2 of the dielectric constant, as well as the generation of their respective graphs using Gnuplot.

The computation of optical and electronic properties was performed within the framework of DFT as implemented in *Quantum ESPRESSO* code. Our results showed mainly that:

1. The most important perovskite for absorb solar light in the visible range is the cubic $MAPbI_3$ perovskite. The Iodine atom is the the least electronegative of the halides considered in this thesis, so the electronegativity influence the performance of the perovskite as solar collector.

2. The methylammonium affects the high energy part of the spectrum.

3. The onset of the absorption is strongly dominated by the halides and the Pb atoms.

4. The unit cell distortion depends on the relation of halide atoms (anions) and the cations that contain the unit cell. Here, electronegativity plays a minor role; in contrast, the covalent radius defines the degree of distortion.

5. The hybrid perovskites have strong light absorption in the visible range of light, between 1 and 3 eV, which implies that they are good candidates as light harvesting materials.

6. The onset of the $\mathfrak{Im}[\chi^1_{ab}(-\omega;\omega)]$ part is strongly dominated by the Pb and halide optical transference, this implies that at the Fermi level, the composition of the valence bands are due a mixture of the halogen and Pb atoms "p" states, in contrast, the low-energy conduction bands are formed mainly by Pb "p"

states. From the mentioned above, the methylammonium does not play an important role in optical absorption.

7. Remarkably, the largest Kohn-Sham band gap is correlated with the structure that has the most electronegative atom, the Chlorine atom in the unit cell.

Further, for the first time to our knowledge, here, we deduced χ within the matrix density formalism as well as the H_i Hamiltonian.

1. A complete quantum derivation of the first order optical tensor $\mathfrak{Im}[\chi^1_{ab}(-\omega;\omega)]$ was obtained employing the perturbation approach that allows us to understand how the process of light absorption happens in the perovskite material. Moreover, $\mathfrak{Im}[\chi^1_{ab}(-\omega;\omega)]$ depends on the band structure and the matrix elements of the position quantum operator computed as the $r_{mn} = \langle\psi|\hat{r}|\psi^*\rangle$. In this thesis we demonstrated that:

   - To correct the effect of the bang gap underestimation problem on the $\mathfrak{Im}[\chi^1_{ab}(-\omega;\omega)]$, we just shift the $\mathfrak{Im}[\chi^1_{ab}(-\omega;\omega)]$ to the experimental value.
   - If we employ $p_{mn} = \langle\psi|\hat{P}|\psi^*\rangle$ or $r_{mn} = \langle\psi|\hat{r}|\psi^*\rangle$ in the computation of the spectrum, this is the same. (gauge-invariance).

2. Revision of Maxwell Equations in order to derive the interaction Hamiltonian.

3. A complete derivation of the interaction Hamiltonian $H_i = \mathbf{A}\cdot\hat{p}$ that describes how the light and the material interact. The light was described classically by Maxwell Equations, whereas, the perovskite is described by Schrödinger Equation. This allows us to understand how the solar light is coupled to the perovskite solar cell.

Without a doubt, the perovskite with the halogen iodine in its structure ($MAPbI_3$) showed the best results in the group, starting with its near optimal band gap, located at 1.45 eV, a material with a starting absorption of this energy level tends to absorb the most photons from the sun radiation in the visible range, making it the most promising perovskite of all three investigated to use as a light harvesting layer for a solar cell. Absorption wise, all three phases of $MAPbI_3$ gave similar results, but the cubic perovskite showed the highest absorption in the visible range of the electromagnetic spectrum, $MAPbI_3$ perovskite in its cubic structural phase is proposed as the best material for PSC development in this perovskite group.

DFT-PBE theory used obtained good results regarding the calculation of the structural properties for all the structural phases of the three investigated perovskites, these were compared with experimental results found in the literature, and an error percentage of less than 2 % was found when compared, showing an excellent approximation for experimental data. The resulting band gaps showed an error percentage of 20 %, considering that DFT usually underestimates the gap by up to 50 %, the results were accepted as positive. This thesis, helped us to clearly

understand how to compute from first principles, the optical response of perovskite material.

5.1 Future work

- As per future work, I'd like to develop a total description employing DFT-GW (Green's function (G) and Coulomb interaction (W)) of these studied perovskites, with a focus mainly on their ability to produce electricity due to their photovoltaic capacities. GW approximation presents itself as an advancement of typical GGA approximation for DFT, providing highly accurate calculations for semiconductor material's electronic and optical properties.
- The inclusion of temperature.
- The inclusion of excitonic effects through the Bethe-Salpeter Equation.

Appendix A

Appx. Congress

A.0.1 Attendance certificate *RUIM* 2019

LA UNIVERSIDAD DE SONORA

Otorga el presente

RECONOCIMIENTO

RUIM 2019

El saber de mis hijos hará mi grandeza

A través de la
División de Ciencias Exactas y Naturales
Departamento de Investigación en Física

de la Unidad Regional Centro

A:

Edgar Paredes-Sotelo[1], José Luis Cabellos[1]

Por haber presentado el Poster:

"OPTICAL PROPERTIES OF GRAPHENE AND SILICENE MONOLAYERS" en la XXIV Reunión Universitaria de Investigación en Materiales RUIM 2019, celebrada en el Auditorio del Centro de las Artes de la Universidad de Sonora, los dias 6,7 y 8 de Noviembre de 2019.

Dr. Jorge Gaspar Armenta
Jefe del Departamento de Investigación en Física

Dr. Rafael García Gutiérrez
Presidente del Comité Organizador

Figure A.1: Attendance certificate of work presented in the: La Reunión Universitaria de Investigación en Materiales,*RUIM*, Nov. 2019, Universidad de Sonora, Hermosillo, Sonora.

A.0.2 Attendance certificate *RUIM* 2021

Figure A.2: Attendance certificate of work presented in the: La Reunión Universitaria de Investigación en Materiales,*RUIM*, March 2021, Universidad de Sonora, Hermosillo, Sonora.

Appendix B

Appx. Linear response

In this appendix we review the approach used to calculate the first order linear response ($\mathfrak{Im}[\chi(-\omega;\omega)]$). Although this is already presented in several articles [Cabellos 2009a, Cabellos 2011], for study in this thesis we derive and present the main steps in the calculation in the velocity gauge formalism of $\mathfrak{Im}[\chi(-\omega;\omega)]$.

B.0.1 Perturbation approach

We use the independent particle approximation, that allow us to describe the system using a scaled one electron density operator ρ, with which we can calculate the expectation value of an observable $\mathcal{O}$ as

$$\mathcal{O} = \mathrm{Tr}(\rho\hat{\mathcal{O}}), \tag{B.1}$$

with $\hat{\mathcal{O}}$ the associated quantum mechanical operator. The dynamical equation of ρ is given by

$$i\hbar\frac{d\rho}{dt} = [H,\rho], \tag{B.2}$$

with H as the total single electron Hamiltonian, written as

$$H(t) = H_0 + H_I(t), \tag{B.3}$$

where H_0 is the unperturbed time-independent Hamiltonian, and $H_I(t)$ is the time-dependent potential energy due to the interaction of the electron with the electromagnetic field. H_0 has eigenvalues $\hbar\omega_n(\mathbf{k})$ and eigenstates $|n\mathbf{k}\rangle$ (Bloch states) labeled by a band index n and crystal momentum $\mathbf{k}$.

To proceed with the solution of Eq. (B.2) it is convenient to use the interaction picture, where one uses a unitary operator $U = \exp(iH_0t/\hbar)$ to transform any operator $\hat{\mathcal{O}}$ into $\tilde{\mathcal{O}} = U\hat{\mathcal{O}}U^\dagger$, where even if $\hat{\mathcal{O}}$ does not depend on t, $\tilde{\mathcal{O}}$ does depend through the explicit dependence of U. Then Eq. (B.2) leads to

$$i\hbar\frac{d\tilde{\rho}}{dt} = [\tilde{H}_i,\tilde{\rho}], \tag{B.4}$$

with solution

$$i\hbar\tilde{\rho}(t) = i\hbar\tilde{\rho}_0 + \int_{-\infty}^{t} dt'[\tilde{H}_I(t'),\tilde{\rho}(t')], \tag{B.5}$$

where $\tilde{\rho}_0 = \tilde{\rho}(t=-\infty)$ is the unperturbed density matrix. We look for the standard perturbation series solution,

$$\tilde{\rho}(t) = \tilde{\rho}^{(0)} + \tilde{\rho}^{(1)} + \tilde{\rho}^{(2)} + \cdots, \tag{B.6}$$

where the superscript denotes the order (power) with which each term depends on the perturbation H_I. Then, Eq. (B.5) gives that the N-th order term is given by

$$\tilde{\rho}^{(N)}(t) = \frac{1}{i\hbar}\int_{-\infty}^{t} dt'[\tilde{H}_I(t'), \tilde{\rho}^{(N-1)}(t')]. \tag{B.7}$$

The series is generated by the unperturbed density operator $\tilde{\rho}^{(0)} \equiv \tilde{\rho}_0$, assumed to be the diagonal Fermi-Dirac distribution, $\langle n\mathbf{k}|\tilde{\rho}_0|n\mathbf{k}\rangle = f(\hbar\omega_n(\mathbf{k})) \equiv f_n$. For a clean, cold ($T = 0$K) semiconductor $f_n = 1$ for n a valence (v) or occupied band and zero for n a conduction (c) or empty band.

We first look for the expectation value of the macroscopic current density, $\mathbf{J}$, through

$$\mathbf{J} = e\mathrm{Tr}(\rho\dot{\mathbf{r}}) = e\mathrm{Tr}(\tilde{\rho}\dot{\tilde{\mathbf{r}}}), \tag{B.8}$$

where $\dot{\mathbf{r}}$ is the time derivative of the position operator of the electron of charge e, given by

$$\mathbf{v} \equiv \dot{\mathbf{r}} = \frac{1}{i\hbar}[\mathbf{r}, H], \tag{B.9}$$

with $\mathbf{v}$ the velocity operator of the electron. Then, we calculate the macroscopic polarization density $\mathbf{P}$ related to $\mathbf{J}$ by $d\mathbf{P}/dt = \mathbf{J}$, and for a harmonic perturbing electromagnetic field, we write the second order non-linear polarization for as,

$$P^{a(2)}(2\omega) = \chi^{abc}(-2\omega;\omega,\omega)E^b(\omega)E^c(\omega), \tag{B.10}$$

where χ^{abc} is the second harmonic non-linear susceptibility responsible of second harmonic generation (SHG). The roman superscripts in Eq. (B.10) denote Cartesian directions and if repeated they have to be summed upon, and we see that χ^{abc} must satisfy the intrinsic permutation symmetry, $\chi^{abc} = \chi^{acb}$.

B.0.2 Scissors Hamiltonian

As it is well known, LDA underestimates the band gap. A procedure to fix this is to use the so called scissors correction by which one could only shift the conduction bands in energy, so that the band gap corresponds to the accepted experimental, or GW band gap.[Hybertsen 1986, Cabellos 2009a, Cabellos 2011] Concurrently, one uses the LDA wave functions since they produce band structures with dispersion relations similar to those predicted by the GW approximation. Then, the scissors term $\hat{S}$,

$$\hat{S} = \hbar\Delta\sum_n \int d^3k(1 - f_n)|n\mathbf{k}\rangle\langle n\mathbf{k}|, \tag{B.11}$$

where $\hbar\Delta$ is the rigid ($\mathbf{k}$-independent) energy correction to be applied. The scissored Hamiltonian is

$$H_0^S \quad = \quad H_0 + S(\mathbf{r}, \mathbf{p}), \tag{B.12}$$

where $S(\mathbf{r},\mathbf{p})$ is the coordinate representation of $\hat{S}$, and H_0 is the unscissored or LDA Hamiltonian,

$$H_0 = \frac{p^2}{2m} + V(\mathbf{r}), \tag{B.13}$$

with m the mass of the electron, $\mathbf{p}$ its canonical momentum given by $-i\hbar\boldsymbol{\nabla}$, and $V(\mathbf{r})$ the periodic crystal potential. These Hamiltonians satisfy

$$H_0\psi_{n\mathbf{k}}(\mathbf{r}) = \hbar\omega_{n\mathbf{k}}\psi_{n\mathbf{k}}(\mathbf{r}), \tag{B.14}$$
$$H_0^S\psi_{n\mathbf{k}}(\mathbf{r}) = \hbar\omega^S_{n\mathbf{k}}\psi_{n\mathbf{k}}(\mathbf{r}), \tag{B.15}$$

with

$$\omega^S_{n\mathbf{k}} = \omega_{n\mathbf{k}} + (1-f_n)\Delta, \tag{B.16}$$

and $\psi_{n\mathbf{k}}(\mathbf{r}) = \langle\mathbf{r}|n\mathbf{k}\rangle$ is the coordinate representation of the ket $|n\mathbf{k}\rangle$. As stated above, the scissored Hamiltonian has the same wave functions as the unscissored one.

B.1 Velocity-gauge Formalism

To calculate the optical response through the colloquially called "velocity-gauge", we use the minimal substitution through which the in the presence of an electromagnetic field the Hamiltonian is written as

$$H^S = \frac{1}{2m}(\mathbf{p} - \frac{e}{c}\mathbf{A})^2 + V(\mathbf{r}) + S(\mathbf{r}, \mathbf{p} - \frac{e}{c}\mathbf{A}), \tag{B.17}$$

$\mathbf{A}$ is the vector potential, through which one calculates the magnetic field $\mathbf{B} = \nabla\times\mathbf{A}$ and the electric field $\mathbf{E} = -(1/c)\dot{\mathbf{A}}$. We assume the long wavelength approximation by which $\mathbf{A}$ is spatially constant and thus only depends on time. Furthermore we use a harmonic perturbation such that $\mathbf{A}(t) = \mathbf{A}(\omega)e^{-i\tilde{\omega}t}$, where $\tilde{\omega} = \omega + i\eta$, and $\eta > 0$ is used to turn on the interaction, adiabatically. We can expand the scissors operator according to,[Nastos 2005]

$$S(\mathbf{r},\mathbf{p}-\frac{e}{c}\mathbf{A}) = S(\mathbf{r},\mathbf{p}) + \frac{e}{c}\frac{i}{\hbar}\mathbf{A}\cdot[\mathbf{r}, S(\mathbf{r},\mathbf{p})] + \frac{1}{2!}\left(\frac{e}{c}\frac{i}{\hbar}\right)^2[\mathbf{A}\cdot\mathbf{r},[\mathbf{A}\cdot\mathbf{r}, S(\mathbf{r},\mathbf{p})]] + \cdots, \tag{B.18}$$

then the scissored Hamiltonian up to second order in $\mathbf{A}$ is

$$H^S = H_0^S + H_{I,1} + H_{I,2}, \tag{B.19}$$

where

$$H_{I,1} = -\frac{e}{c}\mathbf{A}\cdot\mathbf{v}^S, \tag{B.20}$$
$$H_{I,2} = -\frac{ie^2}{2\hbar c^2}[r^b, v^{NL,c}]A^bA^c + \frac{e^2}{2mc^2}A^2, \tag{B.21}$$

are the linear and non-linear (second order) interaction Hamiltonians. We have defined

$$\mathbf{v}^{NL} = -\frac{i}{\hbar}[\mathbf{r}, S(\mathbf{r},\mathbf{p})], \tag{B.22}$$

as the non-local contribution to the velocity operator due to the scissors term, and

$$\mathbf{v}^{S} = \frac{\mathbf{p}}{m} + \mathbf{v}^{NL}, \tag{B.23}$$

as the scissored velocity operator. From Eq. (B.9), we get that

$$\begin{aligned} \dot{r}^a &= -\frac{i}{\hbar}[r^a, H^S] \\ &= v^{S,a} - \frac{e}{mc}A^a + \frac{ie}{\hbar c}[r^a, v^{NL,b}]A^b - \frac{e^2}{2\hbar^2 c^2}[r^a,[r^b, v^{NL,c}]]A^bA^c, \end{aligned} \tag{B.24}$$

thus the current operator, $\mathbf{j} = e\dot{\mathbf{r}}$, up to second order in $\mathbf{A}$ is

$$j^a = j_0^a + j_1^a + j_2^a, \tag{B.25}$$

From Eq. (B.8),

$$J^{(1)a} = \mathrm{Tr}(j_0^a \rho^{(1)}) + \mathrm{Tr}(j_1^a \rho^{(0)}), \tag{B.26}$$

is the linear macroscopic current.

B.1.1 Linear Response

We derive the linear response as part of this thesis, we also derive some results that will be used for the Edgar's Doctoral project, any way. Taking matrix elements of Eq. (B.7) and using Eq. (B.20) we have

$$\tilde{\rho}^{(1)}_{mn}(t) = \frac{ei}{\hbar c}\int_{-\infty}^{t} dt' A^b(t') \sum_{\ell} \left(\tilde{v}^{S,b}_{m\ell}(t')\tilde{\rho}^{(0)}_{\ell n}(t') - \tilde{\rho}^{(0)}_{m\ell}(t')\tilde{v}^{S,b}_{\ell n}(t') \right), \tag{B.27}$$

where the sum over ℓ is over all states, and we have omitted $\mathbf{k}$ from the already crowded notation. Since $U(t) = \exp(iH_0^S t/\hbar)$, we get

$$\tilde{v}^{S,b}_{m\ell}(t') = \langle m\mathbf{k}|U(t')v^{S,b}U(t')^\dagger|\ell\mathbf{k}\rangle = e^{i\omega^S_{m\ell}t'}v^{S,b}_{m\ell}, \tag{B.28}$$

and $\tilde{\rho}^0_{\ell n}(t') = f_\ell \Delta_{\ell n}$, then

$$\begin{aligned} \tilde{\rho}^{(1)}_{mn}(t) &= = \frac{ei}{\hbar c} f_{nm} v^{S,b}_{mn} A^b_0 \int_{-\infty}^{t} dt' e^{i(\omega^S_{mn}-\omega)t'} \\ &= \frac{e}{\hbar c}\frac{v^{S,b}_{mn} f_{nm}}{\omega^S_{mn} - \omega} A^b(t) e^{i\omega^S_{mn}t}, \end{aligned} \tag{B.29}$$

from where, we get

$$\rho^{(1)}_{mn}(t) = \frac{e}{\hbar c}\frac{f_{nm} v^{S,b}_{mn}}{\omega^S_{mn} - \omega} A^b(t). \tag{B.30}$$

From Eq. (B.26) (using the cyclic invariance of the trace),

$$\begin{aligned} J^{(1)a}(t) &= e\mathrm{Tr}\left(v^{S,a}\rho^{(1)}\right) + e\mathrm{Tr}\left(\rho^{(0)}\left(-\frac{e}{mc}A^a + \frac{ie}{\hbar c}A^b[r^a, v^{NL,b}]\right)\right) \\ &= e\int\frac{d^3k}{8\pi^3}\sum_{mn} v^{S,a}_{nm}\rho^{(1)}_{mn} - \frac{e^2n}{mc}A^a + \frac{ie^2}{\hbar c}A^b\mathrm{Tr}(\rho^{(0)}[r^a, v^{NL,b}]) \\ &= \Big(\frac{-ie^2}{\hbar\omega}\int\frac{d^3k}{8\pi^3}\sum_{mn}\frac{v^{S,a}_{nm}v^{S,b}_{mn}f_{nm}}{\omega^S_{mn}-\omega} + \frac{ie^2n}{m\omega}\delta_{ab} + \frac{e^2}{\hbar\omega}\mathrm{Tr}(\rho^{(0)}\mathcal{F}^{ab})\Big)E^b(\omega), \end{aligned} \tag{B.31}$$

we have defined

$$\mathcal{F}^{ab} = [r^a, v^{NL,b}], \tag{B.32}$$

and we used $\mathbf{A}(t) = -i(c/\omega)\mathbf{E}(t)$ and $\mathrm{Tr}(\rho^{(0)}) = n$ with n the electronic density. We use $d\mathbf{P}/dt = \mathbf{J}$ to write $P^a(\omega) = (i/\omega)J^a(\omega) = \chi^{ab}(-\omega;\omega)E^b(\omega)$, where

$$\begin{aligned} \chi^{ab}(-\omega;\omega) &= \frac{e^2}{\hbar\omega^2}\int\frac{d^3k}{8\pi^3}\sum_{mn}\frac{v^{S,a}_{nm}v^{S,b}_{mn}f_{nm}}{\omega^S_{mn}-\omega} - \frac{e^2n}{m\omega^2}\delta_{ab} + \frac{ie^2}{\hbar\omega^2}\mathrm{Tr}(\rho^{(0)}\mathcal{F}^{ab}) \\ &= \frac{e^2}{\hbar}\int\frac{d^3k}{8\pi^3}\sum_{mn} f_{nm}v^{S,a}_{nm}v^{S,b}_{mn}\Big(\frac{1}{(\omega^S_{mn})^2(\omega^S_{mn}-\omega)} + \frac{1}{(\omega^S_{mn})^2\omega} + \frac{1}{\omega^S_{mn}\omega^2}\Big) \\ &- \frac{e^2n}{m\omega^2}\delta_{ab} + \frac{ie^2}{\hbar\omega^2}\mathrm{Tr}(\rho^{(0)}\mathcal{F}^{ab}), \end{aligned} \tag{B.33}$$

is the linear susceptibility within the scissored Hamiltonian. Using time reversal symmetry $v^S_{mn}(-\mathbf{k}) = -v^S_{nm}(\mathbf{k})$ and $\omega^S_{mn}(-\mathbf{k}) = \omega^S_{mn}(\mathbf{k})$, we can easily show that the contribution to $\mathbf{J}^{(1)}$ coming from the second term in the right hand side (rhs) of Eq. (B.33) cancels. By simple subindex manipulation, the third term, combined with the fourth term in the rhs of Eq. (B.33), gives

$$\frac{1}{\omega^2}\Big(\frac{e^2}{\hbar}\int\frac{d^3k}{8\pi^3}\sum_{vc}\frac{v^{S,a}_{vc}v^{S,b}_{cv} + v^{S,a}_{cv}v^{S,b}_{vc}}{\omega^S_{cv}} - \frac{e^2n}{m}\delta_{ab}\Big) \equiv \frac{\zeta^{ab}}{\omega^2}. \tag{B.34}$$

The last term in the rhs of Eq. (B.33) reduces to

$$\begin{aligned} \frac{ie^2}{\hbar\omega^2}\mathrm{Tr}(\rho^{(0)}\mathcal{F}^{ab}) &= \frac{ie^2}{\hbar\omega^2}\int\frac{d^3k}{8\pi^3}\sum_{mn}\rho^{(0)}_{mn}\mathcal{F}^{ab}_{nm} \\ &= \frac{ie^2}{\hbar\omega^2}\int\frac{d^3k}{8\pi^3}\sum_{n} f_n\mathcal{F}^{ab}_{nn} \\ &= \frac{-e^2\Delta}{\hbar\omega^2}\int\frac{d^3k}{8\pi^3}\sum_{vc}(r^a_{vc}r^b_{cv} + r^b_{vc}r^a_{cv}) \equiv \frac{\eta^{ab}}{\omega^2}, \end{aligned} \tag{B.35}$$

where

$$\mathcal{F}^{ab}_{nn} = i\Delta\sum_{\ell\neq n} f_{n\ell}(r^a_{n\ell}r^b_{\ell n} + r^b_{n\ell}r^a_{\ell n}). \tag{B.36}$$

We can show in general that,

$$\mathcal{F}^{bc}_{nm}(\mathbf{k}) = \mathcal{F}^{bc}_{i,nm}(\mathbf{k}) + \mathcal{F}^{bc}_{e,nm}(\mathbf{k}), \tag{B.37}$$

with

$$\mathcal{F}^{bc}_{e,nm}(\mathbf{k}) = [r^b_e, v^{NL,c}]_{nm} = i\Delta\Big(\sum_{p\neq m} f_{np} r^c_{np}(\mathbf{k}) r^b_{pm}(\mathbf{k}) - \sum_{p\neq n} f_{pm} r^b_{np}(\mathbf{k}) r^c_{pm}(\mathbf{k})\Big), \tag{B.38}$$

and

$$\mathcal{F}^{bc}_{i,nm}(\mathbf{k}) = [r^b_i, v^{NL,c}]_{nm} = \Delta f_{nm} r^c_{nm;b}(\mathbf{k}). \tag{B.39}$$

This is done by decomposing $\mathbf{r}$ into its *interband* part $\mathbf{r}_e$ and intraband part $\mathbf{r}_i$; using the following property of $\mathbf{r}_i$,

$$\langle n\mathbf{k}|[\mathbf{r}_i, \mathcal{O}]|m\mathbf{k}'\rangle = i\delta(\mathbf{k}-\mathbf{k}')(\mathcal{O}_{nm})_{;\mathbf{k}}, \tag{B.40}$$

where $\mathcal{O}$ is an operator and $(\mathcal{O}_{nm})_{;\mathbf{k}}$ the generalized derivative of its matrix elements, and the matrix elements of $\mathbf{r}_e$ simply calculated through

$$(\mathbf{r}_e)_{nm} \to \mathbf{r}_{nm} = \frac{\mathbf{p}_{nm}}{im\omega_{nm}} \quad n \neq m. \tag{B.41}$$

The generalized derivative $r^b_{nm;k^a}$ is explicitly given by,

$$r^b_{nm;k^a} = \frac{r^a_{nm}\Delta^b_{mn} + r^b_{nm}\Delta^a_{mn}}{\omega_{nm}} + \frac{i}{\omega_{nm}}\sum_{\ell}\big(\omega_{\ell m} r^a_{n\ell} r^b_{\ell m} - \omega_{n\ell} r^b_{n\ell} r^a_{\ell m}\big), \tag{B.42}$$

where $\Delta^a_{nm} = (p^a_{nn} - p^a_{mm})/m$ is the difference between the electron velocity at bands n and m. Considering that both the non-diagonal matrix elements of $\mathbf{r}$, $\mathbf{r}_{nm}$, and its generalized derivative, $\mathbf{r}_{nm;\mathbf{k}}$, are evaluated using the unscissored energies, and the canonical momentum matrix elements given by

$$\mathbf{p}_{nm} = \langle n\mathbf{k}|\mathbf{p}|m\mathbf{k}\rangle = \int d^3r \psi_{n\mathbf{k}}(\mathbf{r})(-i\hbar\boldsymbol{\nabla})\psi_{m\mathbf{k}}(\mathbf{r}). \tag{B.43}$$

Finally, Eq. (B.33) reduces to

$$\chi^{ab}(-\omega;\omega) \;=\; \frac{e^2}{\hbar}\int\frac{d^3k}{8\pi^3}\sum_{mn}\frac{v^{S,a}_{nm}v^{S,b}_{mn}f_{nm}}{(\omega^S_{mn})^2(\omega^S_{mn}-\omega)} + \frac{\zeta^{ab}}{\omega^2} + \frac{\eta^{ab}}{\omega^2}. \tag{B.44}$$

We can use

$$\mathbf{v}^S_{nm} = \mathbf{v}_{nm}\frac{\omega^S_{nm}}{\omega_{nm}}, \tag{B.45}$$

where $\mathbf{v}_{nm} = \mathbf{p}_{nm}/m$, then Eq. (B.34) reduces to ($\omega^S_{cv} = \omega_{cv} + \delta$)

$$\begin{aligned}
\zeta^{ab} &= \frac{e^2}{\hbar}\int\frac{d^3k}{8\pi^3}\sum_{vc}\omega^S_{cv}\frac{v^a_{vc}v^b_{cv} + v^a_{cv}v^b_{vc}}{\omega^2_{cv}} - \frac{e^2 n}{m}\delta_{ab} \\
&= -e^2\int\frac{d^3k}{8\pi^3}\sum_v f_v\Big(\frac{\delta_{ab}}{m} - \sum_c\frac{v^a_{vc}v^b_{cv} + v^a_{cv}v^b_{vc}}{\hbar\omega_{cv}}\Big) + \frac{e^2\Delta}{\hbar}\int\frac{d^3k}{8\pi^3}\sum_{vc}\frac{v^a_{vc}v^b_{cv} + v^a_{cv}v^b_{vc}}{\omega^2_{cv}}. \\
&= -e^2\int\frac{d^3k}{8\pi^3}\sum_v f_v\left[\frac{1}{m^*_v}\right]^{ab} + \frac{e^2\Delta}{\hbar}\int\frac{d^3k}{8\pi^3}\sum_{vc}\big(r^a_{vc}r^b_{cv} + r^a_{cv}r^b_{vc}\big),
\end{aligned} \tag{B.46}$$

where $[1/m_v^*]^{ab}$ is the effective mass tensor. The second term in the rhs of Eq. (B.46) is $-\eta^{ab}$, then above equation leads to

$$\zeta^{ab} + \eta^{ab} = -e^2 \int \frac{d^3k}{8\pi^3} \sum_v f_v \left[\frac{1}{m_v^*(\mathbf{k})}\right]^{ab}, \tag{B.47}$$

with which we obtain the following result for the linear susceptibility

$$\chi^{ab}(-\omega;\omega) = \frac{e^2}{\hbar} \int \frac{d^3k}{8\pi^3} \sum_{mn} \frac{v^a_{nm} v^b_{mn} f_{nm}}{\omega^2_{mn}(\omega^S_{mn} - \omega)} - \frac{e^2}{\omega^2} \int \frac{d^3k}{8\pi^3} \sum_v f_v \left[\frac{1}{m_v^*(\mathbf{k})}\right]^{ab} \tag{B.48}$$

For a clean, cold semiconductor the integration over the Brillouin Zone of the term involving the effective mass tensor vanishes identically, which implies

$$\mathrm{Im}[\chi^{ab}(-\omega;\omega)] = \frac{\pi e^2}{\hbar} \int \frac{d\mathbf{k}}{8\pi^3} \sum_{cv} \mathrm{Re}\{r^a_{vc}(\mathbf{k}) r^b_{cv}(\mathbf{k})\} \delta(\omega^S_{cv}(\mathbf{k}) - \omega), \tag{B.49}$$

Our result show, that simply states that for the linear response, the scissors correction only shifts rigidly the energy position of the LDA spectrum by Δ. This Equation B.50 is important in this thesis, and with it we computed the imaginary part of the linear optical response.

$$\mathrm{Im}[\chi^{ab}(-\omega;\omega)] = \frac{\pi e^2}{\hbar} \int \frac{d\mathbf{k}}{8\pi^3} \sum_{cv} \mathrm{Re}\{r^a_{vc}(\mathbf{k}) r^b_{cv}(\mathbf{k})\} \delta(\omega^S_{cv}(\mathbf{k}) - \omega), \tag{B.50}$$

Bibliography

[Adair 1989] Robert Adair, L. L. Chase and Stephen A. Payne. *Nonlinear refractive index of optical crystals.* Phys. Rev. B, vol. 39, pages 3337–3350, Feb 1989. 24

[Adler 1962] Stephen L. Adler. *Quantum Theory of the Dielectric Constant in Real Solids.* Phys. Rev., vol. 126, pages 413–420, Apr 1962. 45

[Afanasyev 2021] Dmitriy Afanasyev, Niyazbek Ibrayev and Nurxat Nuraje. *Effect of Plasmonic Nanostructures on the Optical Properties of CH3NH3PbI Perovskite Films.* Frontiers in Materials, vol. 7, page 492, 2021. 53

[Ahmed 2014] Towfiq Ahmed, C. La o vorakiat, T. Salim, Y. M. Lam, Elbert E. M. Chia and Jian-Xin Zhu. *Optical properties of organometallic perovskite: An ab initio study using relativistic GW correction and Bethe-Salpeter equation.* EPL (Europhysics Letters), vol. 108, no. 6, page 67015, dec 2014. 36

[Akkus 2007] Harun Akkus and Amirullah M Mamedov. *Ab initiocalculations of the electronic structure and linear optical properties, including self-energy effects, for paraelectric SbSI.* Journal of Physics: Condensed Matter, vol. 19, no. 11, page 116207, mar 2007. 25

[Aleman-Nava 2014] Gibran S. Aleman-Nava, Victor H. Casiano-Flores, Diana L. Cardenas-Chavez, Rocio Daaz-Chavez, Nicolae Scarlat, Jurgen Mahlknecht, Jean-Francois Dallemand and Roberto Parra. *Renewable energy research progress in Mexico: A review.* Renewable and Sustainable Energy Reviews, vol. 32, pages 140–153, 2014. 1

[Anderson 2015] Sean M. Anderson, Nicolas Tancogne-Dejean, Bernardo S. Mendoza and Valérie Véniard. *Theory of surface second-harmonic generation for semiconductors including effects of nonlocal operators.* Phys. Rev. B, vol. 91, page 075302, Feb 2015. 21, 45

[Argaman 2000] Nathan Argaman and Guy Makov. *Density functional theory: An introduction.* American Journal of Physics, vol. 68, no. 1, pages 69–79, 2000. 13

[Ashcroft 1976] W. Ashcroft, N.W. Ashcroft, N.D. Mermin, N.D. Mermin and Brooks/Cole Publishing Company. Solid state physics. HRW international editions. Holt, Rinehart and Winston, 1976. 16, 21

[Askeland 2010] Donald R. Askeland and Pradeep P. Fulay. The Science & Engineering of Materials. Cengage Learning, sixth edition édition, 2010. 21

[Aversa 1995] Claudio Aversa and J. E. Sipe. *Nonlinear optical susceptibilities of semiconductors: Results with a length-gauge analysis.* Phys. Rev. B, vol. 52, pages 14636–14645, Nov 1995. 16

[Bachelet 1982] Giovanni Bachelet. *Relativistic norm-conserving pseudopotentials.* Physical Review B, vol. 25, no. 4, 1982. 15

[Barca 2020] Giuseppe M.J. Barca, Colleen Bertoni, Laura Carrington, Dipayan Datta, Nuwan De Silva, J. Emiliano Deustua, Dmitri G. Fedorov, Jeffrey R. Gour, Anastasia O. Gunina, Emilie Guidez, Taylor Harville, Stephan Irle, Joe Ivanic, Karol Kowalski, Sarom S. Leang, Hui Li, Wei Li, Jesse J. Lutz, Ilias Magoulas, Joani Mato, Vladimir Mironov, Hiroya Nakata, Buu Q. Pham, Piotr Piecuch, David Poole, Spencer R. Pruitt, Alistair P. Rendell, Luke B. Roskop, Klaus Ruedenberg, Tosaporn Sattasathuchana, Michael W. Schmidt, Jun Shen, Lyudmila Slipchenko, Masha Sosonkina, Vaibhav Sundriyal, Ananta Tiwari, Jorge L. Galvez Vallejo, Bryce Westheimer, Marta Włoch, Peng Xu, Federico Zahariev and Mark S. Gordon. *Recent developments in the general atomic and molecular electronic structure system.* Journal of Chemical Physics, vol. 152, no. 15, 2020. 14

[Becke 2014a] Axel Becke. *Perspective: Fifty years of density-functional theory in chemical physics.* The Journal of chemical physics, vol. 140, page 18A301, 05 2014. 11

[Becke 2014b] Axel D. Becke. *Perspective: Fifty years of density-functional theory in chemical physics.* Journal of Chemical Physics, vol. 140, no. 18, may 2014. 3

[Beiser 1987] A. Beiser. Concepts of modern physics. McGraw-Hill International Student Editions. McGraw-Hill, 1987. 15

[Benmir 2013] A. Benmir and M.S. Aida. *Analytical Modeling and Simulation of CIGS Solar Cells.* Energy Procedia, vol. 36, pages 618–627, 2013. TerraGreen 13 International Conference 2013 - Advancements in Renewable Energy and Clean Environment. 1

[Bennink 1999] Ryan S. Bennink, Young-Kwon Yoon, Robert W. Boyd and J. E. Sipe. *Accessing the optical nonlinearity of metals with metal dielectric photonic bandgap structures.* Opt. Lett., vol. 24, no. 20, pages 1416–1418, Oct 1999. 22

[Berestetskii 2012] V.B. Berestetskii, L.P. Pitaevskii and E.M. Lifshitz. Quantum electrodynamics: Volume 4. Numeéro v. 4. Elsevier Science, 2012. 17

[Boyd 2013] R.W. Boyd. Nonlinear optics. Elsevier Science, 2013. 16

[Burke 2012] Kieron Burke. *Perspective on density functional theory.* Journal of Chemical Physics, vol. 136, no. 15, apr 2012. 12

[Burschka 2013] Julian Burschka, Norman Pellet, Soo-Jin Moon, Robin Humphry-Baker, Peng Gao, Mohammad K. Nazeeruddin and Michael Grätzel. *Sequential deposition as a route to high-performance perovskite-sensitized solar cells.* Nature, vol. 499, no. 7458, pages 316–319, Jul 2013. 34

[Cabellos 2009a] J. L. Cabellos, Bernardo S. Mendoza, M. A. Escobar, F. Nastos and J. E. Sipe. *Effects of nonlocality on second-harmonic generation in bulk semiconductors.* Phys. Rev. B, vol. 80, page 155205, Oct 2009. 5, 12, 21, 22, 45, 46, 65, 66

[Cabellos 2009b] J. L. Cabellos, Cuauhtémoc Salazar and Bernardo S. Mendoza. *Stress-modulated optical spin injection in bulk Si and GaAs semiconductors.* Phys. Rev. B, vol. 80, page 245204, Dec 2009. 5

[Cabellos 2011] J. L. Cabellos, Bernardo S. Mendoza and A. I. Shkrebtii. *Optical coherent current control at surfaces: Theory of injection current.* Phys. Rev. B, vol. 84, page 195326, Nov 2011. 5, 65, 66

[Cai 2017] Molang Cai, Yongzhen Wu, Han Chen, Xudong Yang, Yinghuai Qiang and Liyuan Han. *Cost-Performance Analysis of Perovskite Solar Modules.* Advanced Science, pages 1–6, 2017. 2

[Cargnoni 2000] Fausto Cargnoni, Carlo Gatti, Emanuela May and Dario Narducci. *Geometrical reconstructions and electronic relaxations of silicon surfaces. I. An electron density topological study of H-covered and clean Si(111)(1×1) surfaces.* The Journal of Chemical Physics, vol. 112, no. 2, pages 887–899, 2000. iii, 22

[Castillo-Quevedo 2020] Cesar Castillo-Quevedo, Jose Luis Cabellos, Raul Aceves, Roberto Nuez-Gonzalez and Alvaro Posada-Amarillas. *Cu-Doped KCl Unfolded Band Structure and Optical Properties Studied by DFT Calculations.* Materials, vol. 13, no. 19, 2020. 12, 21, 34

[Che 2008] Renchao Che, Ruijuan Xiao, Chongyun Liang, Huaixin Yang, Chao Ma, Honglong Shi and Jianqi Li. *Electron energy-loss spectroscopy andab initioelectronic structure of the LaOFeP superconductor.* Physical Review B, vol. 77, no. 18, May 2008. 25

[Chimata 2010] Raghuveer Chimata. *Optical Properties of Materials Calculated from First Principles Theory.* PhD thesis, Uppsala University, 2010. 23

[Clark 2005] Stewart J. Clark, Matthew D. Segall, Chris J. Pickard, Phil J. Hasnip, Matt I.J. Probert, Keith Refson and Mike C. Payne. *First principles methods using CASTEP.* Zeitschrift fur Kristallographie, vol. 220, no. 5-6, pages 567–570, 2005. 14

[Denteneer 1987] P.J.H. Denteneer. *The pseudopotential-density-functional method applied to semiconducting crystals*. PhD thesis, Technische Universiteit Eindhoven, 1987. 14

[Diana Marcela Montoya Montoya 2016] Diana Marcela Montoya Montoya. *Películas Orgánico-Inorgánicas con Estructura Perovskita como Capa Activa en Dispositivos Fotovoltaicos*. PhD thesis, Centro de Investigaciones en Optica A.C., Guanajuato, 2016. 8

[Diau 2017] Eric Diau and Peter Chen. Perovskite Solar Cells: Principle, Materials and Devices. World Scientific Publishing, Singapore, volume 1 édition, 2017. 4

[Dominikowska 2016] Justyna Dominikowska, Miroslaw Jablonski and Marcin Palusiak. *Feynman force components, basis for a solution to the covalent vs. ionic dilemma*. Phys. Chem. Chem. Phys., vol. 18, pages 25022–25026, 2016. 28

[Ehrenreich 1959] H. Ehrenreich and M. H. Cohen. *Self-Consistent Field Approach to the Many-Electron Problem*. Phys. Rev., vol. 115, pages 786–790, Aug 1959. 45

[El-Nahass 2016] M. M. El-Nahass, H. S. Soliman and A. El-Denglawey. *Absorption edge shift, optical conductivity, and energy loss function of nanoÂ thermal-evaporated N-type anatase TiO2 films*. Applied Physics A, vol. 122, no. 8, page 775, Jul 2016. 53

[Eljarrat 2016] A. Eljarrat, L. López-Conesa, S. Estradé and F. Peiró. *Electron energy loss spectroscopy on semiconductor heterostructures for optoelectronics and photonics applications*. Journal of Microscopy, vol. 262, no. 2, pages 142–150, 2016. 25

[Ellabban 2014] Omar Ellabban, Haitham Abu-Rub and Frede Blaabjerg. *Renewable energy resources: Current status, future prospects and their enabling technology*. Renewable and Sustainable Energy Reviews, vol. 39, pages 748–764, 2014. 1

[Eperon 2014] Giles E. Eperon, Samuel D. Stranks, Christopher Menelaou, Michael B. Johnston, Laura M. Herz and Henry J. Snaith. *Formamidinium lead trihalide: A broadly tunable perovskite for efficient planar heterojunction solar cells*. Energy and Environmental Science, 2014. 8

[Eswaramoorthy 2020] Nandhakumar Eswaramoorthy and Kamatchi R. Fabrication and manufacturing process of perovskite solar cell, chapitre 3, pages 67–101. John Wiley and Sons, Ltd, 2020. 34

[Fan 2010] Qi Hua Fan, Changyong Chen, Xianbo Liao, Xianbi Xiang, Shibin Zhang, W. Ingler, Nirupama Adiga, Zhihua Hu, Xinmin Cao, Wenhui Du and Xunming Deng. *High efficiency silicon-germanium thin film solar cells*

using graded absorber layer. Solar Energy Materials and Solar Cells, vol. 94, no. 7, pages 1300–1302, 2010. 1

[Feng 2014] Jing Feng. *Mechanical properties of hybrid organic-inorganic CH3NH3BX3 (B = Sn, Pb; X = Br, I) perovskites for solar cell absorbers*. APL Materials, vol. 2, no. 8, page 081801, 2014. 13

[Fermi 1928] E. Fermi. *Eine statistische Methode zur Bestimmung einiger Eigenschaften des Atoms und ihre Anwendung auf die Theorie des periodischen Systems der Elemente*. Science, vol. 48, pages 73–79, 1928. 12

[Filip 2018] Marina R. Filip, George Volonakis and Feliciano Giustino. Hybrid halide perovskites: Fundamental theory and materials design, pages 1–30. Springer International Publishing, Cham, 2018. 34

[Fischer 1995] George L. Fischer, Robert W. Boyd, Russell J. Gehr, Samson A. Jenekhe, John A. Osaheni, J. E. Sipe and Laura A. Weller-Brophy. *Enhanced Nonlinear Optical Response of Composite Materials*. Phys. Rev. Lett., vol. 74, pages 1871–1874, Mar 1995. 22

[Fox 2001] Mark Fox. Optical properties of solids, volume 70. 01 2001. 24

[Fox 2006] A.M. Fox, M. Fox, D.P.A.M. Fox and Oxford University Press. Quantum optics: An introduction. Oxford Master Series in Physics. OUP Oxford, 2006. 16

[G. Burns 1990] A. M. Glazer G. Burns. Space Groups for Solid State Scientists. Academic Press, Boston, first edition édition, 1990. 15

[Gehr 1996] Russell J. Gehr, George L. Fischer, Robert W. Boyd and J. E. Sipe. *Nonlinear optical response of layered composite materials*. Phys. Rev. A, vol. 53, pages 2792–2798, Apr 1996. 22

[Geist 1990] Jon Geist, A. Russell Schaefer, Jun-Feng Song, Yun Hsia Wang and Edward F. Zalewski. *An Accurate Value for the Absorption Coefficient of Silicon at 633 nm*. Journal of research of the National Institute of Standards and Technology, vol. 95, no. 5, pages 549–558, 1990. 28179791[pmid]. 24, 25

[Geng 2014] Wei Geng, Le Zhang, Yan-Ning Zhang, Woon-Ming Lau and Li-Min Liu. *First-Principles Study of Lead Iodide Perovskite Tetragonal and Orthorhombic Phases for Photovoltaics*. The Journal of Physical Chemistry C, vol. 118, no. 34, pages 19565–19571, 2014. 13

[Giannozzi 2009] Paolo Giannozzi, Stefano Baroni, Nicola Bonini, Matteo Calandra, Roberto Car, Carlo Cavazzoni, Davide Ceresoli, Guido L. Chiarotti, Matteo Cococcioni, Ismaila Dabo, Andrea Dal Corso, Stefano De Gironcoli, Stefano Fabris, Guido Fratesi, Ralph Gebauer, Uwe Gerstmann, Christos Gougoussis, Anton Kokalj, Michele Lazzeri, Layla Martin-Samos, Nicola

Marzari, Francesco Mauri, Riccardo Mazzarello, Stefano Paolini, Alfredo Pasquarello, Lorenzo Paulatto, Carlo Sbraccia, Sandro Scandolo, Gabriele Sclauzero, Ari P. Seitsonen, Alexander Smogunov, Paolo Umari and Renata M. Wentzcovitch. *QUANTUM ESPRESSO: A modular and open-source software project for quantum simulations of materials.* Journal of Physics Condensed Matter, vol. 21, no. 39, 2009. 3, 4, 13

[Giannozzi 2017] P Giannozzi, O Andreussi, T Brumme, O Bunau, M Buongiorno Nardelli, M Calandra, R Car, C Cavazzoni, D Ceresoli, M Cococcioni, N Colonna, I Carnimeo, A Dal Corso, S de Gironcoli, P Delugas, R A DiStasio, A Ferretti, A Floris, G Fratesi, G Fugallo, R Gebauer, U Gerstmann, F Giustino, T Gorni, J Jia, M Kawamura, H-Y Ko, A Kokalj, E KÃ¼Ã§Ã¼kbenli, M Lazzeri, M Marsili, N Marzari, F Mauri, N L Nguyen, H-V Nguyen, A Otero de-la Roza, L Paulatto, S Poncé, D Rocca, R Sabatini, B Santra, M Schlipf, A P Seitsonen, A Smogunov, I Timrov, T Thonhauser, P Umari, N Vast, X Wu and S Baroni. *Advanced capabilities for materials modelling with Quantum ESPRESSO.* Journal of Physics: Condensed Matter, vol. 29, no. 46, page 465901, oct 2017. 3, 4

[Giannozzi 2020] Paolo Giannozzi, Oscar Baseggio, Pietro BonfÃ , Davide Brunato, Roberto Car, Ivan Carnimeo, Carlo Cavazzoni, Stefano de Gironcoli, Pietro Delugas, Fabrizio Ferrari Ruffino, Andrea Ferretti, Nicola Marzari, Iurii Timrov, Andrea Urru and Stefano Baroni. *Quantum ESPRESSO toward the exascale.* The Journal of Chemical Physics, vol. 152, no. 15, page 154105, 2020. 3, 4

[Gielen 2019] Dolf Gielen, Francisco Boshell, Deger Saygin, Morgan D. Bazilian, Nicholas Wagner and Ricardo Gorini. *The role of renewable energy in the global energy transformation.* Energy Strategy Reviews, vol. 24, pages 38–50, 2019. 1

[Giorgi 2015] Giacomo Giorgi and Koichi Yamashita. *Alternative, Lead-free, Hybrid Organic-Inorganic Perovskites for Solar Applications: A DFT Analysis.* Chemistry Letters, vol. 44, no. 6, pages 826–828, 2015. 13

[Gomes 2019] Eduardo O. Gomes, Guilherme S.L. Fabris, Mateus M. Ferrer, Fabiana V. Motta, Mauricio R.D. Bomio, Juan Andres, Elson Longo and Julio R. Sambrano. *Computational procedure to an accurate DFT simulation to solid state systems.* Computational Materials Science, vol. 170, page 109176, 2019. 3

[Gonze 2002] X. Gonze, J.-M. Beuken, R. Caracas, F. Detraux, M. Fuchs, G.-M. Rignanese, L. Sindic, M. Verstraete, G. Zerah, F. Jollet, M. Torrent, A. Roy, M. Mikami, Ph. Ghosez, J.-Y. Raty and D.C. Allan. *First-principles computation of material properties: The ABINIT software project.* Computational Materials Science, vol. 25, no. 3, pages 478–492, November 2002. 3

[Gonze 2005] Xavier Gonze. *A brief introduction to the ABINIT software package.* Zeitschrift fÃ¼r Kristallographie - Crystalline Materials, vol. 220, no. 5-6, pages 558–562, 2005. 3

[Green 1982] M.A. Green. Solar cells: Operating principles, technology, and system applications. Prentice-Hall Contemporary Comparative Politics Series. Prentice-Hall, 1982. 24

[Green 2014] Martin A. Green, Anita Ho-Baillie and Henry J. Snaith. *The emergence of perovskite solar cells.* Nature Photonics, no. 8, pages 506–514, 2014. iii, 7

[Green 2015] Martin A. Green, Yajie Jiang, Arman Mahboubi Soufiani and Anita Ho-Baillie. *Optical Properties of Photovoltaic Organic-Inorganic Lead Halide Perovskites.* The Journal of Physical Chemistry Letters, vol. 6, no. 23, pages 4774–4785, 2015. PMID: 26560862. 30

[He 1999] G. He and S.H. Liu. Physics of nonlinear optics. World Scientific, 1999. 16

[Hecht 2017] E. Hecht. Optics. Pearson Education, Incorporated, 2017. 25

[Heine 1970] Volker Heine. *The Pseudopotential Concept.* volume 24 of *Solid State Physics*, pages 1–36. Academic Press, 1970. 14

[Hernández-Haro 2019] Noemí Hernández-Haro, Joaquín Ortega-Castro, Yaroslav B. Martynov, Rashid G. Nazmitdinov and Antonio Frontera. *DFT prediction of band gap in organic-inorganic metal halide perovskites: An exchange-correlation functional benchmark study.* Chemical Physics, vol. 516, pages 225–231, 2019. 13

[HervÃ© 1994] P. HervÃ© and L.K.J. Vandamme. *General relation between refractive index and energy gap in semiconductors.* Infrared Physics & Technology, vol. 35, no. 4, pages 609–615, 1994. 50

[Herz 2017] Laura M. Herz. *Charge-Carrier Mobilities in Metal Halide Perovskites: Fundamental Mechanisms and Limits.* ACS Energy Letters, vol. 2, no. 7, pages 1539–1548, 2017. 34

[Hohenberg 1964] P. Hohenberg. *Inhomogeneous Electron Gas.* PHYSICAL REVIEW, vol. 136, no. 3 B, pages 864–871, 1964. 4, 12

[Huang 2019] Fei Huang, Mengjie Li, Peter Siffalovic, Guozhong Cao and Jianjun Tian. *From scalable solution fabrication of perovskite films towards commercialization of solar cells.* Energy Environ. Sci., vol. 12, pages 518–549, 2019. 1

[Huang 2021] Hsin-Hsiang Huang, Qi-Han Liu, Hsinhan Tsai, Shreetu Shrestha, Li-Yun Su, Po-Tuan Chen, Yu-Ting Chen, Tso-An Yang, Hsin Lu, Ching-Hsiang Chuang, King-Fu Lin, Syang-Peng Rwei, Wanyi Nie and Leeyih Wang. *A simple one-step method with wide processing window for high-quality perovskite mini-module fabrication.* Joule, vol. 5, no. 4, pages 958–974, 2021. 34

[Hutchings 1992] D. C. Hutchings, M. Sheik-Bahae, D. J. Hagan and E. W. Van Stryland. *Kramers-Krönig relations in nonlinear optics.* Optical and Quantum Electronics, vol. 24, no. 1, pages 1–30, Jan 1992. 23

[Hybertsen 1986] Mark S. Hybertsen and Steven G. Louie. *Electron correlation in semiconductors and insulators: Band gaps and quasiparticle energies.* Phys. Rev. B, vol. 34, no. 8, pages 5390–5413, Oct 1986. 12, 21, 66

[Indari 2017] E. D. Indari, T. D.K. Wungu and R. Hidayat. *Ab-Initio Calculation of Electronic Structure of Lead Halide Perovskites with Formamidinium Cation as an Active Material for Perovskite Solar Cells.* In Journal of Physics: Conference Series, volume 877. Institute of Physics Publishing, aug 2017. 8

[Janesko 2021] Benjamin G. Janesko. *Replacing hybrid density functional theory: motivation and recent advances.* Chem. Soc. Rev., pages –, 2021. 11, 13

[Jellison 1999] G.E. Jellison. *Ellipsometry.* In John C. Lindon, editeur, Encyclopedia of Spectroscopy and Spectrometry, pages 402–411. Elsevier, Oxford, 1999. 57, 58

[Jeon 2014a] Nam Joong Jeon, Jun Hong Noh, Young Chan Kim, Woon Seok Yang, Seungchan Ryu and Sang Il Seok. *Solvent engineering for high-performance inorganic–organic hybrid perovskite solar cells.* Nature Materials, vol. 13, no. 9, pages 897–903, Sep 2014. 34

[Jeon 2014b] Nam Joong Jeon, Jun Hong Noh, Young Chan Kim, Woon Seok Yang, Seungchan Ryu and Sang Il Seok. *Solvent engineering for high-performance inorganic-organic hybrid perovskite solar cells.* Nature Materials, vol. 13, no. 9, pages 897–903, 2014. 1

[Kanemitsu 2017] Yoshihiko Kanemitsu. *Luminescence spectroscopy of lead-halide perovskites: materials properties and application as photovoltaic devices.* J. Mater. Chem. C, vol. 5, pages 3427–3437, 2017. vi, 58

[Keast 2005] V.J. Keast. *Ab initio calculations of plasmons and interband transitions in the low-loss electron energy-loss spectrum.* Journal of Electron Spectroscopy and Related Phenomena, vol. 143, no. 2, pages 97–104, 2005. Electron Energy Loss Spectroscopy in the Electron Microscope. 25

[Kieslich 2014] Gregor Kieslich, Shijing Sun and Anthony K. Cheetham. *Solid-state principles applied to organic-inorganic perovskites, new tricks for an old dog.* Chem. Sci., vol. 5, pages 4712–4715, 2014. 30

[Kim 2014] Jongseob Kim, Sung-Hoon Lee, Jung Hoon Lee and Ki-Ha Hong. *The Role of Intrinsic Defects in Methylammonium Lead Iodide Perovskite.* The Journal of Physical Chemistry Letters, vol. 5, no. 8, pages 1312–1317, 2014. 13

[Kittel 2004] C. Kittel. Introduction to solid state physics. Wiley, 2004. 16, 21

[Klimeš 2011] Ji ří Klimeš, David R. Bowler and Angelos Michaelides. *Van der Waals density functionals applied to solids.* Phys. Rev. B, vol. 83, page 195131, May 2011. 13

[Kohn 1965] W. Kohn and L. J. Sham. *Self-Consistent Equations Including Exchange and Correlation Effects.* Phys. Rev., vol. 140, pages A1133–A1138, Nov 1965. 12, 13

[Kojima 2009] Akihiro Kojima, Kenjiro Teshima, Yasuo Shirai and Tsutomu Miyasaka. *Organometal halide perovskites as visible-light sensitizers for photovoltaic cells.* Journal of the American Chemical Society, 2009. 9

[Kovalev 1965] O. V. Kovalev. Irreducible Representations of the Space Groups. Gordon and Breach, New York, first edition édition, 1965. 15

[KRANE 1996] K.A. KRANE and K.S. Krane. Modern physics. Milestones in the history of modern physics. Wiley, 1996. 19

[Kresse 1993a] G. Kresse and J. Hafner. *Ab initio molecular dynamics for liquid metals.* Phys. Rev. B, vol. 47, pages 558–561, Jan 1993. 3

[Kresse 1993b] G. Kresse and J. Hafner. *Ab initio molecular dynamics for liquid metals.* Physical Review B, vol. 47, no. 1, pages 558–561, 1993. 3, 14

[Kresse 1996] G. Kresse and J. FurthmÃ$\frac{1}{4}$ller. *Efficiency of ab-initio total energy calculations for metals and semiconductors using a plane-wave basis set.* Computational Materials Science, vol. 6, no. 1, pages 15–50, 1996. 3

[Kühne 2020] Thomas D. Kühne, Marcella Iannuzzi, Mauro Del Ben, Vladimir V. Rybkin, Patrick Seewald, Frederick Stein, Teodoro Laino, Rustam Z. Khaliullin, Ole Schütt, Florian Schiffmann, Dorothea Golze, Jan Wilhelm, Sergey Chulkov, Mohammad Hossein Bani-Hashemian, Valéry Weber, Urban Borštnik, Mathieu Taillefumier, Alice Shoshana Jakobovits, Alfio Lazzaro, Hans Pabst, Tiziano Müller, Robert Schade, Manuel Guidon, Samuel Andermatt, Nico Holmberg, Gregory K. Schenter, Anna Hehn, Augustin Bussy, Fabian Belleflamme, Gloria Tabacchi, Andreas Glöß, Michael Lass, Iain Bethune, Christopher J. Mundy, Christian Plessl, Matt Watkins, Joost VandeVondele,

Matthias Krack and Jürg Hutter. *CP2K: An electronic structure and molecular dynamics software package -Quickstep: Efficient and accurate electronic structure calculations.* Journal of Chemical Physics, vol. 152, no. 19, 2020. 14

[Lamichhane 2020] Aneer Lamichhane and Nuggehalli M. Ravindra. *Energy Gap-Refractive Index Relations in Perovskites.* Materials (Basel, Switzerland), vol. 13, no. 8, page 1917, Apr 2020. 32325802[pmid]. 49, 51

[Lamichhane 2021] Aneer Lamichhane and N M Ravindra. *First-principles study of cubic alkaline-earth metal zirconate perovskites.* Journal of Physics Communications, vol. 5, no. 3, page 035006, mar 2021. 51

[Lee 2004] Ming-Hsien Lee, Chou-Hsun Yang and Jeng-Huei Jan. *Band-resolved analysis of nonlinear optical properties of crystalline and molecular materials.* Phys. Rev. B, vol. 70, page 235110, Dec 2004. 46

[Lee 2012] Michael M. Lee, Joël Teuscher, Tsutomu Miyasaka, Takurou N. Murakami and Henry J. Snaith. *Efficient Hybrid Solar Cells Based on Meso-Superstructured Organometal Halide Perovskites.* Science, vol. 338, no. 6107, pages 643–647, 2012. 34

[Lee 2014] Youn-Jung Lee, Byung-Sung Kim, S. Ifitiquar, Cheolmin Park and Junsin Yi. *Silicon solar cells: Past, present and the future.* Journal of the Korean Physical Society, vol. 65, pages 355–361, 08 2014. 2

[Leguy 2016] Aurélien M.A. Leguy, Pooya Azarhoosh, M. Isabel Alonso, Mariano Campoy-Quiles, Oliver J. Weber, Jizhong Yao, Daniel Bryant, Mark T. Weller, Jenny Nelson, Aron Walsh, Mark Van Schilfgaarde and Piers R.F. Barnes. *Experimental and theoretical optical properties of methylammonium lead halide perovskites.* Nanoscale, vol. 8, no. 12, pages 6317–6327, 2016. 36, 38, 57

[Leitsmann 2005] R. Leitsmann, W. G. Schmidt, P. H. Hahn and F. Bechstedt. *Second-harmonic polarizability including electron-hole attraction from band-structure theory.* Phys. Rev. B, vol. 71, page 195209, May 2005. 46

[Lemanov 1999] V.V. Lemanov, A.V. Sotnikov, E.P. Smirnova, M. Weihnacht and R. Kunze. *Perovskite $CaTiO_3$ as an incipient ferroelectric.* Solid State Communications, vol. 110, no. 11, pages 611–614, 1999. 7

[Li 2016] Jingrui Li and Patrick Rinke. *Atomic structure of metal-halide perovskites from first principles: The chicken-and-egg paradox of the organic-inorganic interaction.* Phys. Rev. B, vol. 94, page 045201, Jul 2016. 29

[Lieb 1977] Elliott H Lieb and Barry Simon. *The Thomas-Fermi theory of atoms, molecules and solids.* Advances in Mathematics, vol. 23, no. 1, pages 22–116, 1977. 12

[Liu 2013a] Mingzhen Liu, Michael B. Johnston and Henry J. Snaith. *Efficient planar heterojunction perovskite solar cells by vapour deposition.* Nature, vol. 501, pages 395–398, 2013. 2

[Liu 2013b] Mingzhen Liu, Michael B. Johnston and Henry J. Snaith. *Efficient planar heterojunction perovskite solar cells by vapour deposition.* Nature, vol. 501, pages 395–398, 2013. 8

[Liu 2015] Xiangye Liu, Wei Zhao, Houlei Cui, Yi'an Xie, Yaoming Wang, Tao Xu and Fuqiang Huang. *Organic-inorganic halide perovskite based solar cells-revolutionary progress in photovoltaics.* Inorg. Chem. Front., vol. 2, pages 315–335, 2015. 7

[Liu 2018] Dongyan Liu, Shanshan Li, Fang Bian and Xiangying Meng. *First-Principles Investigation on the Electronic and Mechanical Properties of Cs-Doped CH3NH3PbI3.* Materials, vol. 11, no. 7, 2018. 13

[Löper 2015] Philipp Löper, Michael Stuckelberger, Bjoern Niesen, Jérémie Werner, Miha Filipic, Soo-Jin Moon, Jun-Ho Yum, Marko Topic, Stefaan De Wolf and Christophe Ballif. *Complex Refractive Index Spectra of $CH_3NH_3PbI_3$ Perovskite Thin Films Determined by Spectroscopic Ellipsometry and Spectrophotometry.* The Journal of Physical Chemistry Letters, vol. 6, no. 1, pages 66–71, 2015. PMID: 26263093. 24

[Lucarini 2005] V. Lucarini, J.J. Saarinen, K.E. Peiponen and E.M. Vartiainen. Kramers-kronig relations in optical materials research. Springer Series in Optical Sciences. Springer Berlin Heidelberg, 2005. 23

[Makableh 2019] Yahia F. Makableh, Ghaleb Aljaiuossi and Rama Al-Abed. *Comprehensive design analysis of electron transmission nanostructured layers of heterojunction perovskite solar cells.* Superlattices and Microstructures, vol. 130, no. May, pages 390–395, 2019. iii, 10

[Mamedov 2011] Amirullah M. Mamedov and Ekmel Ozbay. *Mechanism of the electro-optic effect and nonlinear optical susceptibilities of some ferroelectrics: ab initio calculation.* no. 2, pages 1–26, 2011. 9, 23

[Martin 2004] R.M. Martin, R.M. Martin and Cambridge University Press. Electronic structure: Basic theory and practical methods. Cambridge University Press, 2004. 16, 21

[Mashiyama 2006] H Mashiyama and Y Kawamura. *The Anti-Polar Structure of CH 3 NH 3 PbBr 3.* vol. 51, no. phase IV, pages 15–17, 2006. 32

[Matsushita 2011] Yu-ichiro Matsushita, Kazuma Nakamura and Atsushi Oshiyama. *Comparative study of hybrid functionals applied to structural and electronic properties of semiconductors and insulators.* Phys. Rev. B, vol. 84, page 075205, Aug 2011. 29

[Meng 2018] Lei Meng, Jingbi You and Yang Yang. *Addressing the stability issue of perovskite solar cells for commercial applications*. Nature Communications, vol. 9, no. 1, pages 1–4, 2018. 2

[Meza 2019] Ulises R. Meza, Bernardo S. Mendoza and W. Luis Mochán. *Second-harmonic generation in nanostructured metamaterials*. Phys. Rev. B, vol. 99, page 125408, Mar 2019. 21

[Mohamed 2019] Hassen Mohamed, Mehdi Ben Jebli and Slim Ben Youssef. *Renewable and fossil energy, terrorism, economic growth, and trade: Evidence from France*. Renewable Energy, vol. 139, pages 459–467, 2019. 1

[Molina-Sánchez 2013] Alejandro Molina-Sánchez, Davide Sangalli, Kerstin Hummer, Andrea Marini and Ludger Wirtz. *Effect of spin-orbit interaction on the optical spectra of single-layer, double-layer, and bulk MoS_2*. Phys. Rev. B, vol. 88, page 045412, Jul 2013. 45

[Monkhorst 1976] Hendrik J. Monkhorst and James D. Pack. *Special points for Brillouin-zone integrations*. Phys. Rev. B, vol. 13, pages 5188–5192, Jun 1976. 46

[Mosconi 2015a] Edoardo Mosconi, Jon M. Azpiroz and Filippo De Angelis. *Ab Initio Molecular Dynamics Simulations of Methylammonium Lead Iodide Perovskite Degradation by Water*. Chemistry of Materials, vol. 27, no. 13, pages 4885–4892, 2015. 13

[Mosconi 2015b] Edoardo Mosconi, Paolo Umari and Filippo De Angelis. *Electronic and optical properties of mixed Sn-Pb organohalide perovskites: a first principles investigation*. J. Mater. Chem. A, vol. 3, 2015. 13

[Mosconi 2016] Edoardo Mosconi, Paolo Umari and Filippo De Angelis. *Electronic and optical properties of MAPbX3 perovskites (X = I, Br, Cl): A unified DFT and GW theoretical analysis*. Physical Chemistry Chemical Physics, vol. 18, no. 39, pages 27158–27164, 2016. 31, 57

[Moss 1951] T S Moss. *Photoconductivity in the Elements*. Proceedings of the Physical Society. Section A, vol. 64, no. 6, pages 590–591, jun 1951. 50

[Motta 2015] Carlo Motta, Fedwa El-Mellouhi and Stefano Sanvito. *Charge carrier mobility in hybrid halide perovskites*. Scientific Reports, vol. 5, no. 1, page 12746, Aug 2015. 34

[Nastos 2005] F. Nastos, B. Olejnik, K. Schwarz and J. E. Sipe. *Scissors implementation within length-gauge formulations of the frequency-dependent nonlinear optical response of semiconductors*. Phys. Rev. B, vol. 72, no. 4, page 045223, 2005. 17, 46, 67

[National Renewable Energy Laboratory] National Renewable Energy Laboratory. *Best Research-Cell Efficiency Chart*. iii, 2

[Neese 2012] Frank Neese. *The ORCA program system.* Wiley Interdisciplinary Reviews: Computational Molecular Science, vol. 2, no. 1, pages 73–78, 2012. 14

[Nenkov 2008] Milen R. Nenkov and Tamara G. Pencheva. *Determination of thin film refractive index and thickness by means of film phase thickness.* Central European Journal of Physics, vol. 6, no. 2, pages 332–343, Jun 2008. 49

[Ness 2005] H. Ness and A. J. Fisher. *Vibrational inelastic scattering effects in molecular electronics.* Proceedings of the National Academy of Sciences of the United States of America, vol. 102, no. 25, pages 8826–8831, Jun 2005. 15956206[pmid]. 53

[Niu 2015] Guangda Niu, Xudong Guo and Liduo Wang. *Review of recent progress in chemical stability of perovskite solar cells.* Journal of Materials Chemistry A, vol. 3, no. 17, pages 1–29, 2015. 2

[Nozières 1958] Philippe Nozières and David Pines. *Electron Interaction in Solids. General Formulation.* Phys. Rev., vol. 109, pages 741–761, Feb 1958. 45

[Okoye 2003] C M I Okoye. *Theoretical study of the electronic structure, chemical bonding and optical properties of KNbO3in the paraelectric cubic phase.* Journal of Physics: Condensed Matter, vol. 15, no. 35, pages 5945–5958, aug 2003. 46

[Oku 2015] Takeo Oku. *Crystal Structures of CH3NH3PbI3 and Related Perovskite Compounds Used for Solar Cells.* In Solar Cells - New Approaches and Reviews. InTech, oct 2015. vii, 8, 9, 29, 31, 32, 56

[Ong 2001] H. C. Ong, J. Y. Dai, A. S. K. Li, G. T. Du, R. P. H. Chang and S. T. Ho. *Effect of a microstructure on the formation of self-assembled laser cavities in polycrystalline ZnO.* Journal of Applied Physics, vol. 90, no. 3, pages 1663–1665, 2001. 49

[Onida 2002] Giovanni Onida, Lucia Reining and Angel Rubio. *Electronic excitations: density-functional versus many-body Green's-function approaches.* Rev. Mod. Phys., vol. 74, pages 601–659, Jun 2002. 21, 45

[Ono 2018] Madoka Ono, Shuhei Aoyama, Masanori Fujinami and Setsuro Ito. *Significant suppression of Rayleigh scattering loss in silica glass formed by the compression of its melted phase.* Opt. Express, vol. 26, no. 7, pages 7942–7948, Apr 2018. 49

[Osterthun 2021] N. Osterthun, N. Neugebohrn, K. Gehrke, M. Vehse and C. Agert. *Spectral engineering of ultrathin germanium solar cells for combined photovoltaic and photosynthesis.* Opt. Express, vol. 29, no. 2, pages 938–950, Jan 2021. 1

[Palik 1998] E.D. Palik. Handbook of optical constants of solids. Academic Press handbook series. Elsevier Science, 1998. 49

[Park 2015] Nam Gyu Park. *Perovskite solar cells: An emerging photovoltaic technology*, 2015. 10

[Perdew 1986] J. P. Perdew. *Density-functional approximation for the correlation energy of the inhomogeneous electron gas.* Physical Review B, vol. 33, no. June, pages 8822–8824, 1986. 13

[Perdew 1996] John P. Perdew, Kieron Burke and Matthias Ernzerhof. *Generalized gradient approximation made simple.* Physical Review Letters, vol. 77, no. 18, pages 3865–3868, 1996. 11, 13

[Petrovic 2015] Milos Petrovic, Vijila Chellappan and Seeram Ramakrishna. *Perovskites: Solar cells & engineering applications-materials and device developments.* Solar Energy, vol. 122, pages 678–699, 2015. 8

[Ramanujam 2015a] Srinivasa Varadan Ramanujam. *Band Structure of Graphene Using Emperical Pseudopotentials.* Arizona State University, no. December, pages 1–61, 2015. 13

[Ramanujam 2015b] Srinivasa Varadan Ramanujam. *Band Structure of Graphene Using Emperical Pseudopotentials.* Arizona State University, no. December, pages 1–61, 2015. 14

[Rathod 2017] Siddharth Narendrakumar Rathod. *Structure Stability and Optical Response of Lead Halide Hybrid Perovskite Photovoltaic Materials : A First-Principles Simulation Study Halide Hybrid Perovskite Photovoltaic materials: A First Principles Simulation Study.* 2017. 12

[Reddy 2008] R.R. Reddy, K. Rama Gopal, K. Narasimhulu, L. Siva Sankara Reddy, K. Raghavedra Kumar, C.V. Krishna Reddy and Syed Nisar Ahmed. *Correlation between optical electronegativity and refractive index of ternary chalcopyrites, semiconductors, insulators, oxides and alkali halides.* Optical Materials, vol. 31, no. 2, pages 209–212, 2008. 51

[Reshak 2012] Ali Hussain Reshak, Xuean Chen, S. Auluck and H. Kamarudin. *Linear and nonlinear optical susceptibilities and hyperpolarizability of borate LiNaB4O7 single crystals: Theory and experiment.* Journal of Applied Physics, vol. 112, no. 5, page 053526, 2012. 46

[Romero 2020] Aldo H. Romero, Douglas C. Allan, Bernard Amadon, Gabriel Antonius, Thomas Applencourt, Lucas Baguet, Jordan Bieder, FranÃ§ois Bottin, Johann Bouchet, Eric Bousquet, Fabien Bruneval, Guillaume Brunin, Damien Caliste, Michel CÃ´tÃ©, Jules Denier, Cyrus Dreyer, Philippe Ghosez, Matteo Giantomassi, Yannick Gillet, Olivier Gingras, Donald R.

Hamann, Geoffroy Hautier, FranÃ§ois Jollet, GÃ©rald Jomard, Alexandre Martin, Henrique P. C. Miranda, Francesco Naccarato, Guido Petretto, Nicholas A. Pike, Valentin Planes, Sergei Prokhorenko, Tonatiuh Rangel, Fabio Ricci, Gian-Marco Rignanese, Miquel Royo, Massimiliano Stengel, Marc Torrent, Michiel J. van Setten, Benoit Van Troeye, Matthieu J. Verstraete, Julia Wiktor, Josef W. Zwanziger and Xavier Gonze. *ABINIT: Overview and focus on selected capabilities*. The Journal of Chemical Physics, vol. 152, no. 12, page 124102, 2020. 3

[Salazar 2016] Cuauhtémoc Salazar, J. L. Cheng and J. E. Sipe. *Coherent control of current injection in zigzag graphene nanoribbons*. Phys. Rev. B, vol. 93, page 075442, Feb 2016. 46

[Schrödinger 1926] E. Schrödinger. *An Undulatory Theory of the Mechanics of Atoms and Molecules*. Phys. Rev., vol. 28, pages 1049–1070, Dec 1926. 12

[Seminario 1995] Jorge M. Seminario. *An introduction to density functional theory in chemistry*. In J.M. Seminario and P. Politzer, editeurs, Modern Density Functional Theory, volume 2 of *Theoretical and Computational Chemistry*, pages 1–27. Elsevier, 1995. 13

[Senocrate 2019] Alessandro Senocrate, Gee Yeong Kim, Michael Grätzel and Joachim Maier. *Thermochemical Stability of Hybrid Halide Perovskites*. ACS Energy Letters, vol. 4, no. 12, pages 2859–2870, 2019. 34

[Setyawan 2010] Wahyu Setyawan and Stefano Curtarolo. *High-throughput electronic band structure calculations: Challenges and tools*. Computational Materials Science, vol. 49, no. 2, pages 299–312, 2010. iii, 16

[Shi 2018] Jing Shi and Sining Yun. First-principles dft calculations for perovskite solar cells, chapitre 19, pages 487–509. John Wiley & Sons, Ltd, 2018. 13

[Shirayama 2016] Masaki Shirayama, Hideyuki Kadowaki, Tetsuhiko Miyadera, Takeshi Sugita, Masato Tamakoshi, Masato Kato, Takemasa Fujiseki, Daisuke Murata, Shota Hara, Takurou N. Murakami and et al. *Optical Transitions in Hybrid Perovskite Solar Cells: Ellipsometry, Density Functional Theory, and Quantum Efficiency Analyses forCH3NH3PbI3*. Physical Review Applied, vol. 5, no. 1, 2016. 13

[Singh 2012] R.J. Singh. Solid state physics. Always Learning. Dorling Kindersley, 2012. 16

[Sipe 1987] J. E. Sipe, D. J. Moss and H. M. van Driel. *Phenomenological theory of optical second- and third-harmonic generation from cubic centrosymmetric crystals*. Phys. Rev. B, vol. 35, pages 1129–1141, Jan 1987. 21

[Sipe 2000] J. E. Sipe and A. I. Shkrebtii. *Second-order optical response in semiconductors*. Phys. Rev. B, vol. 61, pages 5337–5352, Feb 2000. 21, 22, 23, 45

[Snaith 2012] Henry J. Snaith, Michael M. Lee and Tsutomu Miyasaka. *Efficient Hybrid Solar Cells Based on Meso-Superstructured Organometal Halide Perovskites*. Science, vol. 338, pages 643–647, 2012. 9

[Sohn 2017] Honglae Sohn. Refractive index of porous silicon, pages 1–12. Springer International Publishing, Cham, 2017. 51

[Soler 2002] José M. Soler, Emilio Artacho, Julian D. Gale, Alberto García, Javier Junquera, Pablo Ordejón and Daniel Sánchez-Portal. *The SIESTA method for ab initio order-N materials simulation*. Journal of Physics Condensed Matter, vol. 14, no. 11, pages 2745–2779, 2002. 14

[Stahrenberg 2001] K. Stahrenberg, Th. Herrmann, K. Wilmers, N. Esser, W. Richter and M. J. G. Lee. *Optical properties of copper and silver in the energy range 2.5–9.0 eV*. Phys. Rev. B, vol. 64, page 115111, Aug 2001. 46

[Stephenson 2018] Michael Stephenson. *Chapter 1 - The Carbon Cycle, Fossil Fuels and Climate Change*. In Michael Stephenson, editeur, Energy and Climate Change, pages 1–26. Elsevier, 2018. 1

[Stranks 2013] Samuel D. Stranks, Giles E. Eperon, Giulia Grancini, Christopher Menelaou, Marcelo J. P. Alcocer, Tomas Leijtens, Laura M. Herz, Annamaria Petrozza and Henry J. Snaith. *Electron-Hole Diffusion Lengths Exceeding 1 Micrometer in an Organometal Trihalide Perovskite Absorber*. Science, vol. 342, no. 6156, pages 341–344, 2013. 34

[Sun 2016a] Yang Sun, Huan Xu, Bo Da, Shi feng Mao and Ze jun Ding. *Calculations of Energy-Loss Function for 26 Materials*. Chinese Journal of Chemical Physics, vol. 29, no. 6, pages 663–670, 2016. 25

[Sun 2016b] Yang Sun, Huan Xu, Bo Da, Shi-feng Mao and Ze-jun Ding. *Calculations of Energy-Loss Function for 26 Materials*. Chinese Journal of Chemical Physics, vol. 29, no. 6, pages 663–670, 2016. 52

[Suzuki 2019] Atsushi Suzuki, Masataka Kato, Naoki Ueoka and Takeo Oku. *Additive Effect of Formamidinium Chloride in Methylammonium Lead Halide Compound-Based Perovskite Solar Cells*. Journal of Electronic Materials, vol. 48, no. 6, pages 3900–3907, Jun 2019. 29

[Tao 2017] Shu Xia Tao, Xi Cao and Peter A. Bobbert. *Accurate and efficient band gap predictions of metal halide perovskites using the DFT-1/2 method: GW accuracy with DFT expense*. Scientific Reports, vol. 7, no. 1, page 14386, Oct 2017. 34

[Targhi 2018] Farhad Fouladi Targhi, Y. S. Jalili and F. Kanjouri. *MAPbI3 and FAPbI3 perovskites as solar cells Case study on structural, electrical and optical properties.* Results in physics, vol. 10, pages 616–627, 2018. 13

[Teller 1962] Edward Teller. *On the Stability of Molecules in the Thomas-Fermi Theory.* Rev. Mod. Phys., vol. 34, pages 627–631, Oct 1962. 4

[Thomas 1927a] L. H. Thomas. *The calculation of atomic fields.* Mathematical Proceedings of the Cambridge Philosophical Society, vol. 23, no. 5, pages 542–548, 1927. 4

[Thomas 1927b] L. H. Thomas. *The calculation of atomic fields.* Proceedings of the Cambridge Philosophical Society, vol. 23, no. 5, page 542, January 1927. 12

[Tokmakoff 2019] Andrei Tokmakoff. Time Dependent Quantum Mechanics & Spectroscopy. University of Chicago, first edit édition, 2019. 16, 23

[Toll 1956] John S. Toll. *Causality and the Dispersion Relation: Logical Foundations.* Phys. Rev., vol. 104, pages 1760–1770, Dec 1956. 23

[Tombe 2017] Sekai Tombe, Getachew Adam, Herwig Heilbrunner, Dogukan Apaydin, Christoph Ulbricht, Niyazi Sariciftci, Christopher Ardense, Emmanuel Iwuoha and Markus Scharber. *Optical and electronic properties of mixed halide (X = I, Cl, Br) methylammonium lead perovskite solar cells.* J. Mater. Chem. C, vol. 5, 01 2017. 15

[Tran 1999] Muoi Tran, Nacir Tit and M. W. C. Dharma-wardana. *Dielectric constant and light emission in Si/SiO2 superlattices.* Applied Physics Letters, vol. 75, no. 26, pages 4136–4138, 1999. 25

[Uprety 2019] Prakash Uprety, Indra Subedi, Maxwell M. Junda, Robert W. Collins and Nikolas J. Podraza. *Photogenerated Carrier Transport Properties in Silicon Photovoltaics.* Scientific Reports, vol. 9, no. 1, page 19015, Dec 2019. 34

[Van Krevelen 2009] D.W. Van Krevelen and K. Te Nijenhuis. *Optical Properties.* In Properties of Polymers, pages 287–318. Elsevier, 2009. 24

[van Mourik 2014] Tanja van Mourik, Michael BÃ$\frac{1}{4}$hl and Marie-Pierre Gaigeot. *Density functional theory across chemistry, physics and biology Introduction.* Philosophical transactions. Series A, Mathematical, physical, and engineering sciences, vol. 372, page 20120488, 02 2014. 3

[Vanderbilt 1990] David Vanderbilt. *Soft self-consistent pseudopotentials in a generalized eigenvalue formalism.* Physical Review B, vol. 41, no. 11, 1990. 15

[Viklund 2016] Lina Viklund, Louise Augustsson and Jonas Melander. *Numerical approaches to solving the time-dependent Schrödinger equation with different potentials*, 2016. 12

[Von Barth 2004] U Von Barth. *Basic Density-Functional Theory-an Overview.* Physica Scripta, vol. T109, pages 9–39, 2004. 12

[Walls 2012] D.F. Walls and G.J. Milburn. Quantum optics. Springer Study Edition. Springer Berlin Heidelberg, 2012. 16

[Wang 2016] Lingrui Wang, Kai Wang, Guanjun Xiao, Qiaoshi Zeng and Bo Zou. *Pressure-Induced Structural Evolution and Band Gap Shifts of Organometal Halide Perovskite-Based Methylammonium Lead Chloride.* Journal of Physical Chemistry Letters, vol. 7, no. 24, pages 5273–5279, 2016. 32

[Wang 2020] Kai Wang. *Optical properties of 5d transition metal oxides.* PhD thesis, University of Geneva, 2020. vi, 57, 58

[Wei 2017] Hui Wei, Yang Tang, Bo Feng and Hui You. *Importance of PbI2 morphology in two-step deposition of CH3NH3PbI3for high-performance perovskite solar cells.* Chinese Physics B, pages 1–8, 2017. 10

[Whitfield 2016] P. S. Whitfield, N. Herron, W. E. Guise, K. Page, Y. Q. Cheng, I. Milas and M. K. Crawford. *Structures, Phase Transitions and Tricritical Behavior of the Hybrid Perovskite Methyl Ammonium Lead Iodide.* Scientific Reports, vol. 6, no. June, pages 1–15, 2016. 8

[Wild 2013] Martin Wild, Doris Folini, Christoph Schär, Norman Loeb, Ellsworth G. Dutton and Gert König-Langlo. *The global energy balance from a surface perspective.* Climate Dynamics, vol. 40, no. 11, pages 3107–3134, Jun 2013. 1

[Wiser 1963] Nathan Wiser. *Dielectric Constant with Local Field Effects Included.* Phys. Rev., vol. 129, pages 62–69, Jan 1963. 45

[Wu 2014] Yongzhen Wu, Ashraful Islam, Xudong Yang, Chuanjiang Qin, Jian Liu, Kun Zhang, Wenqin Peng and Liyuan Han. *Retarding the crystallization of PbI2 for highly reproducible planar-structured perovskite solar cells via sequential deposition.* Energy and Environmental Science, vol. 32, no. 9, pages 1–6, 2014. 10

[Wu 2018a] Jian Wu, Jing-Jing Dong, Si-Xuan Chen, Hui-Ying Hao, Jie Xing and Hao Liu. *Fabrication of Efficient Organic-Inorganic Perovskite Solar Cells in Ambient Air.* Nanoscale Research Letters, vol. 13, no. 1, page 293, Sep 2018. 34

[Wu 2018b] Jiayi Wu, Wen qi, Zhe Luo, Ke Liu and Hong Zhu. *Electronic Structure and Stability of Lead-free Hybrid Halide Perovskites: A Density Functional Theory Study.* Journal of Shanghai Jiaotong University (Science), vol. 23, pages 202–208, 2018. 13

[Wu 2018c] Yinghui Wu, Wei Chen, Guo Chen, Liyu Liu, Zhubing He and Ruchuan Liu. *The Impact of Hybrid Compositional Film/Structure on Organic-Inorganic Perovskite Solar Cells*. Nanomaterials, vol. 8, no. 6, 2018. 10

[Wu 2019] Cuncun Wu, Duo Wang, Yuqing Zhang, Feidan Gu, Ganghong Liu, Ning Zhu, Wei Luo, Dong Han, Xuan Guo, Bo Qu, Shufeng Wang, Zuqiang Bian, Zhijian Chen and Lixin Xiao. *FAPbI3 Flexible Solar Cells with a Record Efficiency of 19.38% Fabricated in Air via Ligand and Additive Synergetic Process*. Advanced Functional Materials, vol. 1902974, pages 1–7, 2019. 9

[Xing 2013] Guichuan Xing, Nripan Mathews, Shuangyong Sun, Swee Sien Lim, Yeng Ming Lam, Michael Grätzel, Subodh Mhaisalkar and Tze Chien Sum. *Long-Range Balanced Electron- and Hole-Transport Lengths in Organic-Inorganic CH3NH3PbI3*. Science, vol. 342, no. 6156, pages 344–347, 2013. 34

[Xu 2015] Jixian Xu, Andrei Buin, Alexander H. Ip, Wei Li, Oleksandr Voznyy, Riccardo Comin, Mingjian Yuan, Seokmin Jeon, Zhijun Ning, Jeffrey J. McDowell, Pongsakorn Kanjanaboos, Jon-Paul Sun, Xinzheng Lan, Li Na Quan, Dong Ha Kim, Ian G. Hill, Peter Maksymovych and Edward H. Sargent. *Perovskite–fullerene hybrid materials suppress hysteresis in planar diodes*. Nature Communications, vol. 6, no. 1, page 7081, May 2015. 1

[YAKOVKIN 2007] I. N. YAKOVKIN and P. A. DOWBEN. *The Problem of the Band Gap In LDA Calcualtions*. Surface Review and Letters, vol. 14, no. 03, pages 481–487, 2007. 12

[Yang 2017] Shida Yang, Weifei Fu, Zhongqiang Zhang, Hongzheng Chen and Chang-Zhi Li. *Recent advances in perovskite solar cells: efficiency, stability and lead-free perovskite*. J. Mater. Chem. A, vol. 5, pages 11462–11482, 2017. 34

[Yang 2018] Jin-Peng Yang, Matthias Meissner, Takuma Yamaguchi, Xiu-Yun Zhang, Takahiro Ueba, Li-Wen Cheng, Shinichiro Ideta, Kiyohisa Tanaka, Xiang-Hua Zeng, Nobuo Ueno and Satoshi Kera. *Band Dispersion and Hole Effective Mass of Methylammonium Lead Iodide Perovskite*. Solar RRL, vol. 2, no. 10, page 1800132, 2018. 34

[Yehuda B. Band 2013] Yehuda B. Band. Quantum Mechanics with Applications to Nanotechnology and Information Science. News & Information for Chemical Engineers, 1st editio édition, 2013. 4

[Yu 2016] Z. G. Yu. *Effective-mass model and magneto-optical properties in hybrid perovskites*. Scientific Reports, vol. 6, no. 1, page 28576, Jun 2016. 34

[Yusoff 2016] Abd Rashid Bin Mohd Yusoff and Mohammad Khaja Nazeeruddin. *Organohalide Lead Perovskites for Photovoltaic Applications*. Journal of Physical Chemistry Letters, vol. 7, pages 2448–2450, 2016. iii, 2, 20

[Zangwill 1980] A. Zangwill and Paul Soven. *Density-functional approach to local-field effects in finite systems: Photoabsorption in the rare gases*. Phys. Rev. A, vol. 21, pages 1561–1572, May 1980. 45

[Zhang 2016] Wei Zhang, Giles E. Eperon and Henry J. Snaith. *Metal halide perovskites for energy applications*. Nature Energy, vol. 1, no. 6, page 16048, May 2016. 1

[Zhou 2007] Di Zhou. *An Introduction of Density Functional Theory and its Application*. Physics.Drexel.Edu, 2007. 12

[Zuo 2016] Lijian Zuo, Shiqi Dong, Nicholas De Marco, Yao Tsung Hsieh, Sang Hoon Bae, Pengyu Sun and Yang Yang. *Morphology Evolution of High Efficiency Perovskite Solar Cells via Vapor Induced Intermediate Phases*. Journal of the American Chemical Society, vol. 138, no. 48, pages 1–9, 2016. 10